



THE AERODYNAMIC DESIGN AND
DEVELOPMENT OF AN URBAN CONCEPT
VEHICLE THROUGH CFD ANALYSIS

Thesis submitted
in partial fulfilment of the requirements
for the degree

MASTER OF TECHNOLOGY
IN
MECHANICAL ENGINEERING

by

DONOVAN J COGAN

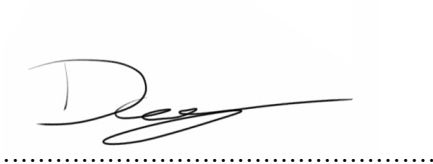
DEPARTMENT OF MECHANICAL ENGINEERING

CAPE PENINSULA UNIVERSITY OF TECHNOLOGY

2016

Plagiarism declaration

I, Donovan John Cogan, declare that the contents of this thesis represent my own unaided work, and that the thesis has not previously been submitted for academic examination towards any qualification. Furthermore, it represents my own opinions and not necessarily those of the Cape Peninsula University of Technology.

A handwritten signature in black ink, appearing to read 'D. Cogan', written over a dotted horizontal line.

Signed

A handwritten date '21/07/2016' in black ink, written over a dotted horizontal line.

Date

Abstract

This work presents the computational fluid dynamics (CFD) analysis of a light road vehicle. Simulations are conducted using the lattice Boltzmann method (LBM) with the wall adapting local eddy (WALE) turbulence model. Simulations include and compare the use of a rolling road, rotating wheels, adaptive refinement as well as showing comparison with a Reynolds-averaged Navier-Stokes (RANS) solver and the Spalart-Allmaras (SA) turbulence model. The lift coefficient of the vehicle for the most part was seen to show a much greater difference and inconsistencies when compared to drag from the comparisons of solvers, turbulence models, refinement and the effect of rolling road. Determining the drag of a road vehicle can be easily achieved and verified using multiple solvers and methods, however, the lift coefficient and its validation require a greater understanding of the vehicle flow field as well as the solvers, turbulence models and refinement levels capable of correctly simulating the turbulent regions around a vehicle. Using the presented method, it was found that the optimisation of vehicle aerodynamics can easily be done alongside the design evolution from initial low-drag shapes to the final detail design, ensuring aerodynamic characteristics are controlled with aesthetic change.

Keywords: CFD, lattice Boltzmann method, Reynolds-averaged Navier-Stokes, vehicle aerodynamics

Acknowledgments

My Supervisor, Prof. Greame Oliver for all the insight and advice concerning the project and thesis.

The PLMCC along with Prof. Stephane Bouye and Michael Petersen, for the funding and contributions towards this research project.

Adriaan Broodryk for the vehicles aesthetic design and class-A surfaces.

My family for their endless support throughout all of my studies.

My dearest Pippa, for all her encouragement and motivation through this work.

Contents

1	Introduction	1
1.1	Background	1
1.2	Literature review	2
1.3	Aims and objectives	3
1.3.1	CFD validation	4
1.3.2	Low-drag concept design	4
1.3.3	Final design	5
1.4	Dissertation structure	6
1.5	Delineations	6
2	Aerodynamics	7
2.1	Fluid mechanics	7
2.1.1	Boundary layer	8
2.1.2	Separation and wake	9
2.2	Vehicle aerodynamics	9
2.2.1	Forces and moments	9
2.2.2	Flow coefficients	11
2.2.3	Vehicle aerodynamic aspects	11
2.2.4	Vehicle aerodynamic design	13
3	CFD	15

3.1	Introduction	15
3.2	Conservation	16
3.3	Reynolds-averaged Navier-Stokes	16
3.4	Lattice Boltzmann	17
3.5	Turbulence	20
3.6	Boundary Layer	24
3.7	Simulation setup	26
3.7.1	General simulation settings	26
3.7.2	XFLOW simulation setup	27
3.7.3	FLUENT simulation setup	29
3.8	Flow visualisation	29
4	Initial vehicle concepts	30
4.1	CFD validation	30
4.1.1	Introduction	30
4.1.2	Geometry development	30
4.1.3	Simulation setup	31
4.1.4	Results and Discussion	31
4.2	Low-drag concept	33
4.2.1	Introduction	33
4.2.2	Geometry development	33
4.2.3	CFD simulation setup	37
4.2.4	Global environment setup	37
4.2.5	Domain refinement setup	38
4.2.6	Results and Discussion	39
4.3	Preliminary vehicle concepts	44
4.3.1	Introduction	44

4.3.2	Global environment setup	44
4.3.3	Domain refinement setup	45
5	CFD results of preliminary vehicle concepts	47
6	Result of aerodynamic development	49
6.1	Final design	49
6.1.1	Introduction	49
6.1.2	Geometry development	49
6.1.3	Simulation settings	51
6.1.4	Results and discussion	51
6.2	CFD comparison	52
6.2.1	Introduction	52
6.2.2	Geometry development	52
6.2.3	Simulation settings	53
6.2.4	Results and discussion	53
6.3	Aerodynamic modifications	58
6.3.1	Introduction	58
6.3.2	Geometry development	58
6.3.3	Simulation settings	58
6.3.4	Modification results and discussion	59
6.3.5	Modification combination development	63
6.3.6	Modification combination results and discussion	64
6.3.7	Final result and discussion	65
7	Conclusion and recommendations	66
	Appendix	69

List of Figures

2.1	Vehicle axis and moments	10
2.2	Vehicle contours	13
3.1	HPP model	18
3.2	$D2Q7$ and $D2Q9$ schemes	20
3.3	$D3Q19$ and $D3Q27$ schemes	20
3.4	$f_1(y^+u_\tau/u_c)$	25
3.5	$f_2(y^+u_p/u_c)$	25
3.6	Stability parameter	27
3.7	Velocity range	29
3.8	Pressure range	29
4.1	Ahmed dimensions	30
4.2	Computational domain - Ahmed body	31
4.3	Ahmed initial refinement	31
4.4	Ahmed final refinement	32
4.5	Ahmed refinement - stationary road	32
4.6	Ahmed refinement - rolling road	32
4.7	Low-drag concept surfaces	33
4.8	Side view of limiting planes	34
4.9	Top view of limiting planes	34
4.10	Side view of splines	34

4.11	Top view of splines	34
4.12	Low-drag concept filleted	34
4.13	Low-drag concept with wheel-arches	35
4.14	Simple wheel	35
4.15	3D scan of wheel	36
4.16	Wheel without tread	36
4.17	Tread development	36
4.18	Wheel with tread	36
4.19	Computational domain - Low-drag concept with straightforward flow .	37
4.20	Computational domain - Low-drag concept with yawed flow	38
4.21	Simple initial concept side view velocity vectors	39
4.22	Rounded initial concept side view velocity vectors	39
4.23	Rounded initial concept side view velocity vector cut plot	40
4.24	Rounded initial concept 10 yaw velocity vector cut plot	40
4.25	Rounded initial concept 10 yaw top velocity vector cut plot	40
4.26	Initial concept stationary simple wheel vector cut plot	41
4.27	Initial concept rotating simple wheel vector cut plot	42
4.28	Initial concept stationary simple rear wheel vector cut plot	42
4.29	Initial concept rotating simple wheel vector cut plot	42
4.30	Initial concept rotating detail wheel vector cut plot	42
4.31	Initial concept rotating detail wheel with tread vector cut plot	43
4.32	Initial concept rotating detail wheel with tread vector cut plot	43
4.33	Initial concept rotating detail wheel with tread and yaw vector cut plot	43
4.34	Computational domain - Concept model with straightforward flow . . .	44
4.35	Computational domain - Concept model with yawed flow	45
4.36	Concept 1	46
4.37	Concept 2	46

4.38	Concept 3	46
5.1	Isosurface - concept 1	48
5.2	Isosurface - concept 2	48
5.3	Isosurface - concept 3	48
6.1	Detailed final geometry	50
6.2	Detailed final geometry cutaway	50
6.3	Final simplified - FLUENT	52
6.4	Final simplified - XFLOW	52
6.5	FLUENT's mesh	53
6.6	XFLOW's lattice	53
6.7	XFLOW - WALE - 0.015	55
6.8	FLUENT - WALE - 0.015	55
6.9	XFLOW - WALE - 0.007	56
6.10	FLUENT - WALE - 0.007	56
6.11	XFLOW - SA - 0.015	56
6.12	FLUENT - SA - 0.015	56
6.13	XFLOW - SA - 0.007	56
6.14	FLUENT - SA - 0.007	56
6.15	Final model - centre cut velocity vectors	61
6.16	Spoiler 1 - centre cut velocity vectors	61
6.17	Spoiler 2 - centre cut velocity vectors	61
6.18	Final model - centre cut velocity vectors	62
6.19	Diffuser 1 - centre cut velocity vectors	62
6.20	Diffuser 2 - centre cut velocity vectors	62
A1	XY-plane pressure cut plot - concept 1	70
A2	XY-plane pressure cut plot - concept 2	70

A3	XY-plane pressure cut plot - concept 3	70
A4	XY-plane velocity vectors cut plot - concept 1	71
A5	XY-plane velocity vectors cut plot - concept 2	71
A6	XY-plane velocity vectors cut plot - concept 3	71
A7	XY-plane pressure cut plot at wheels - concept 1	72
A8	Centre cut XY-plane pressure cut plot at wheels - concept 2	72
A9	Centre cut XY-plane pressure cut plot at wheels - concept 3	72
A10	XY-plane velocity vectors cut plot at wheels - concept 1	73
A11	XY-plane velocity vectors cut plot at wheels - concept 2	73
A12	XY-plane velocity vectors cut plot at wheels - concept 3	73
A13	XZ-plane pressure cut plot - concept 1	74
A14	XZ-plane pressure cut plot - concept 2	74
A15	XZ-plane pressure cut plot - concept 3	74
A16	XZ-plane pressure cut plot - concept 1	75
A17	XZ-plane pressure cut plot - concept 2	75
A18	XZ-plane pressure cut plot - concept 3	75
B1	Spoiler 1	76
B2	Spoiler 2	76
B3	Diffuser 1	76
B4	Diffuser 2	76
B5	Front diffuser	76
B6	Wheel diffusers	76
B7	Side skirt	77
B8	Wheel cover	77
B9	Wheel arch top vent	77
B10	Wheel arch rear vent	77
B11	Wheel arch slot	77

B12	Rear vent	77
B13	Front air guide 1	78
B14	Front air guide 2	78
B15	Side mirrors	78
B16	Rear air guide	78

Abbreviations

BGK Bhatnagar-Gross-Krook

CAD computer aided design

CFD computational fluid dynamics

CFL Courant-Friedrichs-Lewy

CPUT Cape Peninsula University of Technology

DOF degrees of freedom

DS Dassault Systemes

LBM lattice Boltzmann method

LGA lattice gas automata

PLMCC Product Lifecycle Management Competency Centre

SA Spallart-Allmaras

SEM Shell Eco-marathon

WALE wall adapting local eddy

Nomenclature

Ω collision operator

Φ viscous dissipation function

δ Kroneker delta

μ dynamic viscosity

ν macroscopic velocity

ρ density

τ relaxation characteristic time

A area

c velocity

C_D coefficient of drag

C_L coefficient of lift

C_M coefficient of pitching moment

c_p specific heat

C_R coefficient of roll moment

C_S coefficient of side force

c_s speed of sound

C_Y coefficient of yawing moment

d distance nearest to wall

D_ν turbulent wall distruction term

ε kynetic energy dissapation ratio

f distribution function

F_D drag force

F_L lift force

f_v viscous damping function

g gravity

k thermal conductivity

L eddy size

$\tilde{\nu}$ kinematic viscosity

ν_t turbulent viscosity
 Ω_{ij} mean rate-of-rotation tensor
 p_w wall pressure
 P_ν turbulent production term
 r lattice position
 Re Reynolds number
 S magnitude of vorticity
 \tilde{S} modified vorticity
 T temperature
 t time
 τ_w turbulent wall shear stress
 U mean velocity
 u_p velocity of adverse wall pressure gradient
 u_τ skin friction velocity
 β yawed flow angle
 v_∞ free stream velocity
 y^+ normal distance from the wall

Chapter 1

Introduction

1.1 Background

Due to environmental effect, more efficient road vehicles are being developed and improved aerodynamics is needed for the design of optimal body shapes. Only in recent years with the ever increasing fuel price have car manufacturers had a growing interest in low speed aerodynamics. Car companies today are now basing their vehicles on being more aerodynamic, with the main goal to develop clean, efficient and sustainable vehicles for urban transport.

The use of computational fluid dynamics (CFD) to predict aerodynamic flow around vehicles has been on the incline over the last few years due to the increase in computing power available, making it a viable tool for simulating aerodynamic effects [Takagi, 1990][Huminić and Chiru, 2006]. Aerodynamic characteristics of a complex body, near a moving wall as well as having moving components are easily setup in certain CFD software allowing real-world characteristics to be implemented early in the design process. The exponential rise in computing power has prompted the increased use of the lattice Boltzmann method in CFD solvers, this has caused some turbulence in the Navier-Stokes dominant CFD industry. The Navier-Stokes equations describe the behaviour of fluid flow in a continuum approximation, whereas the Boltzmann equation looks at the macroscopic behaviour of a fluid. The similarities and differences between Navier-Stokes and lattice Boltzmann computational simulations have yet to all be described.

The Product Lifecycle Management Competency Centre (PLMCC) at Cape Peninsula University of Technology (CPUT), Bellville campus, makes use of Dassault Systemes (DS) high-end computer aided design (CAD) software, CATIA V6. Technical demos are being developed at the PLMCC for research into eco-electric vehicles, one of their projects is to design and create an electric vehicle for the purpose of competing in the Shell Eco-marathon (SEM) competition. The SEM project allows post graduate students from mechanical engineering, electrical engineering and industrial design to apply their respective research to a virtual product in order to display the different applications of CATIA V6 and the technology available at the PLMCC and CPUT.

The outcomes from this research are integrated into the final manufactured vehicle model for development, testing and ultimately competing in the SEM competition. This work presents some of the capabilities of Next Limit's XFLOW 2014, specifically related to vehicle aerodynamics. Using traditional CFD software, problems of this kind require time consuming model idealisation and remeshing processes, which lead to errors or divergence of the simulation. The particle based and fully Lagrangian, lattice Boltzmann approach of XFLOW, moving parts can be easily handled such as the forced rotation of a vehicles wheels, done solely based on the physical and mechanical properties of the objects. Moreover, full detail vehicle models can be handled while not being limited by the complexity of surface geometry [Holman et al., 2012a]. This paper also aims to present a comparative CFD study of a Shell Eco-marathon 'urban concept' road vehicle using Ansys FLUENT 14.5 against Next Limit XFLOW 2014. The results are obtained from similarly setup simulations and will compare drag and lift data as well as flow visualisations for stationary and rolling road configurations, two refinement levels and two turbulence models. The ability to simulate rotating wheels will also be included and compared using XFLOW only. The combinations of control variables are obtained with the aim of optimising the simulation process and data acquisition.

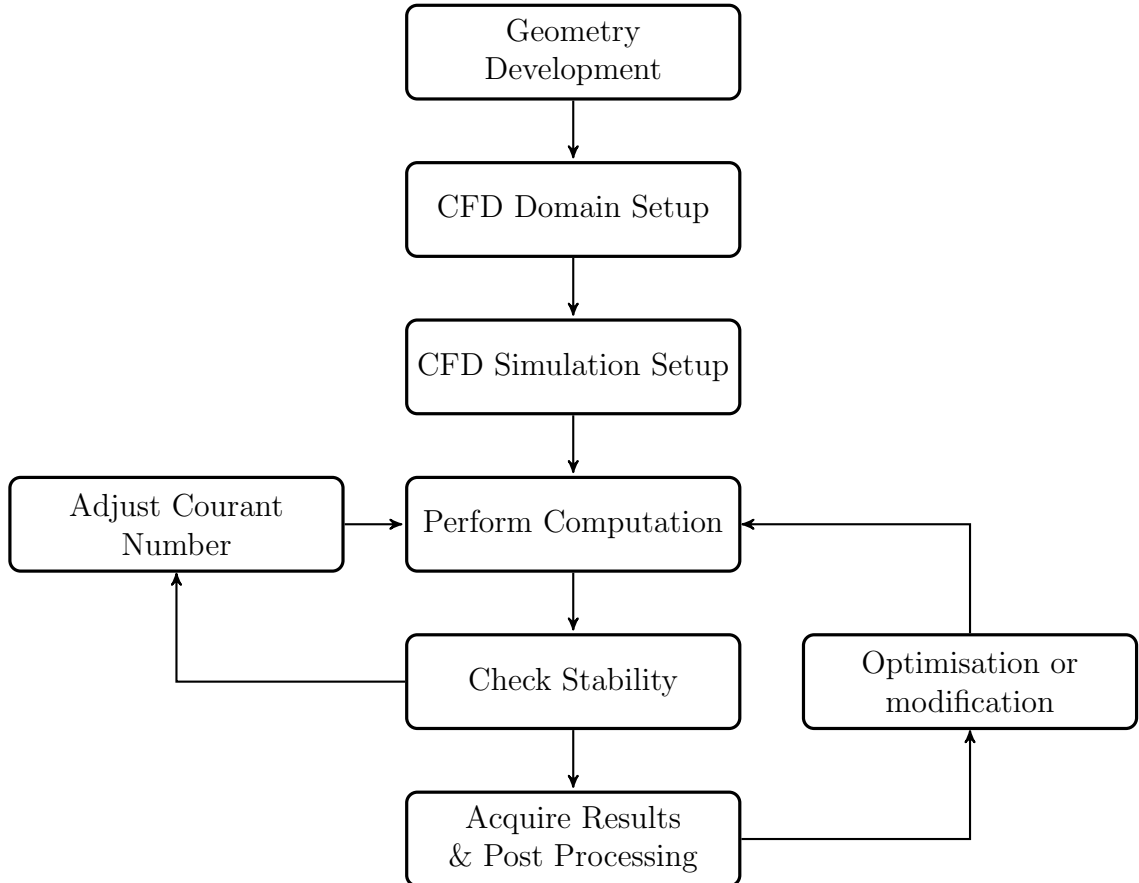
1.2 Literature review

Aerodynamic characteristics of a road vehicle are responsible for energy efficiency from aerodynamic drag, safety aspects such as crosswind stability and vehicle soiling, as well as the environmental influence of a vehicle on its surroundings including air pollution and noise [Hucho, 1987]. The challenge is to accurately simulate very complex fluid phenomena and get results faster in order to successfully implement them in a dynamic design environment with numerous design alterations. The key is to develop CFD early in the design process so that modifications and crucial re-works later are negated [Dhaubhadel, 1996]. Most production vehicle's aerodynamic efficiencies have only ever been represented by a coefficient of drag (C_D) which represents a vehicle's aerodynamic resistance to airflow in the forward direction only, while one of the most important safety factors in passenger vehicles is a resistance to side wind [Hucho, 1987] [Mayer et al., 2007]. Furthermore, aerodynamic drag is increased more during yawed flow when using moving ground in simulations compared to stationary ground conditions [Landström et al., 2010] [Cogotti, 1995]. It is well known that both the local flow field and the global aerodynamic forces are affected by the rotation of the wheels [Wiedemann, 1996] [Kang et al., 2010] [Skea et al., 2000] [Landström et al., 2009] [Sebben, 2001] [Wäschle, 2007] [Mayer and Wiedemann, 2007] [Huminic and Chiru, 2006]. Generally, wheel and wheel cover design is considered only late in the development process; however, designs with detail geometries used in the vehicle's development process allows the potential for drag saving early in the design process [Duncan et al., 2010] [Landström et al., 2011] [Lounsberry et al., 2009]. The aerodynamic development of road vehicles is usually done separately from the suspension. Accelerating, braking and cornering has an effect of the ride height as well as pitching and rolling moments of a vehicle which can lead to large changes of the aerodynamic coefficients [Aschwanden et al., 2008].

The most commonly used numerical methods to discretise equations are the finite difference method (FDM), finite element method (FEM) and finite volume method (FVM). The lattice Boltzmann method (LBM) is a microscopic-based approach for resolving fluid flow phenomena at macroscopic scales. The advantage of large eddy simulation (LES) with the LBM is that the transient processes can be examined in detail which is difficult to achieve in experiments [Krajnovic and Davidson, 2002] and only with a hybrid-LES in Reynolds averaged Navier-Stokes (RANS) equations. LES is formulated on filtering rather than averaging, this method uses the filter size and all flow scales larger than the filter size will be exactly calculated and the scales less than filter size are modeled. LES is thus used for attaining the underlying knowledge about a vehicle’s flow physics.

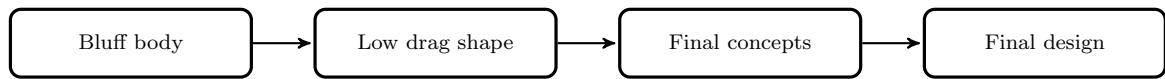
1.3 Aims and objectives

This work aims to present a study on the aerodynamics of a SEM urban concept vehicle, specifically related to the analysis of flow through CFD simulation with the use of Dassault Systemes CATIA V6 parametric 3D CAD software and XFLOW CFD software. The objective is to use the gained understanding of the flow to help the stylist improve the aerodynamic properties throughout the design of the vehicle. CFD will not be limited to predicting the forces and moments acting upon a vehicle, but used to understand the reasons behind them and create objectives for their controlled change. CFD studies require a structured procedure to ensure the uniformity and correctness of simulations.



The objective of this thesis is to develop a framework for a light road vehicle aerodynamic shape optimization. This framework will help car designers and body stylists to effectively evaluate the aerodynamic performance of various body designs and modifications quickly and efficiently at the any stage of vehicle design process. The combinations of control variables are obtained by a process called design of experiments. The design of experiments is a concept that uses a set of selected experiments which are performed with the aim of optimizing a process or a parameter and to draw information on the aerodynamic behaviour against a set of factors which are known to affect the response. The reason for performing a set of designed experiments is to keep the number of simulations as low as possible while obtaining the most information.

This work is broken up into three sections; the first being simplified testing using the Ahmed body, secondly, a simple aerodynamic shape is developed based on the SEM constraints and is used to determine possible low-drag configurations, and finally, the final vehicle model will be determined through a multiple iteration design process along side an industrial designer to develop a vehicle shape that has low-drag and is aesthetically pleasing.



1.3.1 CFD validation

The model chosen for simplified testing and comparison is the Ahmed body, it consists of a simplified vehicle bluff-body which is used as a benchmark for vehicle aerodynamics [Ahmed et al., 1984]. It has been used in several experiments and comprises of a square back, distinct separation lines and is characterised by a low drag shape. The Ahmed bluff-body is free from wheels and accessories, however it retains the primary flow behavior of a road vehicle.

Objectives:

- Compare groundless, stationary road & rolling road configurations

1.3.2 Low-drag concept design

A basic aerodynamic vehicle shape is developed in CATIA V6 to allow the industrial designer to visualise how different vehicle shapes and how they affect the aerodynamics. The simple model can be described as a low drag, bluff body with a Kamm-back that resembles a road vehicle more than that of the Ahmed shape and fits within the SEM constraints. Other factors that influence the shape are driver position, luggage space and provision for electrical components. Its surfaces are easily manipulated allowing the determination of changes to drag, lift and the surrounding flow field. This is used to determine how the basic shape of a vehicle due to its size restrictions (which are bound by the rules of the SEM competition) can be optimised.

Further analysis includes a vehicle model that incorporates basic wheel arches in order to compare wheel geometry and rotation effects on drag and lift. The wheel base and track widths are set at the beginning of the project to their minimum allowable, giving the vehicle the smallest projected area possible as well as allowing it to taper towards the rear.

Objectives:

- Determine low-drag shape based on constraints
- Determine crosswind effects on sharp and round bodies
- Compare stationary and rotating wheels
- Compare simple and detailed geometry wheels

1.3.3 Final design

The design and modeling of the the final SEM vehicle shape and appendages are done collaboratively with an industrial design masters student, this ensures the initial shape has good aesthetics as well as having good aerodynamic characteristics. This way designs that could interfere with the flow characteristics of the vehicle shape and induce drag when not necessary can be ruled out from the start. Three initial concepts are tested with rolling road and detailed rotating wheels before careful analysis determines features of the designs which should be altered to improve the final designs aerodynamics.

The simulation of the detailed final vehicle design takes into account rolling road, rotating wheels and yawed flow.

Objectives:

- Develop low-drag shape design through multiple iterations along side industrial designer
- Analyse flow characteristics and aerodynamic coefficients
- Compare results with Ansys FLUENT
- Optimise with aerodynamic appendages (Rear spoiler, rear diffuser, wheel covers, etc.).

1.4 Dissertation structure

Chapter 2 deals with the aerodynamics background. Before concept designs can be visualised and simulations can be understood a greater understanding of background into fluid mechanics and vehicle aerodynamics. Chapter 3 deals with the numerical methods involved with Reynolds-averaged Navier-Stokes and lattice Boltzmann formulations, including that of turbulence and boundary layer as well as looking at how flow is visualised and interpreted. Chapter 4 deals with the bluff body, low-drag concept and preliminary vehicle concepts geometry development, simulation setup as well as presenting the results and discussions of the simulations. Chapter 5 deals with the results of the preliminary concepts development and simulation. Chapter 6 shows the results from the aerodynamic development, presenting the results and discussions of the simulations. Chapter 7 presents conclusions reached in the framework of this investigation and outlines some research lines that could be undertaken.

1.5 Delineations

- The main limitation to flow simulation, especially in the case of the lattice Boltzmann solver used by XFLOW is computing time. The processing power needed for the simulations comes from the PLMCC's 16 core "Super Computer". However, the license only allowed the usage of a 8 cores and one graphical user interface. Because of this limitation, the simulations required at least 36 hours of iterations before reaching acceptable levels of residuals. Another restriction is the data storage, each simulation stores data up to 70Gb each when the data is not averaged requiring a large amount of storage space for the numerous simulations. These limitations forced the resolution to be as optimised as possible for the simulations in order to save time and storage while ensuring a good accuracy.
- Simulations do not involve any analysis of internal flow due to the vehicle being electrically powered, no vents for cooling are necessary.
- Simulations observe vehicle dynamics due to aerodynamic effects only.
- Simulations do not involve the analysis of any heat effects.
- Simulations will only involve fluid flow which is incompressible.

Chapter 2

Aerodynamics

2.1 Fluid mechanics

Fluid mechanics is the science behind the behavior of fluids at rest and in motion, it plays an important role in the development of road vehicles in terms of vehicle aerodynamics. External fluid flow exerts forces and moments upon a vehicle which greatly influence its performance and directional stability, but is also used to reduce wind noise, cooling for the engine and brakes as well as directing dirt and water away from lights and windows. Aerodynamics is a branch of fluid mechanics which deals with the understanding of how solid objects affect fluid flow and how a fluid in motion induces forces and moments upon solid surfaces. A moving fluid exerts normal pressure and tangential shear forces on a body, these forces make up the drag and lift forces a body experiences. The combinations of these forces tend to move a body in a particular direction depending on the flow. Understanding the flow field around a body enables the calculation of defining properties such as drag and lift as well as specific velocities and pressure for any specific location and time.

A commercial road vehicle is a complex and detailed geometry, usually with both internal and external flows as well as having rotating wheels. The flow over a vehicle is described as fully three-dimensional with turbulent boundary layers and common flow separation followed by reattachment. Turbulent wakes are formed toward the rear and can be shaped as longitudinal trailing vortices. The aerodynamic performance of road vehicles by the automotive industry has for the most part been evaluated through aerodynamic coefficients such as drag, lift and sidewind sensitivity, which are used to improve fuel efficiency or estimate vehicle handling among others. Vehicle design differs from aircraft design as it is not wholly dictated by aerodynamics; style, performance, safety, handling, comfort and production are all important things to consider when designing a vehicle. Aerodynamic development mainly involves fine tuning specific areas of the body, work often starts with a low drag shape which is developed aerodynamically in conjunction with the stylist. The flow region around a vehicle cannot be treated the same way as an aircraft either, it is not possible to distinguish several independent flow fields and the flow field around a vehicle must be treated as a whole [Hucho, 1987]. Most of the aerodynamic design is to prevent or control separation through simulation and testing.

This study focuses on analysing the flow field around a small road vehicle using a commercial CFD software, with emphasis on the external flow effects on a light road vehicle in normal and yawed flow. The maximum velocity to be attainable by the vehicle was predicted at $60\text{Km/hr} = 16.667\text{m/s}$. Due to the velocity being below Mach 0.3 ($\text{Ma} = 0.3 \approx 100\text{m/s}$) and the temperature being low, the assumption is made that the density and viscosity of the fluid can be seen as constant values throughout the simulation. The flow field can then be described as being incompressible and isothermal.

2.1.1 Boundary layer

All experimental observation of fluid in motion show that it comes to a complete stop when it comes into contact with a solid surface, this is known as the non-slip condition. The flow areas around the solid body are affected by the fluid's viscosity, causing a velocity gradient to form close to the surface. This thin layer where the velocity gradient is significant is known as the boundary layer (also known as the non-slip condition), it increases from zero velocity at the surface to the velocity at the free stream. The boundary layer thickness increases away from the surface as it progresses from the front to the rear of the body. The larger boundary layer at the rear of the body means the stagnation pressure is less towards the rear than the front, this effective pressure drop along the length of the body causes the drag force. Despite the thinness of the boundary layer near the wall, it has a strong influence on the flow field around the body. Fluid flow within the boundary layer is categorised into two main groups; laminar and turbulent. In the front most part of the boundary layer the flow is steady and almost parallel to the wall which is known as laminar flow. Further down the body the boundary layer increases in size away from the wall due to the increase in kinematic viscosity, this is known as the turbulent part of the boundary layer. The transition between the two states of flow is governed by the Reynolds number. Reynolds number is a dimensionless parameter that characterises the transition from laminar to turbulent flow in a viscous fluid. It gives a ratio of internal forces to viscous forces for a specific length, however, it is also possible for the fluid flow to transition from laminar to turbulent from disturbances such as surface roughness.

To relate Reynolds number to vehicle aerodynamics it is a function of the velocity of the vehicle, the kinematic viscosity of the fluid and the length of the vehicle. Flows around geometrically similar bodies form the basis for model testing. If the Reynolds numbers are the same for scale models, the results of testing will yield the same dimensionless aerodynamic coefficient results as a full scale test. In general, for the typical operating speeds of commercial vehicles, compressibility can be considered to be negligible and an incompressible viscous fluid model is assumed. Reynolds numbers based on a vehicle body's length are typically high, thus the flow regimes can be assumed to be fully turbulent.

2.1.2 Separation and wake

Vortices and separation occur at certain places on a body and its geometry influences the wake and trailing vortices in the areas immediately around the body as it moves through the air. Flow separation occurs when the boundary layer detaches from the solid body, this is caused when the flow decelerates rapidly also referred to as an adverse pressure gradient. This boundary layer separation causes a large increase of drag on the body. Corners, sharp turns and high angles of attack all lead to energy loss due to boundary layer separation. Where the boundary layer is laminar, the momentum of the fluid cannot handle the increasing pressure and separates from the surface. When the boundary layer is turbulent the momentum is far greater allowing the flow to overcome the adverse pressure gradient, restricting separation. The flow does however tend to naturally separate further downstream. Adding a trip wire that transitions the flow from laminar to turbulent can change where separation occurs on the body. If the flow is tripped and turned turbulent, separation occurs further along the body, which reduces the size of the wake and can be used to reduce drag if done correctly. Drag and lift forces are influenced by the free stream velocity (v_∞), the fluid density and the size, shape and orientation of the body and its position relative to other bodies. For air at low speeds the fluid density varies very little and is regarded as incompressible making it a constant property.

There are two different types of separation that occur; *quasi-two dimensional* and *three dimensional separation*. *Quasi-two dimensional separation* occurs where the flow encounters a perpendicular edge such as between the front and bonnet, this separation is characterised as a high degree of turbulence and often is able to reattach further downstream. This type of separation also occurs when the flow of air over the vehicle separates near the rear, it produces a large low pressure turbulent region behind the vehicle known as the wake which contributes to the formation of pressure drag. *Three dimensional separation* occurs around the edges of the vehicle where the flow separates at an angle and induces trailing vortices in the wake region. Simple smooth surface vehicle configurations, free from wheels and appendages are able to exhibit a range of *quasi two dimensional* and fully *three dimensional* separated flows with the largest being the trailing wake. The separated flow regions are able to exhibit kinematic macro structures in a time-averaged sense and those that are present in the wake greatly influence most of the drag experienced by the body.

2.2 Vehicle aerodynamics

2.2.1 Forces and moments

Vehicle dynamics refers to the motion of a vehicle and the various forces that act upon it when it is in motion. The dynamic responses of a vehicle due to the disturbance in the air around it are governed by the vehicles aerodynamic derivatives coupled with the tyre and suspension characteristics. Six components or degrees of freedom (DOF) make up the vector of the total resulting forces and moments experienced by the vehicle. For no side-wind or symmetrical flow ($\beta = 0$), the vehicle experiences drag

and lift forces along X and Y respectively are accompanied by a pitching moment M with respect to the z axis about the vehicle's centre of gravity (Figure 2.1). A vehicle's centre of gravity becomes an important factor for cornering and stability; a lower centre of gravity allows a more level and stable ride from the suspension, especially during cornering. A known centre of gravity can be used to evaluate the forces acting upon the four wheels of the vehicle.

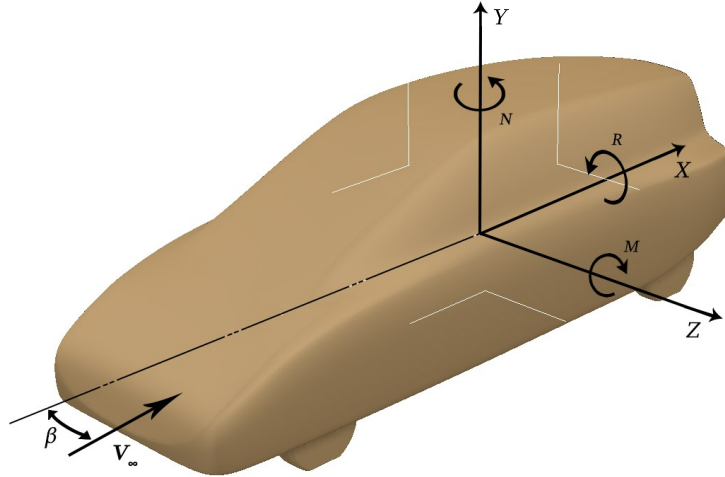


Figure 2.1: Vehicle axis and moments

For conditions with side-wind or asymmetrical flow field, additional forces and moments occur. A side force along Z exists as well as a rolling moment R with respect to the x axis and a yawing moment N with respect to the y axis (Figure 2.1).

The resulting forces and moments from yawed flow must be balanced out by the reaction forces through the suspensions and grip of the tyres. The side-wind sensitivity of a vehicle must be considered from how it affects the vehicle economically and how much the driver has to compensate to correct the lateral effects and the forces that are induced onto components on the vehicle side. The aerodynamic force on the side of a vehicle results from a difference in pressure between the windward side and the leeward side. Only a small pressure force exists on the windward side of the vehicle, however on the leeward side a considerable negative pressure force occurs due to boundary layer separation developing a side wake. This negative pressure region on the leeward side is the main cause of the yawing moment which defines a vehicle's stability. A yawed flow on a vehicle will in turn causes a further increasing angular deviation of the angle β . It is possible to reduce the side force and yawing moment by stalling the flow by having sharp edges on the front corners, this however will increase vehicle drag [Hucho, 1987].

2.2.2 Flow coefficients

Dimensionless flow coefficients are used to represent a bodies reaction to the forces and moments induced on it by fluid flow. These give comparable figures that represent a bodies resistance or sensitivity to a certain flow. The most common coefficients used when determining how aerodynamic a vehicle is, are the drag (C_D) and lift (C_L) coefficients as shown in equation 2.1 and 2.2 respectably. Similarly there exists coefficients for pitching moment C_M , side force C_S , rolling moment C_R and yawing moment C_Y .

$$C_D = \frac{F_D}{2\rho Av_\infty^2} \quad (2.1)$$

$$C_L = \frac{F_L}{2\rho Av_\infty^2} \quad (2.2)$$

Where C_D and C_L are the drag and lift coefficients respectably, F_D and F_L are the force due to drag and lift respectably, ρ is the density, v_∞ is the velocity of the free stream and A is the projected frontal area of the vehicle.

The coefficient of drag is primarily used by production car companies in vehicle specification. To achieve a C_D of 0.5, not much aerodynamic design has to be done, a C_D of 0.4 requires months of aerodynamic design and testing including scale model wind tunnel tests. A drag coefficient of 0.3 for a production car requires several months testing including full-scale wind tunnel testing [Hucho, 1987]. The most aerodynamic production vehicle at the time of this paper is the VW XL1, with a C_D of 0.19.

2.2.3 Vehicle aerodynamic aspects

Unsteady flow

The aerodynamic development of production vehicles is usually performed through disregarding unsteady aerodynamic effects on the handling of a vehicle, where the gustiness that is essential in natural wind conditions is not reproduced. Furthermore, aerodynamic testing typically uses steady-state conditions, howbeit the on-road environment is highly unsteady [Fares, 2006] [Lawson et al., 2007] [Schroeck et al., 2011].

Yawed flow

Most production vehicle's aerodynamic efficiencies have only ever been represented by a coefficient of drag (C_D), which represents a vehicle's aerodynamic resistance to airflow in the forward direction only while one of the most important safety factors in passenger vehicles is a resistance to side-wind which can cause a vehicle to veer off-course, causing the driver to correct. Side-wind sensitivity of a vehicle is typically analysed with the vehicle rotated with respect to the wind tunnel flow, creating the resultant flow from a side-wind [Mayer et al., 2007]. It is also possible to recreate the aerodynamics of a vehicle during cornering using this method with the wheel geometries rotated to the correct position for steering.

Rolling road

A rolling road causes the floor boundary layer to affect the drag and lift coefficients as well as the pitch moment coefficient [Olsen et al., 2014][Hennig et al., 2011] especially at low ground clearances [Fago et al., 1991]. It has also been shown that the use of a rolling road can reduce drag by 8% and lift by 16%, as well as a showing a difference in the nature of flow surrounding a vehicle which has the greatest effect at the floor and on the rear surface of a vehicle, with the wake relatively insensitive to the floor movement [Krajnović and Davidson, 2005][Bearman et al., 1988]. Furthermore, aerodynamic drag increases more during yawed flow when using moving ground simulations when compared to stationary ground conditions [Landström et al., 2010][Cogotti, 1995].

Rotating wheels

Wind tunnel tests have included moving ground systems with rotating wheels during the last decades with numerous studies on the effects of rotating wheels and the importance of wheel aerodynamics being duly noted [Wiedemann, 1996][Kang et al., 2010][Skea et al., 2000]. Different studies point to the most substantial effect from rotating the wheels being the interference effects between the rear wheels and the underfloor [Landström et al., 2009][Sebben, 2001]. It is known that the wheel rotation of an isolated wheel as well as wheel in the wheel arch configurations cause a reduction in drag and lift and are based on numerous effects of the airflow. These forces have been seen to decrease towards the front wheel due to the rotation of the wheel influencing directly on the vehicle body. This increase in aerodynamic efficiency of the vehicle caused by the wheel rotation can also be attained to the interaction between the wakes of the rear wheels and the car's rear end. The use of wheel rotation is thus essential for aerodynamic design and shape optimisation [Wäschle, 2007][Mayer and Wiedemann, 2007][Huminić and Chiru, 2006].

Detailed wheel geometries

Typically, wheel and wheel cover design is investigated late in the development process, however with detail geometries used in the vehicle's development process allows the potential for drag saving early in the design process [Duncan et al., 2010] [Landström et al., 2011] [Lounsberry et al., 2009].

Dynamic suspension

The aerodynamic development of production vehicles is typically done in isolation from the suspension. Accelerating, braking and cornering have an effect of the ride height as well as pitching and rolling moments of a vehicle which can lead to large changes of the aerodynamic coefficients [Aschwanden et al., 2008].

2.2.4 Vehicle aerodynamic design

A low coefficient of drag is a prerequisite for good fuel economy, however other aspects of vehicle aerodynamics can determine dirt build-up and the aerodynamic noise generated by unsteady flow separation which hinders vehicle safety and operating comfort. Depending on the specific purpose of the vehicle, the objectives of aerodynamic design can widely differ. While all road vehicles desire low drag, other aerodynamic properties are, if not more significant. Downforce is imperative for the high speed cornering capability of race cars, but is of no importance for heavy trucks. Cars and vans should have low sensitivity to cross wind, however, heavy trucks not. Cars and buses should have low wind noise but this is of no significance for race cars.

The main purpose of analysing vehicle aerodynamics is to determine the the relationship between cause and effect, if each specific detail of a vehicle could be optimised the minimum aerodynamic drag would be obtained. However, the high interaction between details limits the method of detail optimisation [Hucho et al., 1976]. The method of detail optimisation can be used on a vehicle provided by the stylist. Various zones of a vehicle are defined in order to reduce the drag of a vehicle, these zones for a hatch-back type vehicle are shown in figure 2.2 below, with the zones described along side it, these zones are where most of the drag can be eliminated.

1. round front end
2. cooling duct optimised
3. bonnet slope
4. windscreen slope
5. roof camber
6. rear slope
7. rear diffuser
8. covered wheels
9. smooth underside
10. round wheel-well
11. wheel fairing
12. top view taper
13. windscreen curve
14. A-pillar round
15. C-pillar inswept
16. rear end boat tail

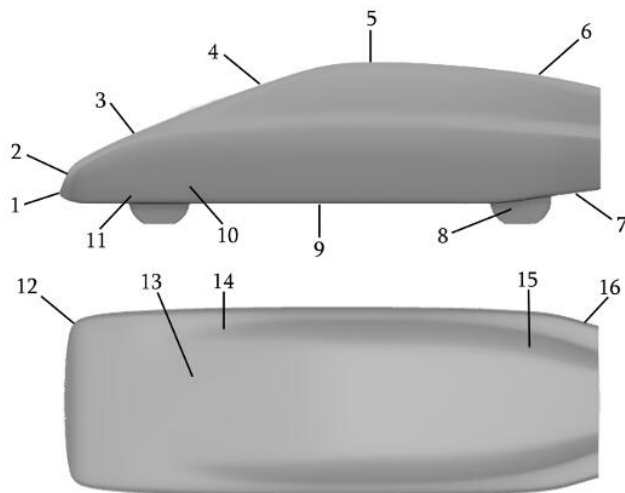


Figure 2.2: Vehicle contours

Detail optimisation is however limited, when a corner is rounded to a point where the air flows around it without separation, further increasing this corner radius will not provide any more reduction in drag. Assuming detail optimisation occurs after a stylistic concept has been given, the drag coefficient can only be brought down to around 0.40 for any stylistic concept [Hucho, 1987] and can only be brought lower by starting with a low drag shape [Hucho et al., 1976].

A low drag shape starts with a streamlined basic body that has the main dimensions of the vehicle (length, width, height). The basic requirements for a low drag shape

are a flat but well rounded front, a curved windshield and a tapering rear. From this shape all the characteristics of a styling model are slowly added and optimised. Rounding of the rear pillars is frequently used to reduce drag which however results in increasing the yaw moment. It can be said that any shape modifications that improves drag resistance may cause a negative effect on the lift force and yaw moment. Flow separation can be manipulated into early separation by adding strakes before the flow reaches the body end and creates a wake. This is a regular design feature used on many vehicles to reduce the yaw moment gradient, drag and lift. They are usually placed on the rear pillars, on side mirrors, along the side of the rear windscreen, or in the front and rear light moulding. Strakes act like trip wires and work by forcing flow separation by prohibiting the air accelerating around curved surfaces resulting in low pressure zones, while reducing unsteadiness in the flow field.

Another method of reducing a vehicle's aerodynamic drag is by modifying certain components or adding suitable attachments. Recent market trends necessitate the use of aerodynamic devices to improve aerodynamic characteristics of a road vehicle. However, due to their complex shape, few computational studies of some of these devices have been performed.

Chapter 3

CFD

3.1 Introduction

Traditional calculations involving flow analysis limit the accuracy of solving and visualising fluid-flow scenarios. This is particularly true of flows that are three dimensional and turbulent. Computational fluid dynamics (CFD) is a powerful tool that considers all fluid properties and overcomes many of the restrictions found in traditional fluid flow analysis. The exponential rise of computational power has allowed very complex 3D simulations including multiple vehicles in full detail. CFD can be used to simulate some hard to reproduce experimental conditions or to investigate hard to measure variables [Anderson et al., 1995].

CFD is based on non-linear partial differential equations which attempt to computationally model theoretical and experimental models. The level of accuracy desired from CFD results is dependent on the requirement of the results. From the perspective of vehicle design, a conceptual design may require only the trends in drag coefficient whereas a detailed design may require accurate determination of the flow characteristics. Since the goal of this study was to obtain the trends in drag and lift coefficients for the development and validation of the proposed framework, qualitative simulations were required. There are two principal methods to simulating heat, mass and momentum transport; continuum and discrete. Using the continuum approach and applying conservation laws; ordinary or partial differential equations can be realised for an infinitesimal control volume. Finite difference, finite volume, finite element, etc., methods along with initial and boundary conditions are then used to convert the differential equations into a system of algebraic equations which can be solved iteratively until convergence is achieved. Next the domain is discretised into volume, grids or elements depending on the solution scheme. This can be imagined macroscopically as each volume, grid or element containing a huge number of particles of which an average or nodal value for velocity, pressure, temperature etc., are represented over a finite volume or assumed linearly or bi-linearly varying between nodes. The sources of errors and uncertainty in CFD results are due to factors such as truncation error between the differential equation solution and the finite equation, spatial discretisation scheme, mesh resolution and iterative convergence [Slater, 2008].

3.2 Conservation

Before any simulations can be done, the laws of conservation that are applied to the virtual wind tunnel must be laid out [Cengel and Cimbala, 2009].

Conservation of mass - the amount of mass in the system remains constant, equal amounts of mass enter and leaves the control volume of the system.

$$\text{Continuity equation} : \quad \frac{\partial u}{\partial x} + \frac{\partial v}{\partial y} + \frac{\partial w}{\partial z} = 0 \quad (3.1)$$

Conservation of Linear Momentum - the relationship between the pressure, viscous forces and momentum in the system. These equations are also known as the Navier-Stokes equations.

$$\begin{aligned} \rho g_x - \frac{\partial p}{\partial x} + \mu \left(\frac{\partial^2 u}{\partial x^2} + \frac{\partial^2 u}{\partial y^2} + \frac{\partial^2 u}{\partial z^2} \right) &= \rho \frac{du}{dt} \\ \rho g_y - \frac{\partial p}{\partial y} + \mu \left(\frac{\partial^2 v}{\partial x^2} + \frac{\partial^2 v}{\partial y^2} + \frac{\partial^2 v}{\partial z^2} \right) &= \rho \frac{dv}{dt} \\ \rho g_z - \frac{\partial p}{\partial z} + \mu \left(\frac{\partial^2 w}{\partial x^2} + \frac{\partial^2 w}{\partial y^2} + \frac{\partial^2 w}{\partial z^2} \right) &= \rho \frac{dw}{dt} \end{aligned} \quad (3.2)$$

Conservation of energy - energy cannot be created or destroyed within the system.

$$\rho c_p \frac{dT}{dt} = k \nabla^2 T = \Phi \quad (3.3)$$

Where ρ is density, g is gravity, μ is dynamic viscosity, Φ is the viscous dissipation function, k is thermal conductivity, T is temperature, c_p is specific heat and t is time.

3.3 Reynolds-averaged Navier-Stokes

The Reynolds-averaged Navier-Stokes (RANS) equations are time-averaged equations for the motion of fluid flow and are largely used for representing turbulent flows. The properties of flow turbulence gives approximate time-averaged solutions to the Navier-Stokes equations [Cengel and Cimbala, 2009]. A shortcoming of the most RANS solvers is their inherent incapacity to deal with greatly separated flows apparent in many logical structures [Ferziger and Perić, 2002].

The Reynolds-averaged Navier-Stokes non-linear equations are not analytically solvable. In the RANS approach splits the instantaneous velocity and pressure into a fluctuating and average components, Equations (3.4) and (3.5)

$$\bar{u} = \frac{1}{T} \int_0^T u dt \quad (3.4)$$

$$\begin{aligned} p &= \bar{p} + p' \\ u &= \bar{u} + u' \\ v &= \bar{v} + v' \\ w &= \bar{w} + w' \end{aligned} \quad (3.5)$$

From the Navier-Stokes equation, inserting *Reynolds decomposition* will result in the continuity equation giving the new fluctuating terms, Equations (3.6) and (3.7).

$$\frac{\partial \bar{u}}{\partial x} + \frac{\partial \bar{v}}{\partial y} + \frac{\partial \bar{w}}{\partial z} = 0 \quad (3.6)$$

$$\rho g_x - \frac{\partial \bar{p}}{\partial x} + \frac{\partial}{\partial x} \left(\mu \frac{\partial \bar{u}}{\partial x} - \rho \bar{u}'^2 \right) + \frac{\partial}{\partial y} \left(\mu \frac{\partial \bar{u}}{\partial y} - \rho \bar{u}'v' \right) + \frac{\partial}{\partial z} \left(\mu \frac{\partial \bar{u}}{\partial z} - \rho \bar{u}'w' \right) = \rho \frac{d\bar{u}}{dt} \quad (3.7)$$

New unknown terms known as *Reynolds stresses* [Cengel and Cimbala, 2009] now exist which cause a *closure problem* resulting in these stresses having to be modeled in order to get a closed system on equations. This is done by introducing turbulence models.

3.4 Lattice Boltzmann

Another way in which flow analysis can be done is to consider the medium to be microscopic, as in made up of small particles which collide with each other. At each time step it is required to identify each particles location and trajectory, making it impossible to be used for large scale simulations as well as having no definition for viscosity, temperature, pressure, etc.. In the literature there are several mesh-less numerical methods to solve CFD. Three main categories are used to describe the behavior of a fluid; algorithms modeled at molecular level, algorithms modeled at a macroscopic level and methods based on a mesoscopic framework, namely the lattice gas automata (LGA) and lattice Boltzmann method (LBM) [Higuera and Jimenez, 1989][Chen and Doolen, 1998]. The LGA and LBM methods have been extensively researched in recent years due to their affinity to computational ability. LBM has the advantage of being easily applied to complex domains and there is no requirement to solve Laplace equations at each time step in order to satisfy the incompressible, unsteady flow continuity as it is with RANS. However, LGA and LBM schemes require more computing memory compared with a RANS solver. The main disadvantage of LGA and LBM schemes is the complexity to theoretically analyse the emergent behavior of the system at macroscopic level from the laws imposed at mesoscopic level [McNamara and Zanetti, 1988],

as well as simulations of the incompressible Navier-Stokes equations, especially for unsteady flows [He and Luo, 1997]. XFLOW's approach to fluid physics takes the ideas behind these methods and extends them to overcome most of the limitations.

Lattice gas automata

LGA models solve the behaviour of gases as particles moving discretely in a d -dimensional lattice in a predetermined direction at discrete times $t = 0, 1, 2, \dots$ and with velocity $v_i, i = 0, \dots, b$, also predetermined. The particles collisions are controlled to preserve mass and linear momentum for any specific position in the lattice [McNamara and Zanetti, 1988][Holman et al., 2012b].

The most basic LGA scheme is the HPP, developed by Hardy, Pomeau and de Pazzis, this scheme allows particles move in four directions on a two-dimensional square grid [Hardy et al., 1976]. The position of an element in the lattice at instant t is given by the occupation number $n_i(r, t)$, with $i = 0, \dots, b$, being $n_i = 1$ presence and $n_i = 0$ absence of particles moving in direction i [Holman et al., 2012b].

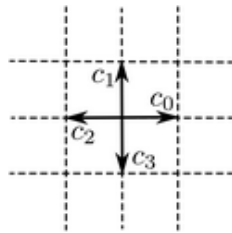


Figure 3.1: HPP model

The equation that governs the evolution of the system is as follows:

$$n_i(r = c_i \Delta t, t = \Delta t) = n_i(r, t) + \Omega_i(n_1, \dots, n_b) \quad (3.8)$$

Where Ω_i is the collision operator, which for each previous state (n_1, \dots, n_b) computes a post-collision state (n_1^C, \dots, n_b^C) conserving the mass, linear momentum and energy; r is a position in the lattice and c_i a velocity.

A system is governed by a number of elements which are macroscopically equivalent to the system that is required to be studied.

The macroscopic density and linear momentum are:

$$\rho = \frac{1}{b} \sum_{i=1}^b n_i, \quad (3.9)$$

$$\rho v = \frac{1}{b} \sum_{i=1}^b n_i c_i \quad (3.10)$$

Boltzmann's transport equation

Boltzmann's transport equation is defined as follows:

$$f_i(r + c_i\Delta t, t + \Delta t) = f_i(r, t) + \Omega_i^B(f_1, \dots, f_b) \quad (3.11)$$

Where f_i is the distribution function in the direction i and Ω_i^B is the collision operator.

From this equation the compressible Navier-Stokes equations can be recovered by means of the Chapman-Enskog expansion [Qian et al., 1992]. The Chapman-Enskog expansion shows the possibility of LGA schemes that allow the recovery of hydrodynamic macroscopic behaviour at low Mach numbers [Holman et al., 2012b].

Lattice Boltzmann method

While LGA methods use discrete numbers to characterise the state of the particles, LBM uses statistical distribution functions containing variables, thus conserving mass, linear momentum and energy [Higuera and Jimenez, 1989][Chen and Doolen, 1998][Succi, 2001]. The collision operator can be simplified under the Bhatnagar-Gross-Krook (BGK) approximation giving a scheme which replicates the hydrodynamic system for low Mach numbers [McNamara and Zanetti, 1988]. The use of the lattice BGK model allows for more efficient computations while allowing the transport coefficients to have flexibility. This operator is defined as follows:

$$\Omega_i^{BGK} = \frac{1}{\tau}(f_i^{eq} - f_i) \quad (3.12)$$

Where f_i is the local equilibrium function and τ is the relaxation characteristic time (which relates to the macroscopic viscosity).

The equilibrium distribution function can adopt the following expression:

$$f_i^{eq}(r, t) = t_i \rho \left(1 + \frac{c_{i\alpha} v_\alpha}{c_s^2} + \frac{v_\alpha v_\beta}{2c_s^2} \left(\frac{c_{i\alpha} c_{i\beta}}{c_s^2} - \delta_{\alpha\beta} \right) \right) \quad (3.13)$$

Where c_s is the sound speed, v the macroscopic velocity, δ the Kronecker delta, and t_i are for preserving the isotropy in space.

LBM is classified as a function of the spatial dimensions d and the number of distribution functions b , which is described in the notation $DdQb$. The most common two dimensional schemes are the $D2Q7$ and $D2Q9$, while three dimensional schemes most used are the $D3Q13$, $D3Q15$, $D3Q19$ and $D3Q27$ as seen below:

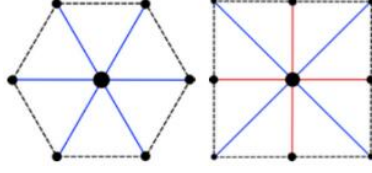


Figure 3.2: $D2Q7$ and $D2Q9$ schemes

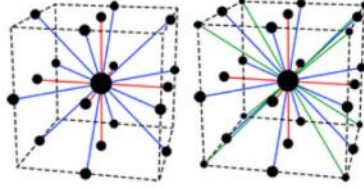


Figure 3.3: $D3Q19$ and $D3Q27$ schemes

The multiscale Chapman-Enskog expansion resolves the relation between the macroscopic viscosity and the relaxation parameter:

$$\nu = c_s^2 \left(\tau - \frac{1}{2} \right) \quad (3.14)$$

For a positive viscosity, the relaxation time has to be greater than 0.5. Using these schemes allow the modeling of a wide range of viscosities $(0, \infty)$ in an efficient way, even with explicit formulations [Holman et al., 2012b].

3.5 Turbulence

Following the dimensional analysis proposed by Kolmogorov at high Reynolds numbers, the flow tends to break in smaller eddies to transform the kinetic energy into internal energy. This process is known as the *Kolmogorov cascade* and it explains the turbulence phenomenon.

The time necessary to break an eddy in the flow is in the order of:

$$t_{break} \sim \frac{L_{eddy}}{\nu_{eddy}} \quad (3.15)$$

and the time to dissipate the kinetic energy through viscosity is expressed as:

$$t_{dissip,visc} \sim \frac{L_{eddy}^2}{\nu} \quad (3.16)$$

For large eddies and high Reynolds numbers, the break time is smaller than the time employed to dissipate the energy and this produces the *Kolmogorov cascade*.

The kinetic energy of a turbulent structure can be estimated by:

$$E_{c\ eddy} \sim V_{eddy}^2 \quad (3.17)$$

The specific kinetic energy dissipation ratio is as follows:

$$\varepsilon_{break} \sim \frac{V_{eddy}^2}{t_{break}} = \frac{V_{eddy}^3}{L_{eddy}} \quad (3.18)$$

The smallest eddies present in the flow (of size $\sim L_{critical}$) have a break time equal to the time necessary to transform their kinetic energy to viscous energy ($t_{break} \sim t_{dissip,visc}$). Then the kinetic energy dissipation ratio can be estimated by:

$$\varepsilon_{viscous} \sim \frac{V_{critical}^3}{L_{critical}} \sim \frac{\nu^3}{L_{critical}^4} \sim \frac{V_{eddy}^3}{L_{eddy}} \sim \varepsilon_{break} \quad (3.19)$$

and thus,

$$\frac{L_{eddy}}{L_{critical}} \sim \frac{V_{eddy}^3 L_{eddy}^3 L_{critical}^3}{\nu^3 L_{eddy}^4} = \frac{L_{critical}^3}{L_{eddy}^3} Re_{eddy}^3 \quad (3.20)$$

Finally,

$$\frac{L_{critical}}{L_{eddy}} \sim Re_{eddy}^{-3/4} \quad (3.21)$$

Taking into account this relationship, if we want to explicitly solve every eddy in a three-dimensional flow, the number of elements is in the order of:

$$N_{elements} \sim \left(\frac{L_{eddy}}{L_{critical}} \right)^3 \sim Re_{eddy}^{9/4} \quad (3.22)$$

The RANS approach models the turbulence in a global way, this is the most widely adopted approach. As it calculates values averaged in time, the approach removes the time dependence of the solution. Although calculating averaged results is computationally less expensive, new terms appear in the Navier-Stokes equations that have to be modeled by new transport equations. Moreover there are several RANS models, each one suitable for a specific problem, and the parameters of each model need to be adjusted empirically.

Another approach to turbulence modeling is the Large Eddy Simulation (LES). This approach solves turbulence locally by modeling only the smallest scales which is closer to the real physics. The smallest scales of turbulence have been extensively

studied and the behavior can be replicated without the use arbitrary parameters. In LES, an additional viscosity called eddy viscosity, or subgrid-scale viscosity, is introduced in order to model the turbulence.

$$\nu_{effective} = \nu_{molecular} + \nu_{turbulent} \quad (3.23)$$

Wall-Adapting Local Eddy

The wall adapting local eddy (WALE) viscosity turbulence model has excellent properties both near to and far from the wall and both for laminar and turbulent flows. The turbulent boundary layer can be directly solved when the asymptotic behavior is recovered and it does not have to create additional turbulent viscosity in the shear regions of the wake [Ducros et al., 1999]. The WALE model is formulated as follows:

$$\nu_{turbulent} = \Delta^2 \frac{(G_{\alpha\beta}^d G_{\alpha\beta}^d)^{3/2}}{(S_{\alpha\beta} S_{\alpha\beta})^{5/2} + (G_{\alpha\beta}^d G_{\alpha\beta}^d)^{5/4}} \quad (3.24)$$

$$S_{\alpha\beta} = \frac{1}{2} \left(\frac{\partial v_\alpha}{\partial r_\beta} + \frac{\partial v_\beta}{\partial r_\alpha} \right) \quad (3.25)$$

$$G_{\alpha\beta}^d = \frac{1}{2} (g_{\alpha\beta}^2 + g_{\beta\alpha}^2) - \frac{1}{3} \delta_{\alpha\beta} g_{\gamma\gamma}^2 \quad (3.26)$$

$$g_{\alpha\beta} = \frac{\partial v_\alpha}{\partial r_\beta} \quad (3.27)$$

$$\Delta = c_w Vol^{1/3} \quad (3.28)$$

Where the WALE constant (c_w) is typically 0.32

Spalart-Allmaras

The Spalart-Allmaras (SA) turbulence model was used in the Reynolds Averaged Navier Stokes Equations model. The SA model was found to be suitable for flow over structures, shear layer detail and attached wall bounded flows. Its disadvantages include inaccuracy for greatly separated flows, degenerating turbulence and internal flows [Ashgriz and Mostaghimi, 2002] The transport equation for the kinematic viscosity ($\tilde{\nu}$) is the working variable for the Spalart-Allmaras model [Allmaras and Johnson, 2012][Fluent, 2012], is given by

$$\frac{\partial(\rho\tilde{\nu})}{\partial t} + \frac{\partial(\rho\tilde{\nu}u_k)}{\partial x_k} = P_\nu + \frac{1}{\sigma_\nu} \left[\frac{\partial}{\partial x_k} \left\{ (\nu + \tilde{\nu}) \frac{\partial \tilde{\nu}}{\partial x_k} \right\} + C_{b2} \rho \frac{\partial}{\partial x_k} \left(\frac{\partial \tilde{\nu}}{\partial x_k} \right) \right] - D_\nu \quad (3.29)$$

The turbulent viscosity is then given by

$$\nu_t = \rho \tilde{\nu} f_{v1} \quad (3.30)$$

where the viscous damping function is given by

$$f_{v1} = \frac{\chi^3}{\chi^3 + C_{v1}^3} \quad (3.31)$$

with $\chi \equiv \frac{\tilde{\nu}}{\nu}$

The turbulent production term in Equation (3.29) is given by

$$P_\nu = C_{b1} \rho \tilde{S} \tilde{\nu} \quad (3.32)$$

where the modified vorticity is defined as

$$\tilde{S} = S + \frac{\tilde{\nu}}{\kappa^2 + d^2} f_{v2} \quad (3.33)$$

with

$$f_{v2} = 1 - \frac{\chi}{1 + \chi f_{v1}} \quad (3.34)$$

with $S \equiv \sqrt{2\Omega_{ij}\Omega_{ij}}$ being the magnitude of the vorticity. The vorticity is found from the mean rate-of-rotation tensor:

$$\Omega_{ij} = \frac{1}{2} \left(\frac{\partial u_i}{\partial x_j} - \frac{\partial u_j}{\partial x_i} \right) \quad (3.35)$$

The variable d is the distance to the nearest wall in the standard RANS model.

The turbulent wall destruction term in Equation (3.29) is given by

$$D_\nu = C_{b1} \rho f_w \left[\frac{\tilde{\nu}}{d} \right]^2, \quad (3.36)$$

with $f_w = g \left[\frac{1+C_{w3}}{g^6+C_{w3}} \right]^{\frac{1}{6}}$, $g = r + C_{w2}(r^6 - r)$, $r = \frac{\tilde{\nu}}{S\kappa^2 d^2}$,

The parameter $C_{w1} = \frac{C_{b1}}{\kappa^2} + \frac{(1+C_{b1})}{\sigma_\nu}$. The Spalart-Allmaras parameters input into FLUENT by the user does not include κ or σ_ν but the rest of the parameters can be modified with the values used given in table Table 3.1.

Table 3.1: Spalart-Allmaras Turbulence model parameters

C_{b1}	0.1355
C_{b2}	0.622
C_{v1}	7.1
C_{w2}	0.3
C_{w3}	2.0
σ_ν	2/3
κ	0.4187
Pr	0.667

3.6 Boundary Layer

When a fluid flows next to a body, a boundary layer of slower moving fluid is created near the surface. Closest to the body the velocity of the flow is equal to that of the solid, this is known as the *non-slip condition*. The velocity of the fluid increases toward the freestream velocity, boundary layer thickness is defined as the distance from the surface to where the velocity reaches 99% of the freestream velocity. Boundary layer can be categorised into three types of flow, laminar, turbulent and a combination of both. The fluid flow can be said to start as laminar and as it progresses along the length of the body, the flow becomes turbulent. Wall functions assume that the flow near the wall behaves in a fully turbulent manner and use an algorithm to resolve the gradients in the boundary layer [Fluent, 2012].

Moving boundary conditions are treated similarly to the handling of fixed boundaries, in simple LBM configurations the wall boundary conditions for straight boundaries are resolved by following a *bounce-back* rule for the non-slip condition and a *bounce-forward* rule for the free-slip condition. In XFLOW the reconstruction of the statistical distribution functions is done by taking into account the distance from the wall, the velocity as well as the wall properties and behaviour, this is then recomputed each time-step taking into consideration the new position of the moving boundaries. As the fluid physics are implemented rather than the surface elements, XFLOW relaxes the geometry requirements and is tolerant to intersecting or advanced surfaces. Finally, the under-resolved scales at the boundary layer are taken into account by a unified non-equilibrium law of the wall model. The boundary condition used to define a surface that has no velocity perpendicular to it is known in XFLOW as the *enhanced wall-function*.

The wall function includes the effect of changing pressure gradients in order to model the boundary layer. The wall function is valid for all y^+ and accurately resolves the turbulent boundary layer taking into account also for the influence of curvature and pressure gradient. The formulation of this wall function is as follows:

$$\begin{aligned}\frac{U}{u_c} &= \frac{U_1 + U_2}{u_c} = \frac{u_\tau U_1}{u_c u_\tau} + \frac{u_p U_2}{u_c u_p} \\ &= \frac{\tau_w}{\rho u_\tau^2} \frac{u_\tau}{u_c} f_1\left(y^+ \frac{u_\tau}{u_c}\right) + \frac{dp_w/dx}{|dp_w/dx|} \frac{u_p}{u_c} f_2\left(y^+ \frac{u_p}{u_c}\right)\end{aligned}\quad (3.37)$$

$$y^+ = \frac{u_c y}{\nu} \quad (3.38)$$

$$u_c = u_\tau + u_p \quad (3.39)$$

$$u_\tau = \sqrt{|\tau_w|/\rho} \quad (3.40)$$

$$u_p = \left(\frac{\nu}{\rho} \left| \frac{dp_w}{dx} \right| \right)^{1/3} \quad (3.41)$$

Where y^+ is the perpendicular distance from the wall, u_τ is the skin friction velocity, τ_w is the shear stress of the turbulent wall, dp_w/dx is the wall pressure gradient, u_p is the adverse wall pressure gradient characteristic velocity and U is the mean velocity at a given distance from the wall.

The interpolating functions f_1 and f_2 are depicted as follows:

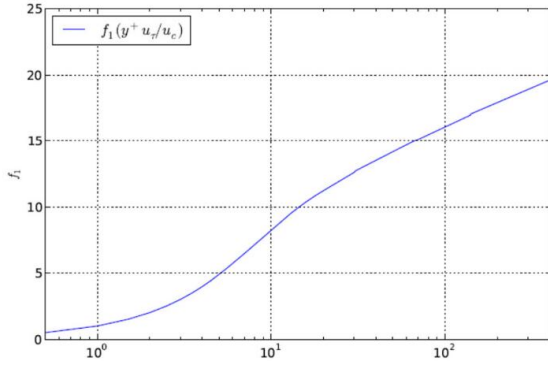


Figure 3.4: $f_1(y^+ u_\tau / u_c)$

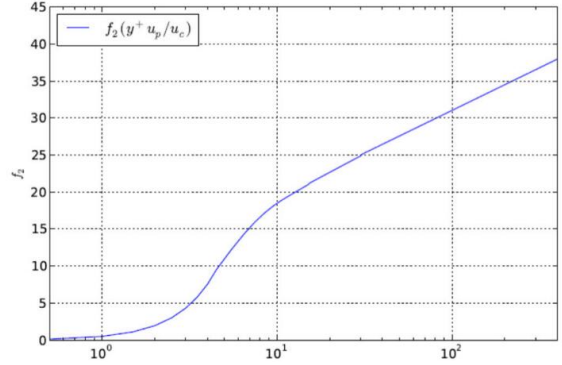


Figure 3.5: $f_2(y^+ u_p / u_c)$

This single consistent law of the wall is based on a unified non-equilibrium wall function that accounts for continuous blending between viscous sub-layer and logarithmic layer, adverse and favorable pressure gradients and surface curvature in a completely automatic way [Shih et al., 1999].

3.7 Simulation setup

3.7.1 General simulation settings

Material settings

Table 3.2: Material settings

Fluid type	Gas
Molecular weight	28.996 <i>u</i>
Density	1.225 <i>kg.m</i> ³
Temperature	288.15 <i>K</i>
Viscosity model	Newtonian
Dynamic viscosity	1.7894 <i>e</i> ⁻⁵ <i>Pa.s</i>

Simulation settings

Table 3.3: General model settings

Thermal model	Isothermal
Turbulence model 1	Large eddy simulation (LES)
Subgrid scale turbulence model	Wall adapting local eddy (WALE)
Turbulence model 2	Detached eddy simulation (DES)
Subgrid scale turbulence model	Spalart-Allmaras (SA)

Velocity – The Shell Eco-marathon requires vehicles to complete 10 laps (16117*m*) of the track in a maximum time of 39 minutes, this requires a minimum average speed of 6.888*m/s* (24.795*km/hr*). To achieve this, it was decided that a much higher speed should be used, all simulations are conducted at a straightforward velocity (c_x) of 16.667*m/s* (60*km/hr*).

Rolling road velocity – For simulations involving a moving ground plane, the velocity of the plane is the same as the straightforward velocity (c_x), 16.667*m/s*.

Yawed flow velocity – For simulations involving yawed flow, an inlet velocity is introduced from a lateral side wall, two yawed flow angels are simulated in this paper, 5° and 10°. A lateral flow inlet (c_z) of 1.438*m/s* is required for 5° yaw and 2.939*m/s* for 10° yaw.

Rotating wheel angular velocity – All simulations involving rotating wheels have wheels rotate at the same angular velocity as the speed for the vehicle is the same for all simulations. The angular velocity is calculated using $c = \omega \times r$ where ω is the angular velocity, c is the straightforward velocity and r is the wheel radius measured off the geometry. The angular velocity law in XFLOW works in degrees per second which results in an input for angular velocity (ω) as 3384.38°/s for a velocity of 16.667*m/s*.

3.7.2 XFLOW simulation setup

XFLOW solver settings

Table 3.4: XFLOW solver settings

XFLOW settings		
Flow model		Lattice Boltzmann
Inlet		Velocity
Outlet		Velocity
Wall model	Lateral boundaries	Periodic boundaries
	Ground wall	Enhanced wall-function
Domain generation		Automatic octree-like grid
Resolution scheme		Wall adaptive

XFLOW temporal discretisation

XFLOW automatically estimates the time step that will remain constant during the simulation. This is calculated by taking into account the initial maximum velocity and pressure gradient of the domain, the minimum cell size and the value of the Courant number given by the user. The Courant number is the main control over the time step, larger time steps lead to faster computation, however a smaller number results in a more stable solution but requires more computation time. The time step corresponds to the biggest resolution of the lattice, other resolution levels are automatically created using spatial and temporal resolutions twice smaller than the previous level, forming the octree structure. The Courant number by default it is set to 1 as it is the stability limit, the stability parameter (Figure 3.6) must satisfy the Courant-Friedrichs-Lewy (CFL) condition, and thus its value must be less than 1. If it reaches 1, it means that somewhere in the domain CFL is not being satisfied, the stability of the simulation is thus not ensured. A stability parameter of less than 1 means the stability of the numerical scheme is ensured and the solution should therefore be consistent. If it is very close to 0, the Courant number can be increased to save computation time. XFLOW recommends a stability parameter between 0.1 and 0.3.

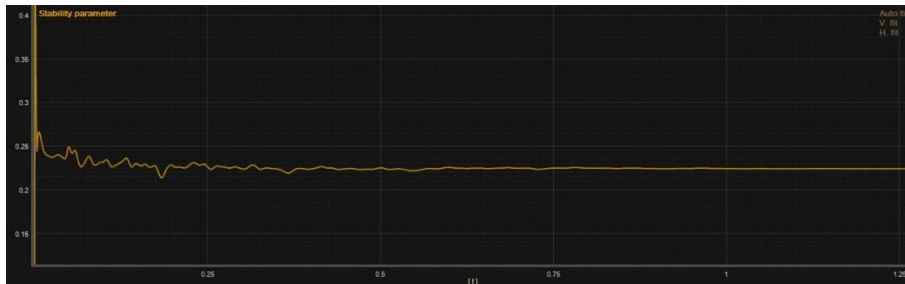


Figure 3.6: Stability parameter

Stability can usually be determined within a few minutes of running the simulation, XFLOW will warn the user that the time step is too big and stability will not be ensured. The Courant number is then decreased and the simulation is re-run until stability is achieved. Due to this unsteady nature of the simulations, output values fluctuate with time. Averaging the data is necessary for getting a single value for each case. XFLOW provides different refinement algorithms to refine the solution at areas where greater detail is required, it reduces the overall number of elements, the amount of memory and the computation time necessary. Adaptive refinement refines regions close to geometries and adapts dynamically to moving geometries following their motion. Furthermore, it can dynamically refine the wake area and the number of elements in the domain will vary in time due to the refinement.

Resolved scale resolution – Spatial resolution at the far field, i.e. the resolution of the largest level of the lattice. The smaller it is, the finer the spatial discretisation of the domain and thus the more accurate. However, the simulation time will be large as more elements must be computed.

Target resolved scale resolution – Starting at the far field scale(resolved scale), XFLOW progressively reduces the resolution size by a factor of 2 to approach the closer resolution to the Target resolved scale. Due to the lattice structure, each level of refinement is half size than the upper one. Hence, the target resolved scale is required to be: $x/(2^n)$, where x is the resolved scale and n a positive integer. If the user-defined target resolved scale do not satisfy this rule, XFLOW automatically replaces it for the closest superior number.

Wake refinement threshold – If the refinement algorithm is set to adaptive refinement, the wake is dynamically refined at the given wake resolution. The wake refinement criteria is based on the level of vorticity, regions of high vorticity are characterised as wake regions ,the particle resolution is then automatically adapted in areas of high turbulence, while treating less active regions with fewer particles.

Rule:

$$Resolved\ scale \geq Wake\ resolution \geq Target\ resolved\ scale\ (Shape)$$

3.7.3 FLUENT simulation setup

Fluent solver settings

Table 3.5: FLUENT solver settings

FLUENT settings		
Flow model		Reynolds averaged Navier-Stokes
Inlet		Velocity
Outlet		Pressure
Wall model	Lateral boundaries	Symmetry
	Ground wall	Non slip
Domain generation		Tetrahedral mesh
Resolution scheme		Refine at wall

Fluent temporal discretisation

Due to the nature of the turbulence model the simulation is transient, therefore the simulation results will fluctuate and not converge. Similarly like XFLOW, the FLUENT simulation is let to run for as long as possible so that results are as close to the correct result as possible. The FLUENT simulation is set to run for 1000 iterations before the results acquisition, averaged over 1000 iterations.

3.8 Flow visualisation

To analyse the results of the numerical calculations, flow visualisation techniques are required. Humans are capable of comprehending information much greater when it is presented visually rather than numerically. By using the computer not only for processing the numerical data, but also for visualising the data in an understandable way. There are a number of visual representations that are a standard in visualisation mappings that are used in this work including cut plots of pressure and vector fields, stream lines and iso surfaces. The representations of velocity and pressure are colour-mapped between specific ranges to best view flow visualisation techniques. The ranges for visual representations are set as shown in Figures 3.7 and 3.8 below unless otherwise stated.

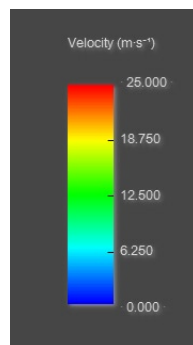


Figure 3.7: Velocity range

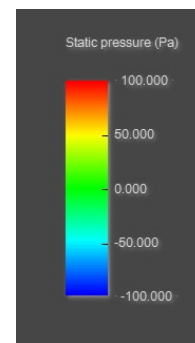


Figure 3.8: Pressure range

Chapter 4

Initial vehicle concepts

4.1 CFD validation

4.1.1 Introduction

The model chosen for simplified testing and comparison is the Ahmed body, it consists of a very simplified bluff-body which is used as a benchmark in vehicle aerodynamics [Ahmed et al., 1984]. It has been used in several experiments [Lienhart et al., 2002] [Gilliéron and Chometon, 1999] [Howard and Pourquie, 2002] [Strachan et al., 2007] [Fares, 2006] and is described as slant back, having a well defined separation line and is characterised as a low drag shape. The shape of this body is free from wheels and accessories but it still preserves the primary flow behavior of a road vehicle.

4.1.2 Geometry development

The body dimensions (Figure 4.1) of the Ahmed body were taken from the experimental work of Ahmed [Ahmed et al., 1984] and has a length $L = 1044$ mm, which is approximately a third the maximum length of a SEM urban concept vehicle. The body is suspended $0.048L$ from the floor of the wind tunnel.

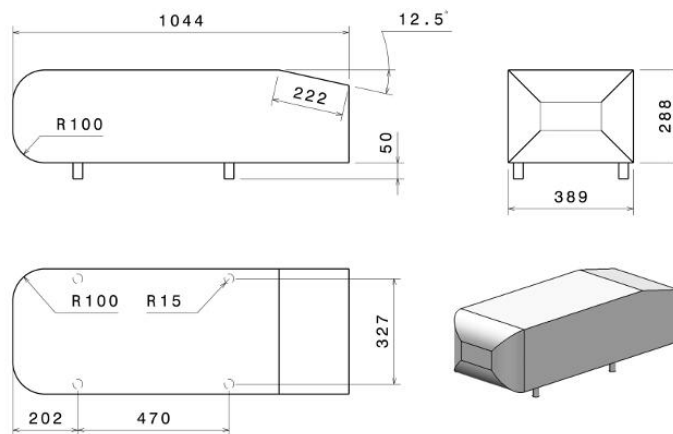


Figure 4.1: Ahmed dimensions

4.1.3 Simulation setup

Global environment setup

The virtual wind tunnel domain dimensions were taken from the work of Ahmed [Ahmed et al., 1984], it has length of $10L$ in the stream-wise direction (x), $2L$ in the span-wise (z) and $1.5L$ in the stream-normal or vertical (y). The inlet flow section is placed $2.4L$ upstream of the model front while the outlet flow section is placed $6.6L$ downstream from the model rear end.

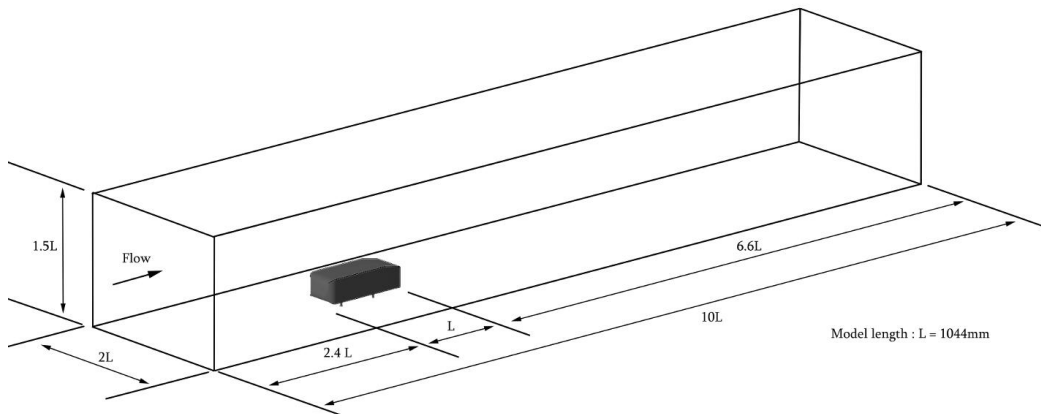


Figure 4.2: Computational domain - Ahmed body

Domain refinement setup

Table 4.1: Ahmed domain refinement setup

Resolved scale	0.04m
Wake resolution	0.01m
Shapes refinement	Ahmed body 0.01m

4.1.4 Results and Discussion

Figures 4.3 and 4.4 show how the lattice structure changes from the initial to the final step due to the wake, when using using the near wall and adaptive wake refinement.

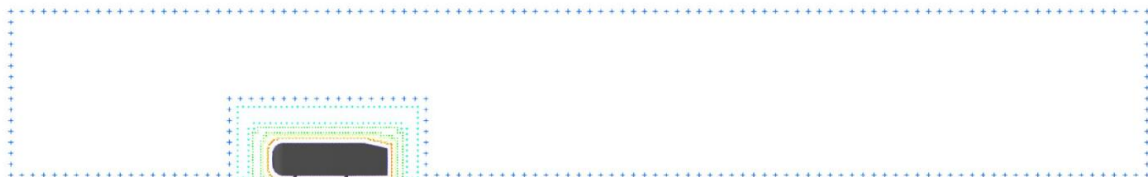


Figure 4.3: Ahmed initial refinement

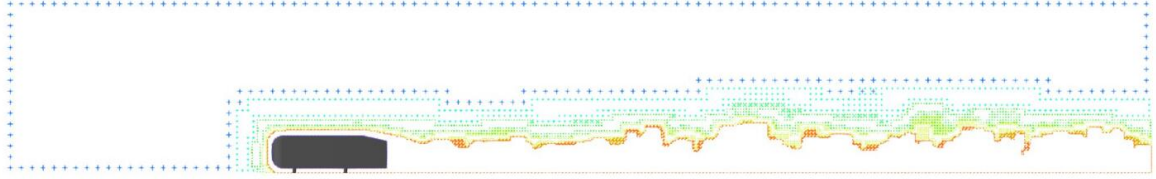


Figure 4.4: Ahmed final refinement

Table 4.2: Ahmed results

Case	Initial Elements	Final elements	C_D	C_L
Groundless	462053	1971578	0.198	0.271
Stationary road	462053	2008727	0.269	0.120
Rolling road	462053	1639859	0.279	0.066

The groundless simulation showed a drag coefficient greatly lower than the simulations with a road simulated, however it showed a greater lift coefficient. Comparing the wake structure refinement for the stationary (Figure 4.5) and rolling road (Figure 4.6) configurations, in the stationary road simulation the wake develops and is kept in the computational domain due to the friction caused by the road surface. This causes the adaptive wake refinement to refine a greater area of the computational domain than it would in comparison to a groundless or rolling road simulation. Thus the stationary road simulation is more computationally expensive, this can be seen by comparing the final number of elements between the different cases. The movement of the ground provides a more realistic simulation and confirms that drag is increased due to the rolling road. The use of the rolling road not only provides a more realistic simulation but is shown to be computationally less expensive when compared to a stationary road simulation.

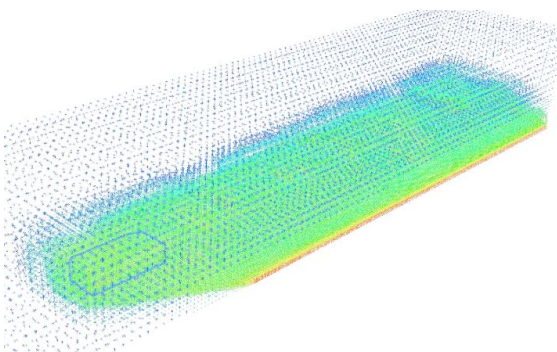


Figure 4.5: Ahmed refinement - stationary road

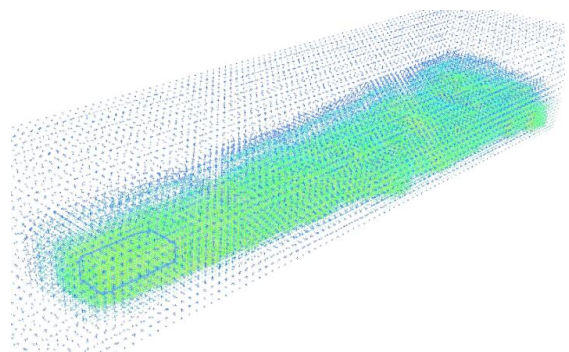


Figure 4.6: Ahmed refinement - rolling road

4.2 Low-drag concept

4.2.1 Introduction

A basic aerodynamic vehicle shape was developed in CATIA V6 in order to allow the industrial designer to visualise how different shapes affect aerodynamics. The basic vehicle model can be described as a low drag, bluff body that tapers towards the rear, resembles a road vehicle more than that of the Ahmed shape and that fits within the SEM constraints. Other factors that influenced the shape are driver position, luggage space and provision for electrical components. Further analysis includes a vehicle model that incorporates basic wheel arches in order to compare wheel geometry and rotation effects on the aerodynamic coefficients. The wheel base and track widths were set at the beginning of the project to their minimum allowable, giving the vehicle the smallest projected area possible as well as allowing it to taper towards the rear.

4.2.2 Geometry development

Initial design

Using basic sketches that can be easily manipulated to alter the geometry of the vehicle, multiple iterations of the basic shape are used to determine the best low drag shape based on the dimensional constraints of the SEM competition. Maximum and minimum limiting planes (Figures 4.8, 4.9) are used to keep the vehicle within competition specification.

The vehicle body is broken up into surface sections (Figure 4.7) which can be manipulated independently, each section consists of two curved sketches near the front and the rear connected as a multi-section surface using a curved spline that runs along the vehicle length (Figures 4.10, 4.11). The initial shape is planarly cut at the front and the rear of the vehicle shape.

The body surfaces are broken up as follows:

1. Floor
2. Bonnet/separation line
3. Sides
4. Windscreen/roof-line
5. Window sides
6. Front cut
7. Rear cut

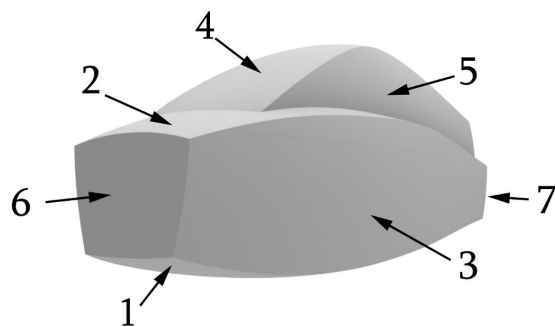


Figure 4.7: Low-drag concept surfaces

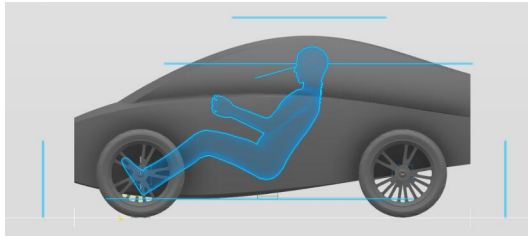


Figure 4.8: Side view of limiting planes

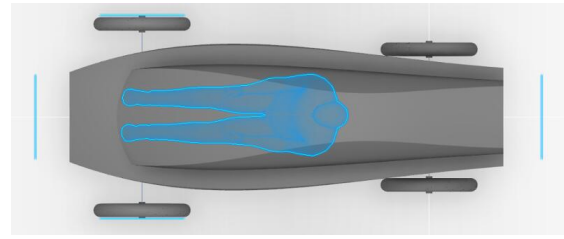


Figure 4.9: Top view of limiting planes

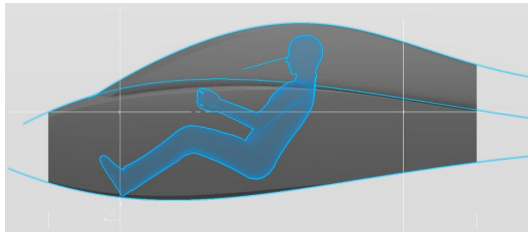


Figure 4.10: Side view of splines

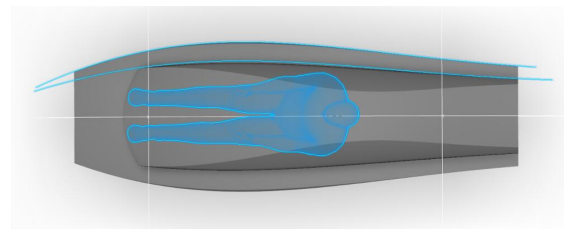


Figure 4.11: Top view of splines

Filleted design

Fillets are placed at all sharp extremities of the vehicle apart from the rear surface to determine how the rounding would affect the drag, lift and sidewind sensitivity in both straightforward and yawed flow conditions (Figure 4.12).

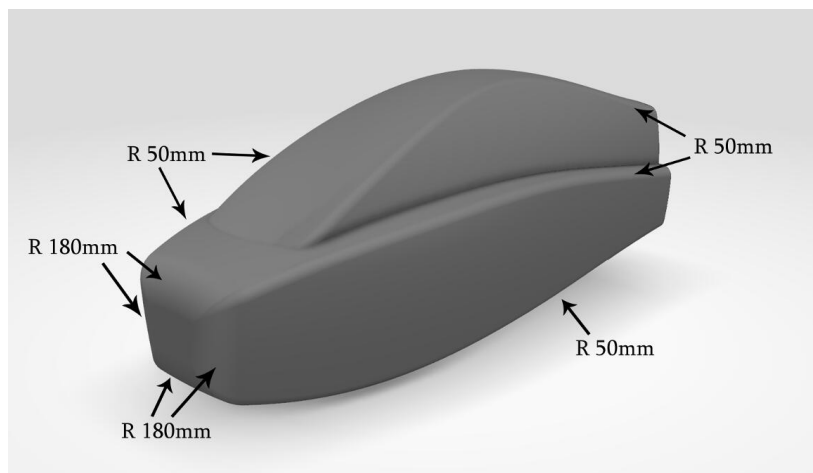


Figure 4.12: Low-drag concept filleted

Wheel-arch design

Simple wheel-arch extensions are placed over the wheels at their initial positions with provision for suspension travel and for wheel turning during steering (Figure 4.13). It is specified in the SEM rules that the wheels must be covered with arches rigidly attached to the main body of the vehicle.

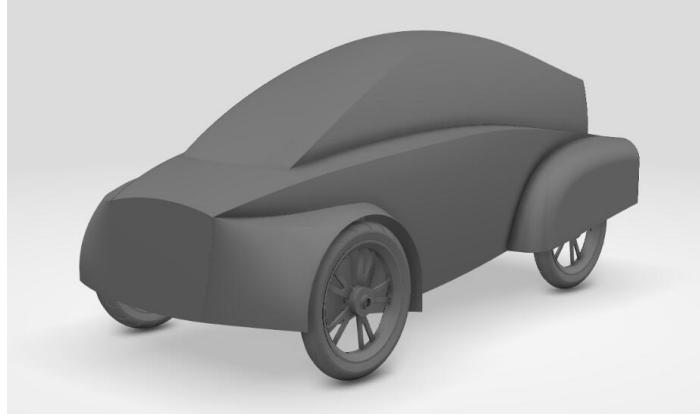


Figure 4.13: Low-drag concept with wheel-arches

Simple wheel geometry

A simple wheel and tyre geometry was modeled from overall wheel dimensions for use in simulation as a base-line test (Figure 4.14). This simple wheel provides low computation simulation for the comparison between rotating and non rotating wheels.

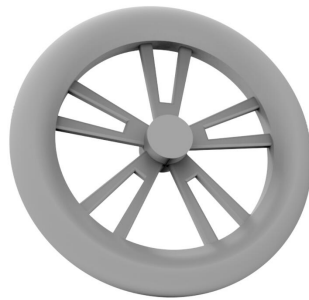


Figure 4.14: Simple wheel

Detailed wheel geometry

The detail wheel geometry was reverse engineered from a 3D scan of the actual wheel and tyre that is to be used on the final manufactured vehicle (Figures 4.15 to 4.18). This provides the exact detailed wheel geometry for use in simulations, including a model that incorporates tyre tread.



Figure 4.15: 3D scan of wheel



Figure 4.16: Wheel without tread

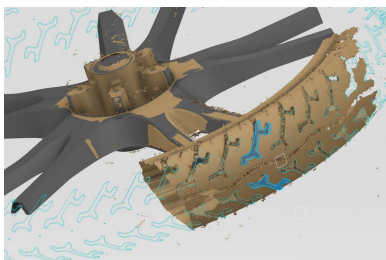


Figure 4.17: Tread development



Figure 4.18: Wheel with tread

4.2.3 CFD simulation setup

4.2.4 Global environment setup

The dimensions for the virtual wind tunnel are similar to that of the Ahmed simulations, where each length is related to the vehicle length. The wind tunnel dimensions ensured no interference from sidewalls or the inlet, as well as having enough room for a large amount of wake to develop. The simulations involving yawed flow have a larger virtual wind tunnel on the leeward side of the vehicle to account for the wake produced due to the yawed flow.

Straightforward flow

The virtual wind tunnel domain has length of $7L$ in the stream-wise direction (x), $2L$ in the span-wise (z) and $1.5L$ in the vertical (y), where L is the length of the vehicle body. The inlet flow section is located $2L$ upstream of the model front while the outlet flow section is located $4L$ downstream from the model rear end.

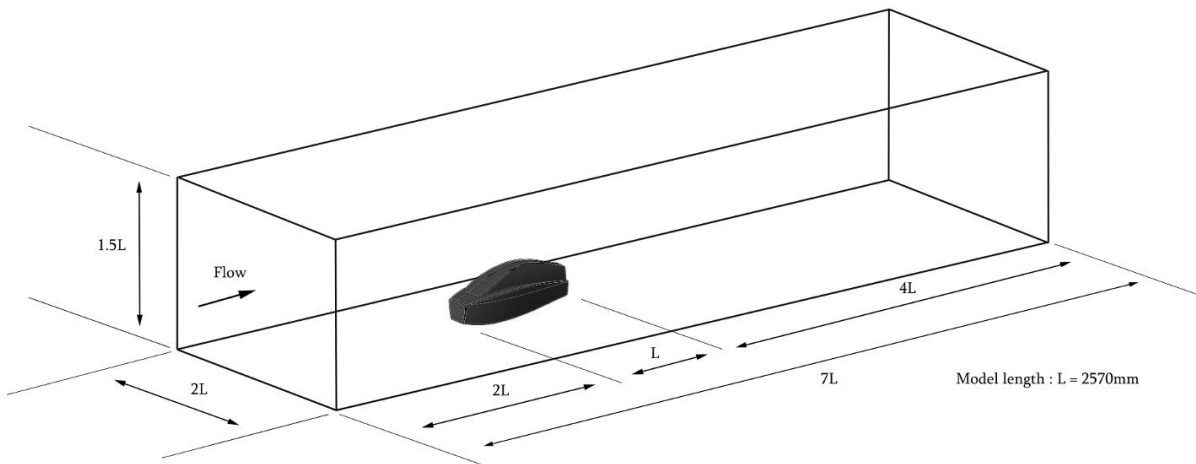


Figure 4.19: Computational domain - Low-drag concept with straightforward flow

Yawed flow

The virtual wind tunnel domain has length of $7L$ in the stream-wise direction (x), $2L$ in the span-wise (z) and $1.5L$ in the vertical (y), where L is the length of the vehicle body. The inlet flow section is located $2L$ upstream of the model front while the outlet flow section is located $4L$ downstream from the model rear end. The vehicle is offset $0.25L$ towards the span-wise direction (z) to allow for side-wake development.

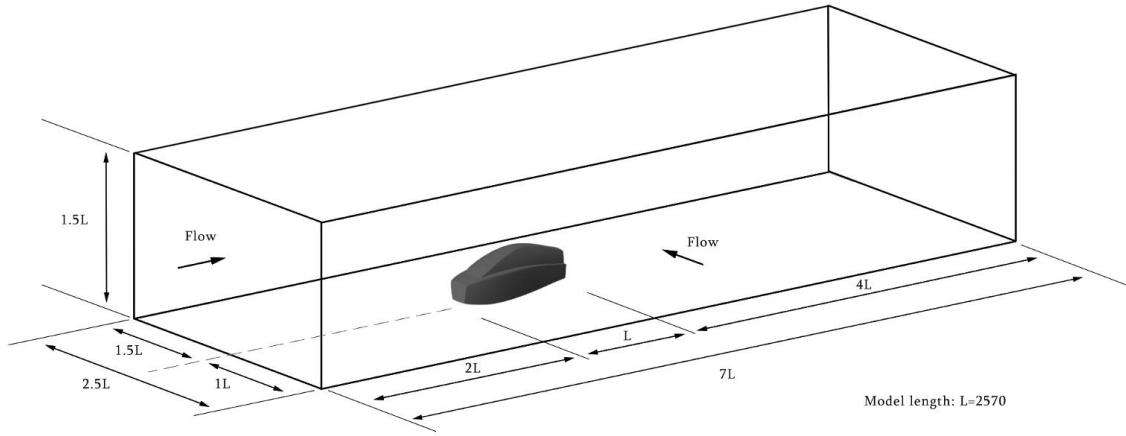


Figure 4.20: Computational domain - Low-drag concept with yawed flow

4.2.5 Domain refinement setup

Table 4.3: Low-drag shape domain refinement setup

Resolved scale		1m
Wake resolution		0.015625m
Shapes refinement	Low-drag shape	0.015625m
	Wheel	0.015625m

4.2.6 Results and Discussion

Comparison between initial and rounded model

Table 4.4: Low-drag concept results

Case	Initial elements	Final elements	C_D	C_L
Simple	409608	3719278	0.066	-0.214
Simple 5°yaw	414016	4646460	0.119	-0.224
Simple 10°yaw	414016	5630738	0.112	-0.303
Rounded	409836	4051495	0.066	-0.185
Rounded 5°yaw	414077	4164075	0.091	-0.196
Rounded 10°yaw	414077	5185135	0.149	-0.218

The outcomes of this comparison showed that rounding the edges of a simple vehicle body had no effect on the drag and only a slight decrease in downforce when under normal flow conditions (Figures 4.21 and 4.22). However when comparing the models under yawed flow conditions it was found that the rounded edges provided a decrease in drag while lowering the downforce (Figures 4.23 to 4.25).

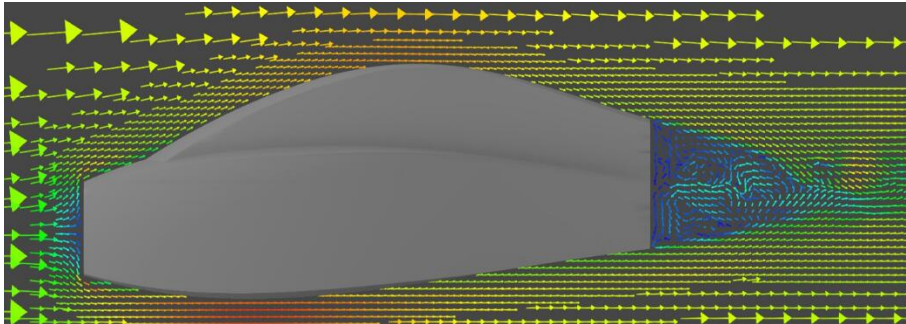


Figure 4.21: Simple initial concept side view velocity vectors

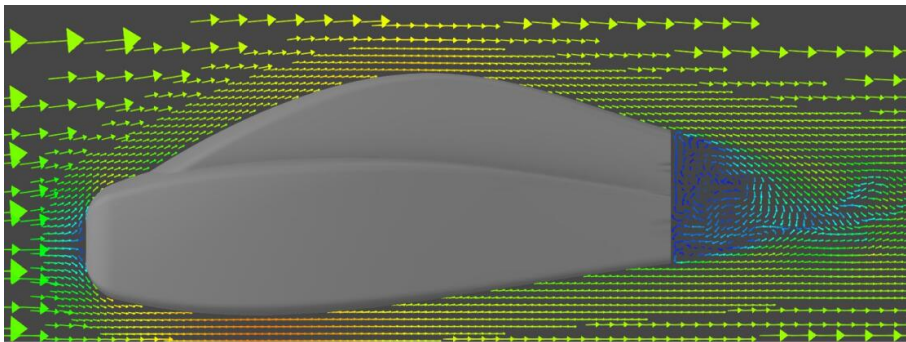


Figure 4.22: Rounded initial concept side view velocity vectors

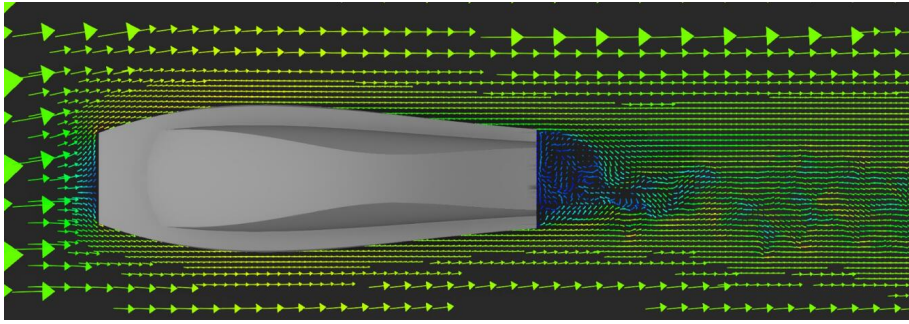


Figure 4.23: Rounded initial concept side view velocity vector cut plot

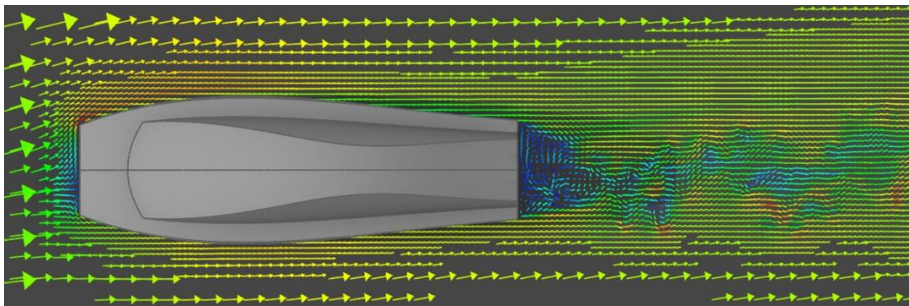


Figure 4.24: Rounded initial concept 10 yaw velocity vector cut plot

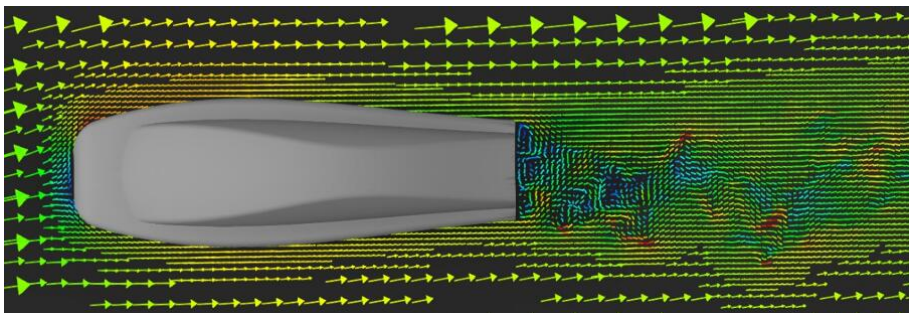


Figure 4.25: Rounded initial concept 10 yaw top velocity vector cut plot

Comparison between wheel geometries on wheel-arch model

Table 4.5: Low-drag concept with arches

Case	Initial elements	Final elements	C_D	C_L
Stationary simplified wheel	516082	7923902	0.449	-0.015
Rotating simplified wheel	522136	7477889	0.401	0.007
Rotating detailed wheel	522170	7498677	0.425	0.008
Rotating wheel with tread	522171	7372749	0.424	0.033
Rotating wheel with tread, 5°yaw	523534	7939684	0.438	0.099
Rotating wheel with tread, 10°yaw	523534	8694774	0.443	0.194

Comparing the results between the stationary simplified wheel to the rotating simplified wheel, the rotating wheel showed the ability to reduce drag and downforce in this scenario. A larger wake region can be seen inside and behind the front wheel arch of the stationary wheel (Figure 4.26) when compared to the rotating wheel (Figure 4.27). This is true to the works of Wäschle [2007] and Humnic and Chiru [2006].

When comparing the rear wheel vector cut plots (Figures 4.28 and 4.29) the same can be seen, the stationary wheel has slower moving air past it than the rotating wheel. The wake behind the rear wheel arch appears more attached with rotating wheels, whereas behind the stationary rear wheels it appears to be separating. The combination of the rotating wheels assisting in keeping the fluid moving past and keeping the wake attached had an effect of both drag and lift parameters.

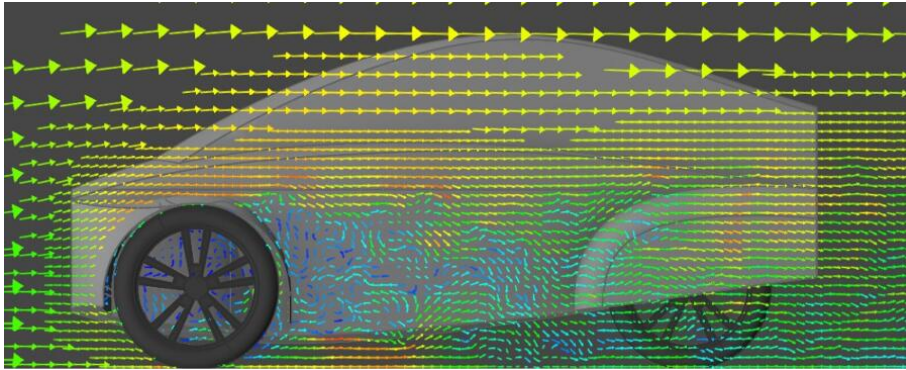


Figure 4.26: Initial concept stationary simple wheel vector cut plot

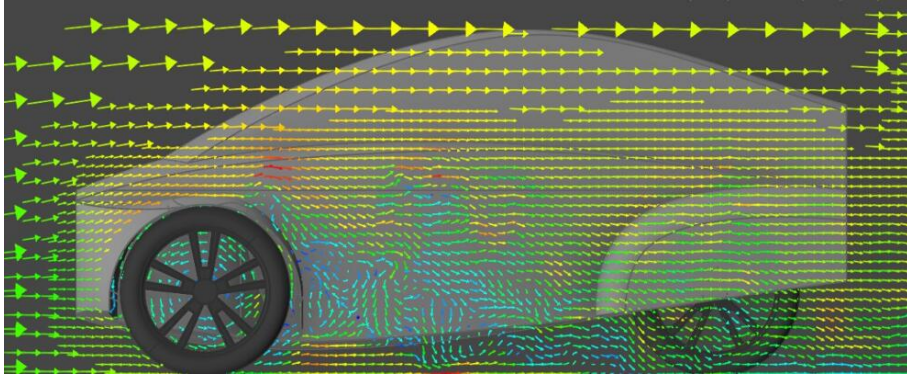


Figure 4.27: Initial concept rotating simple wheel vector cut plot

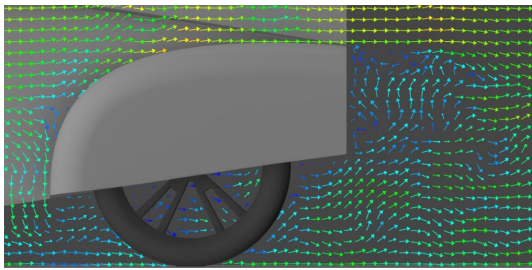


Figure 4.28: Initial concept stationary simple rear wheel vector cut plot

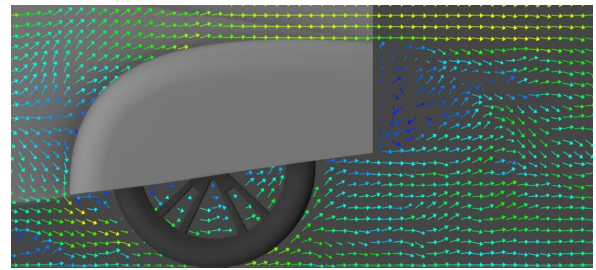


Figure 4.29: Initial concept rotating simple wheel vector cut plot

A detailed wheel geometry with rotation shows an increased drag but little effect on the lift. The more complex shape of the wheel increased wake behind the front wheel arch (Figure 4.30) when compared to the simple geometry (Figure 4.27) and especially in the case of the detailed geometry with tyre tread (Figure 4.31). The wheel with tread did not affect the drag greatly but gave an increase in lift. This shows that detail wheel geometries give significantly different results as in the work of Lounsberry et al. [2009].

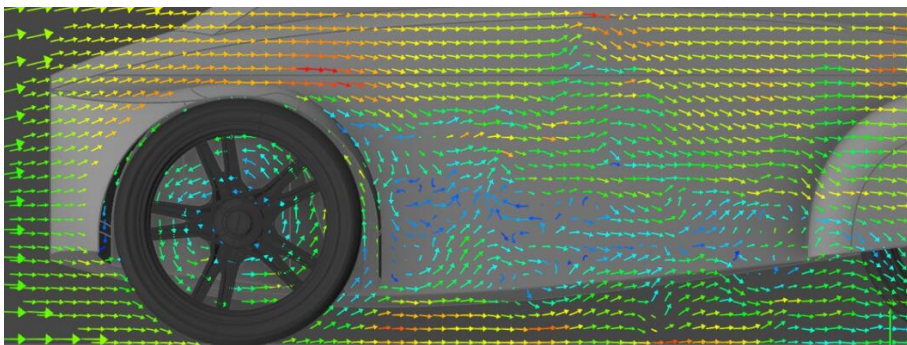


Figure 4.30: Initial concept rotating detail wheel vector cut plot

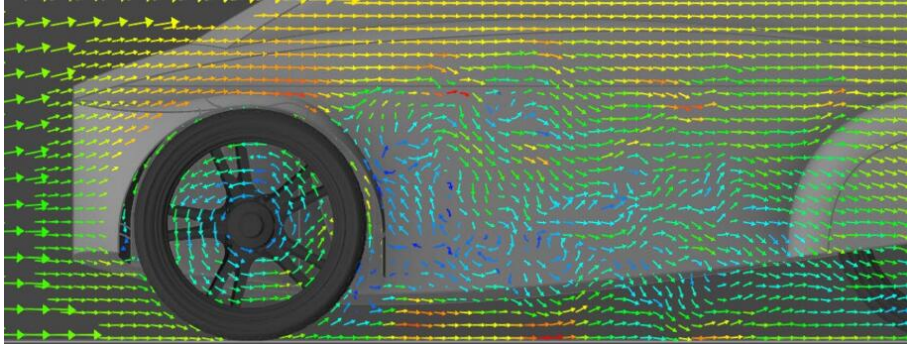


Figure 4.31: Initial concept rotating detail wheel with tread vector cut plot

Applying a yawed flow onto the model with detailed rotating wheel with tread shows an increase in both drag and lift, with a large increase in lift for a greater yawed flow. When viewing a cut plot view from the top at wheel centre; a much larger wake is seen to form behind the leeward side of the front wheel arch and behind the rear wheel on the windward side of the yawed flow simulation (Figure 4.32) when compared to the straightforward flow (Figure 4.33).

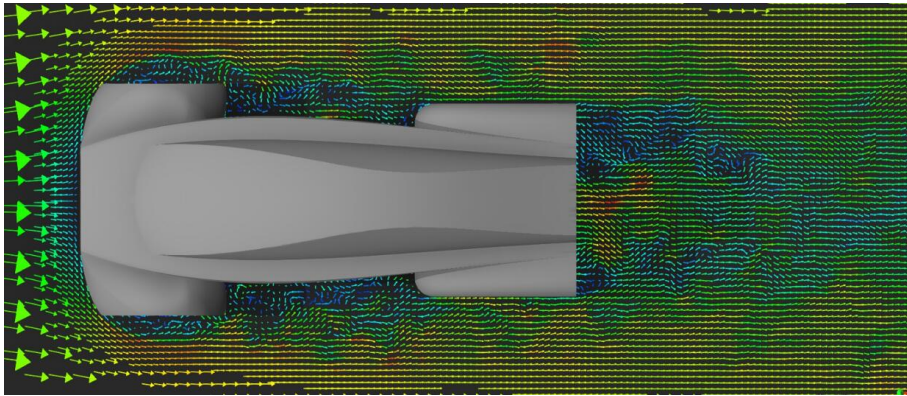


Figure 4.32: Initial concept rotating detail wheel with tread vector cut plot

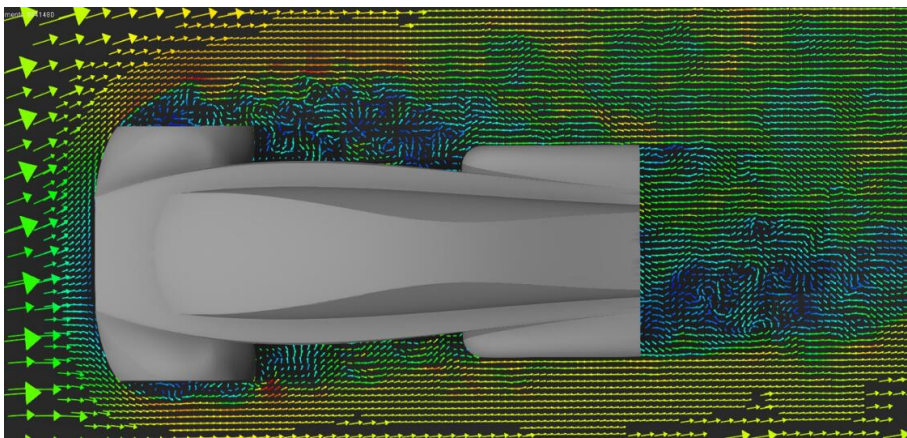


Figure 4.33: Initial concept rotating detail wheel with tread and yaw vector cut plot

4.3 Preliminary vehicle concepts

4.3.1 Introduction

The final design is required to be as aerodynamic as possible, with the addition of having good aesthetic design and features. Based on the constraints, three novel concept designs were developed with a masters student of industrial design, Adriaan Broodryk, combining ergonomics, design and aerodynamic intent.

It was shown by Wäschle [2007], Humnic and Chiru [2006] and Lounsberry et al. [2009] that rotating and detailed geometry wheels provide a significant change in the simulation results, from this and results found in sections 4.1 and 4.2, it was decided that detailed rotating wheels with tread should be used in further simulations. This section intends to show areas of the designs that have positive or negative influences on the aerodynamics of the vehicle body using the same visualisation techniques as Section 4.2, furthermore it will give a good estimate on the drag of the final vehicle and which areas could be optimised and additional modifications to be added. Concept design simulations included the effects of rolling road, rotating wheels with detailed geometry as well as the comparison between straightforward and yawed flow. Due to the low speed at which the vehicle travels, it was decided to test the concept designs with a yaw angle of 10° only to show the effects of large sidewind conditions. The concept designs need to have a certain amount of downforce in their basic shapes in order to keep an overall downforce when combined with rotating wheels and especially under yawed flow conditions.

4.3.2 Global environment setup

Straightforward flow

The virtual wind tunnel domain has length of $8L$ in the stream-wise direction (x), $2L$ in the span-wise (z) and $1.5L$ in the vertical (y), where L is the length of the vehicle body. The inlet flow section is located $1.5L$ upstream of the model front while the outlet flow section is located $5.5L$ downstream from the model rear end.

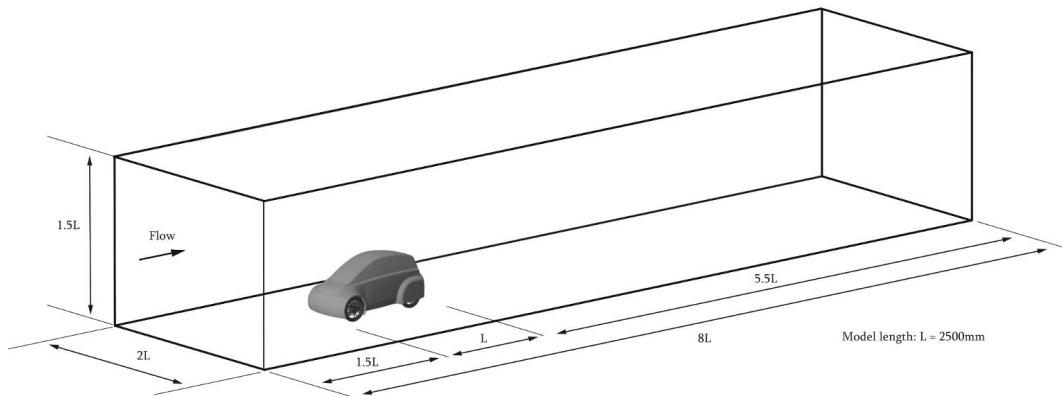


Figure 4.34: Computational domain - Concept model with straightforward flow

Yawed flow

The virtual wind tunnel domain used for yawed flow conditions has length of $8L$ in the stream-wise direction (x), $2.5L$ in the span-wise (z) and $1.5L$ in the vertical (y), where L is the length of the vehicle body. The inlet flow section is located $1.5L$ upstream of the model front while the outlet flow section is located $5.5L$ downstream from the model rear end. The vehicle is offset $0.25L$ towards the span-wise direction (z) to allow for side-wake development.

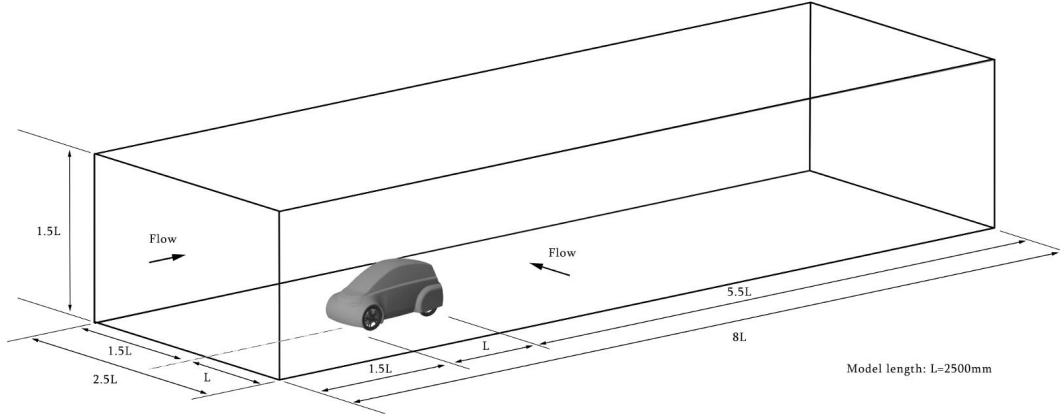


Figure 4.35: Computational domain - Concept model with yawed flow

Simulation parameters

4.3.3 Domain refinement setup

Table 4.6: Final design domain refinement setup

Resolved scale		1m
Wake resolution		0.015625m
Shapes refinement	Vehicle body	0.015625m
	Wheel	0.015625m

Geometry development

The development of the vehicle concepts was done in conjunction with an industrial design masters student. His initial role was to provide concept sketches which translated into novel concept designs in CATIA V6, of which 3 concept designs are simulated. The vehicle concepts fall within the SEM constraints, are generally similar in size and feature different design styles. The wheel base and track width are set the same for all concepts, this provided a similar frame on which to develop the shapes and reduced simulation setup time. The vehicles were developed mainly around the mechanical and electrical components, but also included the driver position, visibility requirement, ensuring the ease of entering and exiting the vehicle, and provision for the required

luggage space. According to the SEM rules, all mechanical components including the suspension and wheels of the vehicle and the driver must be covered with a rigid shell. The roof must surround the drivers head such that the helmet is 50mm below the roll bar and the covers for the suspension and wheels must be covered when viewed from above and up to the axle centre line when viewed from the front or the rear. The vehicle body must also not have any sharp edges or points that might be dangerous to anyone that would come into contact with the vehicle exterior. The vehicle concepts however did not take into account the provisional space for the travel of the wheels brought on by suspension and steering effects.

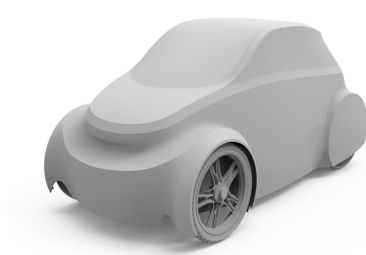


Figure 4.36: Concept 1

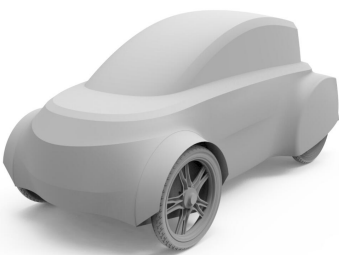


Figure 4.37: Concept 2

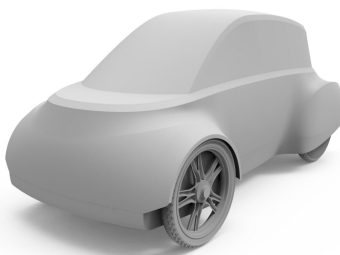


Figure 4.38: Concept 3

Chapter 5

CFD results of preliminary vehicle concepts

Table 5.1: Concept results

Case	Initial elements	Final elements	C_D	C_L	C_Z
Concept 1	495072	7166275	0.339	-0.017	–
Concept 1 10°yaw	496953	9256739	0.388	0.233	-0.399
Concept 2	497465	7724419	0.411	0.261	–
Concept 2 10°yaw	496703	9013428	0.434	0.341	-0.279
Concept 3	503874	7836108	0.324	0.399	–
Concept 3 10°yaw	503740	9214638	0.410	0.437	-0.278

From the results in table 5.1 it can be seen that concept 1 and 3 offer the lowest drag, while concept 1 has the most desirable lift coefficient. However, all concepts incur a large increase in lift due to the crosswind effects, where concept 3 is the least affected although it starts with a less desirable lift coefficient.

Looking at the isosurfaces of vorticity, coloured by velocity as shown in Figures 5.1 to 5.3, for straightforward flow, a large portion of the turbulent wake is seen to arise from the front wheel arches due to their location away from the body and the rotating wheel. This wake is seen to be less in concept 1, due to a more closed off wheel arch, while concept 2 and 3 showed more wake due to the more open wheel arches near the floor of the vehicle. Separation was also noted on concepts 1 and 3 on the A-pillar section on the vehicle, this is due to the amount of curvature on the A-pillar going from the windscreen to the side windows. Ample curvature in the A-pillar section can be seen in concept 2 as it does not show and separation in this area. Separation is also seen to occur on the sharper details on the nose of concepts 1 and 2, while concept 3 has a large area of separation and re-attachment from the nose to the windscreen, this is backup up by lateral centre cut plots (Figures A1 to A3). Looking at cut plots located at the front wheel (Figures A7 to A12) another trend that developed between the simulations appeared as a low pressure zone above the front wheel arches. As the front wheels are used for steering, a small amount of downforce is require in order to

keep grip with the road while turning, this problem is likely inherent with the shape of the wheel arch and may require modification to rectify. During simulations that involved yaw, concept 1 clearly performed the worst while concepts 2 and 3 performed similarly both in results and visual representation (Figures A16 to A18).

From this, the results along with the visualisations, a better understanding of how the visualisations can be related to the results which assists in the development in the final model.

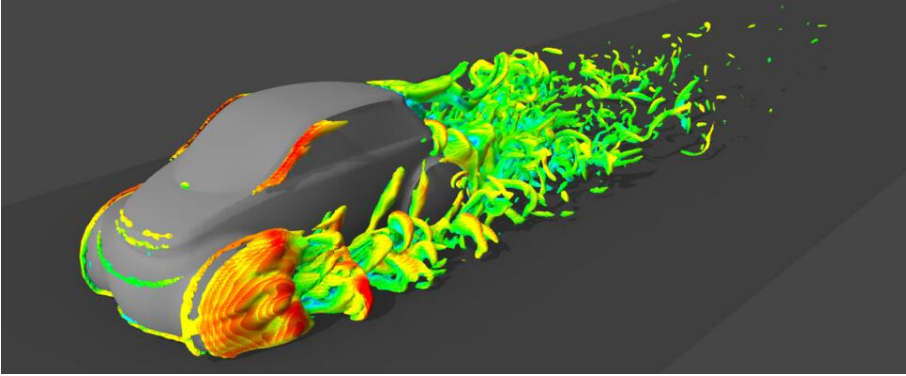


Figure 5.1: Isosurface - concept 1

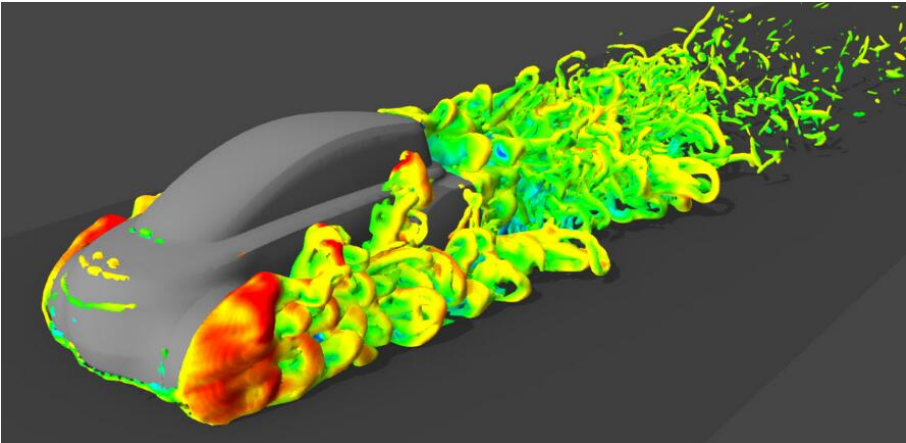


Figure 5.2: Isosurface - concept 2

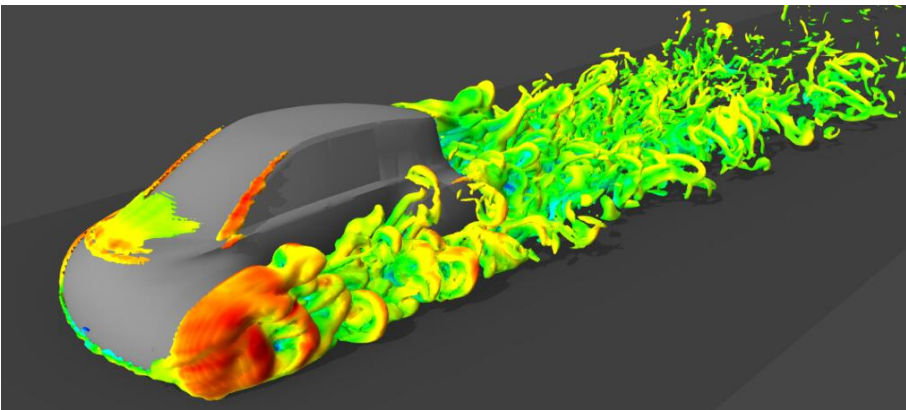


Figure 5.3: Isosurface - concept 3

Chapter 6

Result of aerodynamic development

6.1 Final design

6.1.1 Introduction

The best aerodynamic, ergonomic, stylistic and manufacturable features from the concept studies are integrated into a final design vehicle. The design of the final vehicle is based that of concept 3, which showed good characteristics in both straightforward and yawed flow, as well as being chosen as the most aesthetic by a review of engineers and designers. This concept however had the least favourable coefficient of lift (C_y).

This vehicle will be simulated with a rolling road and rotating detailed wheels with tread only, the previous simulations showed the importance of using these and how they influence the aerodynamics. It was decided to use detail wheels with tread, even though the simulations in Section 4.2 showed an effect on the lift only, as it could have greater effect when modification is made to the front wheel arch.

6.1.2 Geometry development

The geometry used in XFLOW simulations does not need any prior modification and can be exported from CATIA as is, only a few components from the interior were removed as they would not have any effect on the airflow. The vehicle shell takes into account provision for steering and suspension travel of the front wheel and suspension arms in the front wheel arch. It was decided that the wheel arches should encompass as much of the wheel as possible, in order to portray a real world road vehicle, this also increases front suspension arm protection, as well as aiding in wheel arch rigidity. The front areas were made devoid of sharp edges, this problem can be seen in final concept 1 where the sharp areas on the front caused a large wake to appear behind the front wheel in yawed flow. Other design parameters include; a tapering rear end, a curved roofline and underfloor, a smooth transition between the front and the windscreen to discourage separation and re-attachment, a well curved A-pillar to avoid separation and a sharp cut rear end to help with separation.

Two different geometries based on the same design were designed, a simple and a detailed model. The simple geometry has a simplified chassis and shell, which is more closed and does not include any detailed body geometries. The detailed model includes the detailed suspension geometries as well as headlights which are regarded as a highly important aesthetic feature that should be included in simulations. The reason two different level of detail geometries are tested is to see if a less detailed geometry would provide the same results for less computing time. Figure 6.1 shows the final detailed model from various views. Figure 6.2 shows an internal view of the chassis and suspension components for the detailed model.

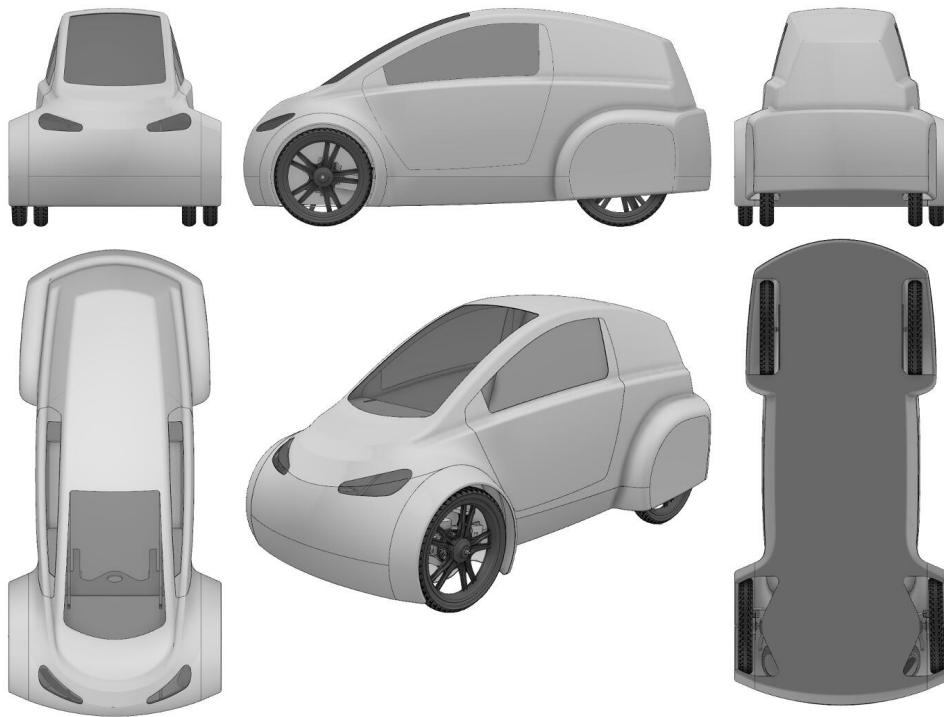


Figure 6.1: Detailed final geometry

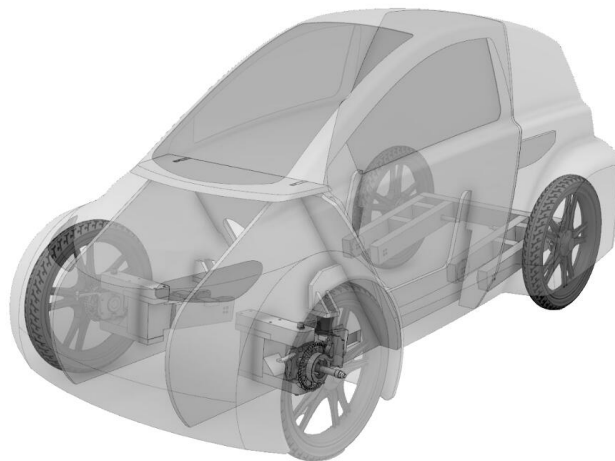


Figure 6.2: Detailed final geometry cutaway

6.1.3 Simulation settings

Table 6.1: Simulation settings

General simulation settings	
Velocity	16.667 <i>m.s</i>
Resolved scale resolution	1m
Shapes refinement resolution	0.015625m
Subgrid-scale turbulence	Wall-Adapting Local-Eddy

6.1.4 Results and discussion

Table 6.2: Final design results

Case	Initial elements	Final elements	C_D	C_L	C_Z
Final simplified	563537	8745501	0.401	0.011	–
Final simplified yaw	563179	10649654	0.473	0.344	-0.490
Final detailed	941464	9233405	0.399	-0.006	–
Final detailed yaw	941106	11097679	0.463	0.279	-0.443

Comparing results of the simplified and detailed final model, the detail geometry simulations including suspension arms did not have a great influence on the drag in both normal and yawed flows, however the other characteristics such as lift and sidewind sensitivity were seen to have different results. Although the starting elements of the detailed simulations were far greater than those of the simple simulations, the final elements for both simple and detailed were similar.

Comparing the results of the detailed final model to the concept designs results shows an increase in drag comparing to concept 3, however an improvement in the lift value can be seen which now gives a slight downforce as required. The increase in sidewind sensitivity did not come from the included suspension geometry as seen in the comparison between simple and detailed final geometry, this issue could be due to the increased projected side area from the more sloping front windscreen as well as the larger front wheel cavity for steering and suspension travel of both the wheel and suspension arms.

6.2 CFD comparison

6.2.1 Introduction

To properly justify the results of the final design and of further simulations, the final design results are compared with another CFD software namely Ansys FLUENT 14.5. This not only allows the comparison of results but also of the simulation setup between the two software, setup time and computation time are highly important factors in CFD analysis efficiency.

The material and simulation settings are set up the same as the previous simulations (Section 3.7), however due to the constrictions of FLUENT and simplified comparison, some of the parameters were not simulated, these include rolling road, rotating wheels and yawed flow. The simulation settings for XFLOW are the same as used previously for the detailed final design, however the automatic wake refinement is disabled due to FLUENT not having a dynamic mesh refinement system. Results for the FLUENT simulation were taken after 1000 iterations and averaged over 1000 iterations, due to the transient turbulence model the solution does not converge making it necessary to take the result after the solution has stabilised.

6.2.2 Geometry development

The final vehicle design geometry had to be simplified in order to simulate in Ansys FLUENT, due to it's mesh-based approach it requires the model to be 'water tight' in order to define a preferable fluid domain. This restriction requires a much simpler version of the vehicle in terms of suspension components and wheels while keeping the vehicle body geometry as accurate as possible. The exported model included simplified stationary wheels with no tread, simple inner front wheel arch with no suspension and no rear wheel compartment. Figures 6.3 and 6.4 below show the simplified vehicle body imported in both FLUENT and XFLOW.

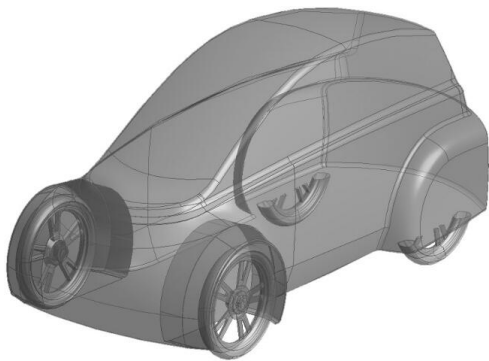


Figure 6.3: Final simplified - FLUENT

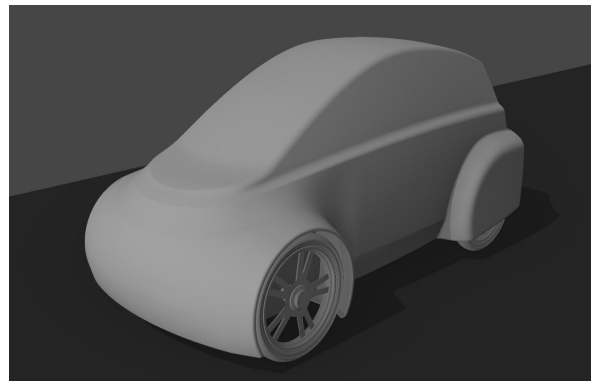


Figure 6.4: Final simplified - XFLOW

Below, a comparison of the spatial discretisation methods between the two softwares is shown. Figure 6.5 shows FLUENT’s mesh based domain and Figure 6.6 shows XFLOW’s lattice based domain.

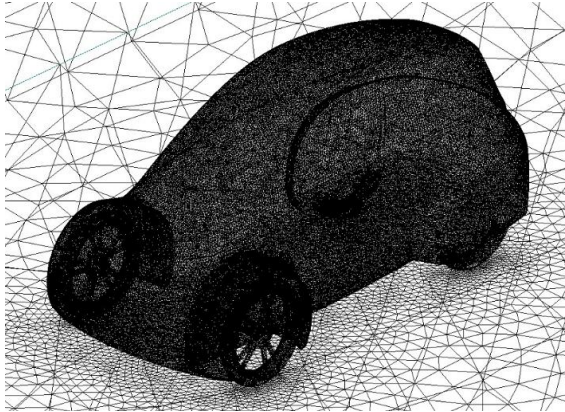


Figure 6.5: FLUENT’s mesh

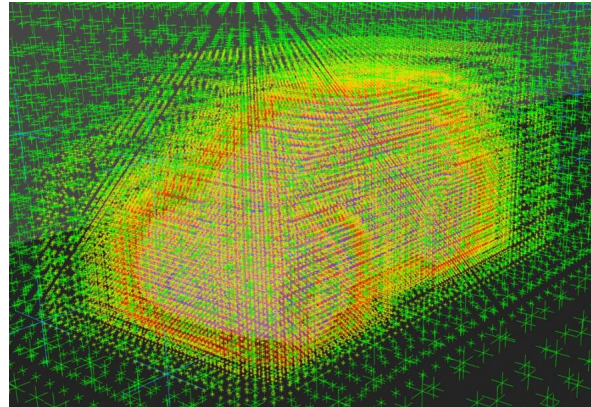


Figure 6.6: XFLOW’s lattice

6.2.3 Simulation settings

Table 6.3: Simulation settings

General simulation settings	
Velocity	16.667 <i>m.s</i>
Resolved scale resolution	1m
Shapes refinement resolution	0.015625m and 0.0078125m
Subgrid-scale turbulence	Wall-Adapting Local-Eddy Spalart-Allmaras

6.2.4 Results and discussion

The initial comparison between XFLOW and FLUENT showed some discrepancies between the values, this prompted re-simulation using a better refinement in both software as well as a comparison using a different turbulence model. The alternative turbulence model chosen was the Spalart-Allmaras as it can be found in both software and was developed to analyse aerodynamic flows in the aerospace industry. The results of the software comparison are shown in Tables 6.4 and 6.5.

Table 6.4: WALE turbulence model results

Refinement: 0.015625m		
Case	C_D	C_L
FLUENT stationary road	0.574	0.208
FLUENT rolling road	0.569	0.169
XFLOW stationary road	0.572	0.087
XFLOW rolling road	0.562	0.056
Refinement: 0.0078125m		
Case	C_D	C_L
FLUENT stationary road	0.585	0.112
FLUENT rolling road	0.555	0.054
XFLOW stationary road	0.498	0.272
XFLOW rolling road	0.494	0.267

Table 6.5: Spalart-Allmaras turbulence model results

Refinement: 0.015625		
Case	C_D	C_L
FLUENT stationary road	0.615	0.344
FLUENT rolling road	0.565	0.287
XFLOW stationary road	0.576	0.084
XFLOW rolling road	0.583	0.096
Refinement: 0.0078125		
Case	C_D	C_L
FLUENT stationary road	0.634	0.332
FLUENT rolling road	0.581	0.292
XFLOW stationary road	0.502	0.280
XFLOW rolling road	0.497	0.311

While drag values were similar in the initial refinement for the wall adapting local eddy turbulence model, XFLOW's lift value is far less than that of FLUENT. When looking at the higher refinement level results XFLOW's drag value is marginally less than that of FLUENT; however, the values for lift show an increase in lift in XFLOW and a decreased lift in Fluent. This however is not entirely the case with the Spalart-Allmaras turbulence results, drag results are similar and XFLOW does have a low lift in the initial refinement, but FLUENT's lift value does not decrease when using a higher resolution. It can be said that refinement had a greater overall effect on XFLOW's results than for FLUENT's.

The results from FLUENT show a decrease in drag and lift due to the rolling road for all simulations, XFLOW results showed similar drag for all configurations; a decrease in lift using the WALE turbulence model and a slight increase in lift using the Spalart-Allmaras turbulence model. The rolling road had a far greater effect on the lift than on the drag in all simulations with refinement levels having less than 5% for WALE and less than 10% for SA change in drag coefficient, the change in lift

between road configurations was seen to be more consistent for SA than for WALE. For the WALE turbulence model, refinement had little effect on the drag in FLUENT and showed a 12% decrease in XFLOW, however, the change in lift in XFLOW greatly outweighed ($> 200\%$) the change in FLUENT. Refining the domain increased the lift in XFLOW above the original FLUENT values, while reducing the lift in FLUENT to values similar to the original XFLOW results. This however was not the case with the SA model, it showed similar lift values in FLUENT for both refinement levels and in XFLOW for only the refined simulation results.

These results show correlation between the bluff body simulation comparison (Section 4.1) between stationary and rolling road configurations, the effect of a rolling road had negligible effect on drag and a greater than 50% reduction in lift.

Comparing the flow visualisation of FLUENT and XFLOW show some good similarity and some difference, the pressure range was automatically calculated by FLUENT and applied to XFLOW in order to compare fluid surface interaction. The surface pressure plots of initial refinement simulations using the wall adapting local eddy turbulence model (Figures 6.7 and 6.8) appear similar however the XFLOW model shows an area of high pressure at the rear edge which does not appear in the FLUENT model. After refining the simulation (Figures 6.9 and 6.10) there was no drastic change to the FLUENT result while the XFLOW result gave a low pressure region at the rear end of the vehicle where the previous simulation showed a high pressure region. The same can be seen the Spalart-Allmaras turbulence model was used (Figures 6.11 to 6.14); the rear edge of the vehicle gives similarly different results from XFLOW where it turns from a high pressure region to a low pressure one after refinement. These differences in flow characteristics near the rear of the vehicle are able to cause changes in the wake which can greatly effect the lift, as can be seen by the change in C_L values in XFLOW due to refinement.

Wall adapting local eddy (WALE) turbulence model - Refinement: 0.015625

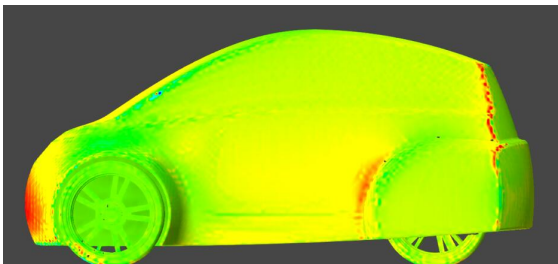


Figure 6.7: XFLOW - WALE - 0.015

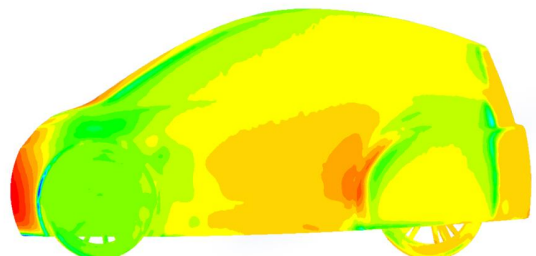


Figure 6.8: FLUENT - WALE - 0.015

Wall adapting local eddy (WALE) turbulence model - Refinement: 0.0078125

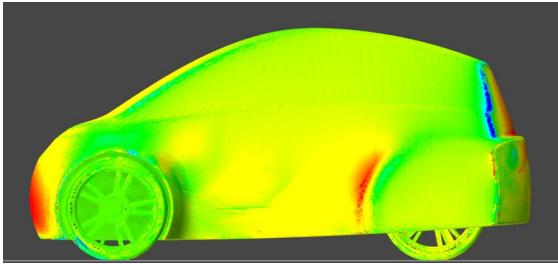


Figure 6.9: XFLOW - WALE - 0.007

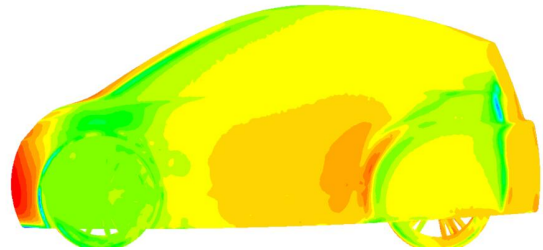


Figure 6.10: FLUENT - WALE - 0.007

Spalart-Allmaras (SA) turbulence model - refinement: 0.015625

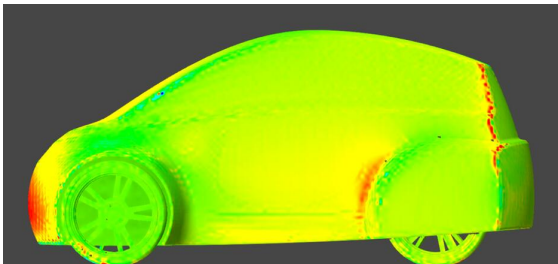


Figure 6.11: XFLOW - SA - 0.015

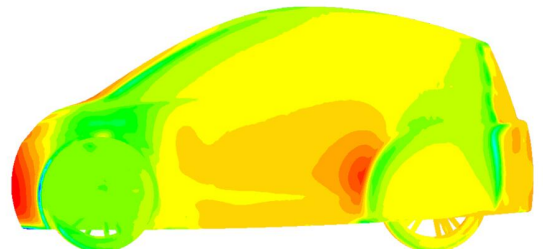


Figure 6.12: FLUENT - SA - 0.015

Spalart-Allmaras (SA) turbulence model - refinement: 0.0078125

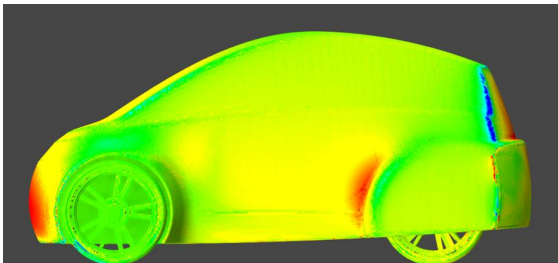


Figure 6.13: XFLOW - SA - 0.007

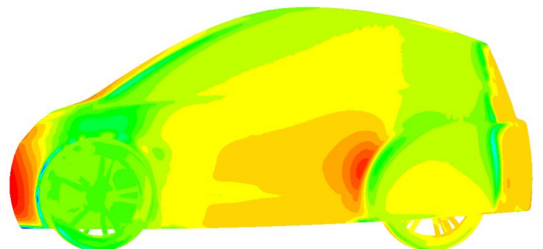


Figure 6.14: FLUENT - SA - 0.007

It can be said that refinement had a greater overall effect on XFLOW's results than for FLUENT's and that refinement does not completely correlate between the two solvers or the two turbulence models. Simulations do not completely validate between the software, although refining the XFLOW simulation gave a more similar result to FLUENT when looking at the pressure near the rear edge. Other differences that can be seen in the flow visualisations is a high pressure zone on the bottom of the front windscreen in all the FLUENT simulations only, and a high pressure zone in the centre of the rear of the vehicle in higher refinement XFLOW simulations only.

The use of rotating wheels in CFD can be easily implemented in XFLOW and offers a more realistic look at vehicle aerodynamics. The effect on drag and lift of rotating wheels in combination with a rolling road was simulated using the WALE

and SA turbulence models at the previously used refinement levels. Table 6.6 shows the results of the rotating wheel simulations.

Table 6.6: Rotating wheels comparison results

Refinement: 0.015625		
Case	C_D	C_L
WALE stationary wheels	0.562	0.056
WALE rotating wheels	0.54	0.018
SA stationary wheels	0.583	0.096
SA rotating wheels	0.541	0.024
Refinement: 0.0078125		
Case	C_D	C_L
WALE stationary wheels	0.494	0.267
WALE rotating wheels	0.476	0.334
SA stationary wheels	0.497	0.311
SA rotating wheels	0.492	0.364

The use of rotating wheels and rolling road combined in XFLOW simulations showed some (<10%) reduction in drag for all turbulence models and resolutions. The rotating wheels however had a negative effect on lift by around 100% for low resolution and an increase in lift of around 20% for higher resolution simulations.

Compared to the low-drag concept simulations (Section 4.2), the use of rotating wheels reduces drag, however, the change in lift for the low-drag concept showed better correlation with the higher resolution final results as both comparisons showed an increase in lift.

6.3 Aerodynamic modifications

6.3.1 Introduction

Modifications are done to the final vehicle model to assess the applicability of specific modifications to this vehicle. Modifications were only considered if they could be attached or adapted to the manufactured shell, after its completion. The modifications were chosen from various known vehicle modifications with the intention of lowering drag and sidewind sensitivity, as well as keeping a slight downforce under all conditions. Due to the possible underestimation of lift with the chosen resolution scheme, modifications can be used to compensate for the error. Modifications were chosen that did not drastically increase the projected frontal area of the vehicle as well as to not increase the weight of the vehicle severely. All modifications are made to the detailed final vehicle as a more detailed model would give better results especially since some modifications would interference with geometry in the detailed model. Aerodynamic appendages which adjust or are prone to changing shape due to wind whilst the vehicle is in motion, are forbidden by the rules of the SEM. Simulations were set up exactly the same as the final design simulations for both straightforward and yawed flow. These modifications allow the improvement of aerodynamic characteristics where the final design model had inherent issues. A fine resolution in CFD is vital for correct results and the main driving force behind CFD is computing power. Time based constraints limit the possible resolution level needed to obtain accurate results; however, comparing changes to a design can give a good estimate to what effect the modifications will have on the flow characteristics.

6.3.2 Geometry development

Pictures of all modifications can be seen in Appendix B. The spoiler modifications (Figures B1 and B2) are not the usual inverted wing type, but rather a tapering extension of the rear outline with the intention to reduce the wake size.

6.3.3 Simulation settings

Table 6.7: Simulation settings

General simulation settings	
Velocity	16.667 <i>m.s</i>
Resolved scale resolution	1m
Shapes refinement resolution	0.015625m
Subgrid-scale turbulence	Wall-Adapting Local-Eddy

6.3.4 Modification results and discussion

Table 6.8: Concept results

Case	Initial elements	Final elements	C_D	C_L	C_Z
Rear spoiler 1	941938	8996201	0.393	-0.022	–
Rear spoiler 1 with yaw	941580	11019788	0.459	0.344	-0.427
Rear spoiler 2	946796	8135103	0.374	0.049	–
Rear spoiler 2 with yaw	946431	11184932	0.440	0.263	-0.436
Front diffuser	941532	9295822	0.413	0.000	–
Front diffuser with yaw	941174	11469671	0.474	0.286	-0.448
Rear diffuser 1	941181	9121899	0.412	-0.116	–
Rear diffuser with yaw 1	940487	10671530	0.450	0.260	-0.411
Rear diffuser 2	940941	8958923	0.407	-0.110	–
Rear diffuser 2 with yaw	940583	10853346	0.453	0.228	-0.432
Wheel diffuser	941539	8816532	0.390	0.018	–
Wheel diffuser with yaw	941181	11288805	0.481	0.349	-0.436
Side skirt	942414	9195316	0.401	-0.034	–
Side skirt with yaw	942056	10939246	0.466	0.303	-0.464
Wheel cover	942201	8866971	0.384	0.002	–
Wheel cover with yaw	941806	11274282	0.454	0.409	-0.461
Wheel arch vent top	941448	9041113	0.393	-0.006	–
Wheel arch vent top with yaw	941185	11052240	0.462	0.277	-0.453
Wheel arch vent rear	941535	8899156	0.403	-0.036	–
Wheel arch vent rear with yaw	941177	11149935	0.477	0.324	-0.443-
Wheel arch slot	941448	9162843	0.388	0.002	–
Wheel arch slot with yaw	941090	11623951	0.470	0.300	-0.429
Front air guide 1	941013	9097868	0.395	-0.002	–
Front air guide 1 with yaw	940655	10994727	0.461	0.297	-0.437-
Front air guide 2	941136	9142791	0.403	-0.029	–
Front air guide 2 with yaw	940778	11449024	0.467	0.277	-0.448
Rear vent	941543	9153215	0.399	0.002	–
Rear vent with yaw	941185	11212901	0.475	0.322	-0.443
Side mirrors	945936	9321541	0.413	-0.022	–
Side mirrors with yaw	945480	11349188	0.471	0.268	-0.429
Rear vein	941838	9171261	0.401	-0.018	–
Rear vein with yaw	941409	11052041	0.473	0.308	-0.427

From analysing the data as well as comparing flow visualisations, the following can be said for each modification:

Rear spoiler 1 - Improved drag and downforce during normal flow and improved side wind sensitivity during yawed flow compared to the final design . A reduced wake size can be seen when comparing a cut plane of the velocity vectors between spoiler 1 and the final model (Figures 6.15 and 6.16).

Rear spoiler 2 - Good improvement on drag overall, but increases lift compared to the final design. An even greater reduction in wake size can be seen when comparing a cut plane of the velocity vectors between spoiler 2 and the final model (Figures 6.15 and 6.17).

Front diffuser - No improvement to any characteristic.

Rear diffuser 1 - Had a negative influence on drag but provided an increase in downforce in all conditions compared to the final design. A change to the shape of the wake and its size can be seen when comparing cut plane of the velocity vectors between diffuser 1 and the final model (Figures 6.18 and 6.19)

Rear diffuser 2 - Performed slightly better than rear diffuser 1 with regards to lift during a sidewind compared to the final design. A greater change to the shape of the wake and its size can be seen when comparing cut plane of the velocity vectors between diffuser 2 and the final model (Figures 6.18 and 6.20)

Wheel spoilers - Decreases drag in normal flow only, negative influence on the other characteristics

Side skirts - Increases downforce slightly in straightforward only.

Wheel cover - Improvement on drag but increased sidewind sensitivity and lift.

Wheel arch vent top - No improvement to any characteristic.

Wheel arch vent rear - Slight increase in downforce on front wheel, although does have adverse affects during yawed flow.

Wheel arch slot - Improves drag, sidewind sensitivity but has light adverse effects on the rest of the characteristics.

Front air guide 1 - Not much improvement to any characteristic.

Front air guide 2 - Slight increase in downforce.

Rear vent - No improvement to any characteristic. Side mirror - Increased drag, only slight improvements on other characteristics.

Rear vein - Only slightly increased downforce during normal flow only and slightly better sidewind sensitivity.

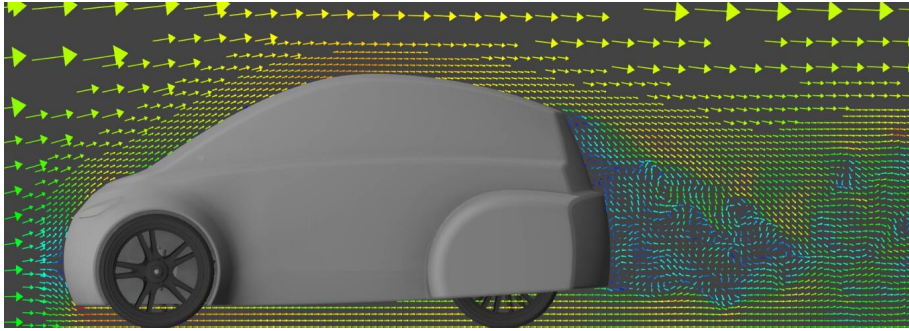


Figure 6.15: Final model - centre cut velocity vectors

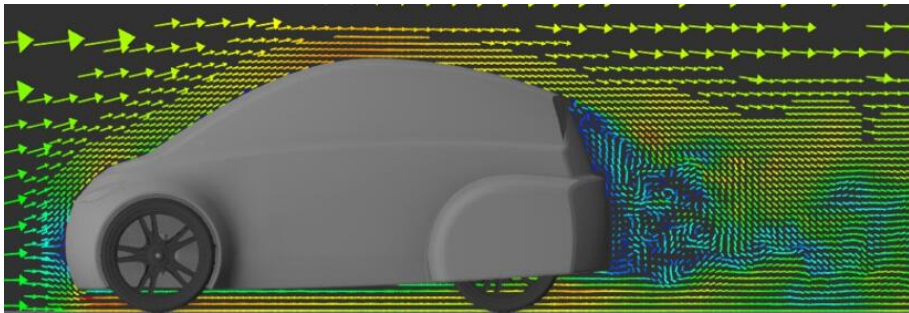


Figure 6.16: Spoiler 1 - centre cut velocity vectors

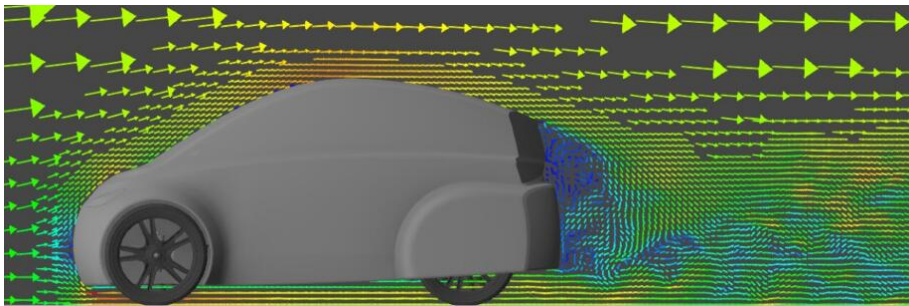


Figure 6.17: Spoiler 2 - centre cut velocity vectors

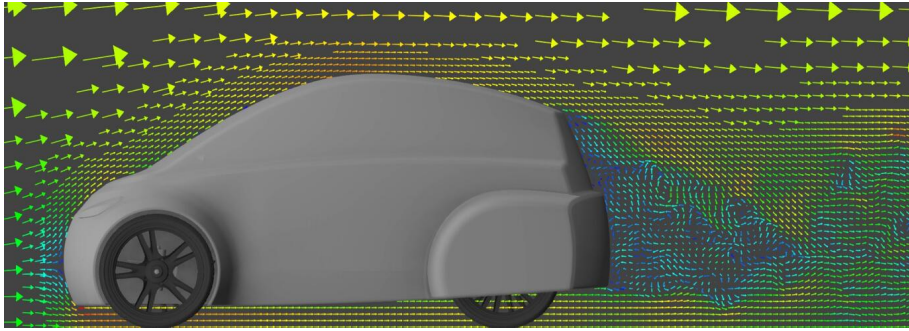


Figure 6.18: Final model - centre cut velocity vectors

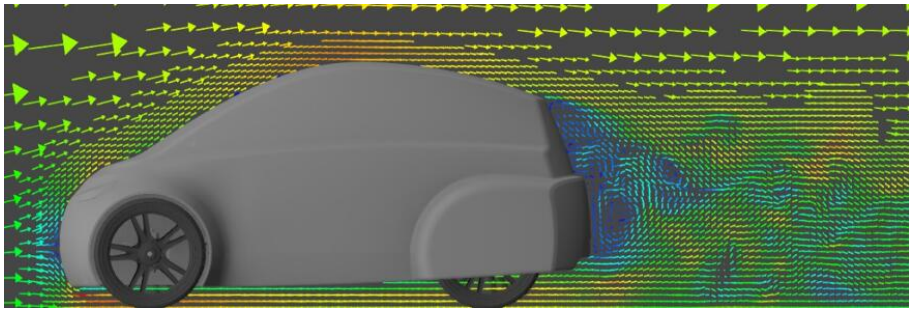


Figure 6.19: Diffuser 1 - centre cut velocity vectors

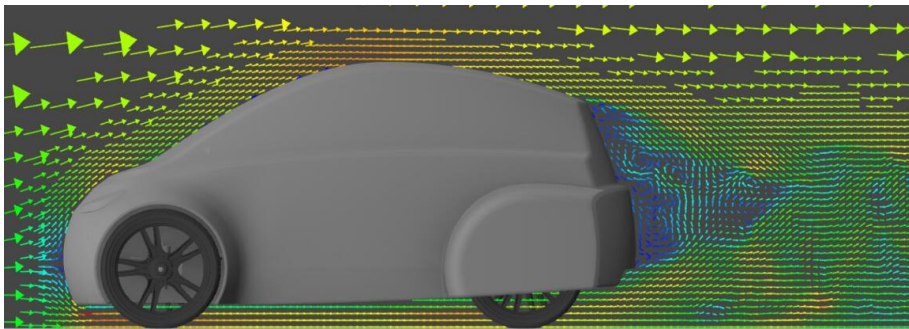


Figure 6.20: Diffuser 2 - centre cut velocity vectors

6.3.5 Modification combination development

None of the modifications presented provided a large downforce, the possible underestimation of lift as seen in the CFD comparison results could have resulted in some simulations giving different results where the lift or downforce contributed greatly. The modifications which improved the required characteristics were chosen to be implemented in the final design in combination. Combining different modifications can result in enhancing or reducing the effectiveness of a certain mod, which may have a change of improving overall efficiency. Combinations could negate the negative effects of specific modifications with the positive effect of others. The most positively influential modifications from straightforward and yawed flow are listed below in Table 6.9 and Table 6.10 respectively. From this four vehicle models combining certain modifications are selected with results shown in Table 6.11.

Table 6.9: Positively affecting modifications - Normal flow

C_x	C_y
Rear spoiler 1	Rear spoiler 1
Rear spoiler 2	Rear diffuser 1
Wheel diffuser	Rear diffuser 2
Wheel cover	Side skirt
Wheel arch top vent	Wheel arch rear vent
Wheel arch slot	Front air guide 2
	Side mirrors
	Rear vein

Table 6.10: Positively affecting modifications - yawed flow

C_x	C_y	C_z
Rear spoiler 1	Rear spoiler 2	Rear spoiler 1
Rear spoiler 2	Rear diffuser 1	Rear spoiler 2
Rear diffuser 1	Rear diffuser 2	Rear diffuser 1
Rear diffuser 2	Side mirrors	Rear diffuser 2
		Wheel arch slot
		Side mirror
		Rear vein

Table 6.11: Positively affecting modifications - yawed flow

Combination 1	Combination 2	Combination 3	Combination 4
Rear spoiler 1 Rear diffuser 1 Side skirt	Rear spoiler 1 Rear diffuser 1 Wheel diffuser Wheel covers Wheel arch vent rear Wheel arch slot	Rear spoiler 2 Rear diffuser 2 Wheel diffuser Wheel covers Wheel arch vent rear Wheel arch slot Front air guide 2	Rear spoiler 2 Rear diffuser 2 Wheel diffuser Wheel covers Wheel arch vent rear Wheel arch slot Front air guide 2 Rear Vein

6.3.6 Modification combination results and discussion

Table 6.12: Modification combination results

Case	Initial elements	Final elements	C_D	C_L	C_Z
Combination 1	942467	8757981	0.398	-0.099	-
Combination 1 with yaw	942109	11117526	0.437	0.155	-0.428
Combination 2	9474941	8137373	0.369	0.023	-
Combination 2 with yaw	947126	11394507	0.423	0.381	-0.423
Combination 3	947245	7970835	0.361	0.027	-
Combination 3 with yaw	946880	10987554	0.426	0.418	-0.426
Combination 4	946253	7983010	0.371	-0.023	-
Combination 4 with yaw	945818	11147695	0.439	0.304	-0.395

From the results seen in Table 6.12 it can be said that combination 3 performed the best in terms of having the lowest drag (C_x), however it did not have an adequate lift value. The most promising overall combinations were 1 and 4, combination 1 had a larger downforce and has the lowest downforce during yawed flow. Combination 4 had a decent drag coefficient, light downforce as well as having the least side wind sensitivity. The implementation of these modifications in combination proved to reduce drag and lift in straightforward flow, and reduce sidewind sensitivity in yawed flow. From this it can be seen that more combinations and alteration of modifications is required to optimise for all characteristics.

6.3.7 Final result and discussion

From comparing the results of the final simulation to the results from the low-drag concept, the chosen preliminary design and the final unmodified vehicle (Table 6.13), the following can be said; although aesthetic design had some apparent negative effect on aerodynamics, the use of many different simulations along the design evolution and the use of modifications allowed the control and improvement on overall aerodynamic characteristics of the vehicle.

Table 6.13: Final results

Case	Initial elements	Final elements	C_D	C_L	C_Z
Chosen combination	946253	7983010	0.371	-0.023	–
Chosen combination with yaw	945818	11147695	0.439	0.304	-0.395
Final design	941464	9233405	0.399	-0.006	–
Final design with yaw	941106	11097679	0.463	0.279	-0.443
Preliminary concept	503874	7836108	0.324	0.399	–
Preliminary concept with yaw	503740	9214638	0.410	0.437	-0.278
Initial concept	522171	7372749	0.424	0.033	–
Initial concept with yaw	523534	8694774	0.443	0.194	0.-468

Chapter 7

Conclusion and recommendations

Conclusion

This work presents the computational fluid dynamics analysis of a light road vehicle. Using the presented method, it was found that the optimisation of vehicle aerodynamics can easily be done alongside the design evolution from initial low-drag shapes to the final detail design, ensuring aerodynamic characteristics are controlled with aesthetic change. This paper implements meshless CFD analysis with dynamic refinement, the use of a rolling road, rotating detail geometry wheels, yawed flow as well as the use of 3D scanning which allowed the exact replication of wheel geometries for the purpose of detail simulation. The methods used in geometry development and CFD simulations setup allowed for easy integration between the software and ensured uniform simulations.

From the low-drag concept to the final design, all aerodynamic coefficients were able to be improved upon whilst the model became more complex. The use of multiple modifications increased effectiveness and was able to further improve aerodynamic characteristics and efficiency.

Mesh based CFD software such as FLUENT requires the user to edit the CAD geometry and simplify the model in order to perform a boolean with the wind tunnel domain, this allows the mesh to be generated in a single fluid region. The user must then define the fluid surface interaction properties for each simulation, this results in a tedious, time-consuming task when many simulations are required. XFLOW gives a much simpler and more efficient platform in which to achieve CFD analysis. The way in which the lattice Boltzmann method is solved allows the software to quickly generate the domain and fluid surface interaction properties. This method works very well in an industry which requires many designs to be analysed over a design criteria. XFLOW makes it able to easily set the refinement and simulation parameters such as wake refinement, moving objects as well as allowing complex models that do not require simplification.

The main differences between the CFD software comparison results was seen for the lift coefficient far more than that of the drag. The rolling road influence had around a

10% reduction in drag and as much as 50% change in lift for specific refinement levels. The change due to rolling road results from FLUENT using the Spalart-Allmaras turbulence model showed better comparability to the theory. Refinement had negligible effect on the drag in FLUENT while having a change in lift for the WALE model of around 50%. The increased refinement had an average of around 12% reduction in drag for all XFLOW simulations and an increase in lift by as much as 200%, with the effect of rolling road further increasing lift by 150%. The implementation of rotating wheels in XFLOW does show a drag loss as presumed from the theory, however, large differences in lift are seen between the refinement levels as well as the turbulence models. Lift was increased by 175% when comparing the difference between the lower and higher resolution schemes for rolling road in XFLOW for both turbulence models. The lattice Boltzmann method simulations show similar drag and lift changes between the WALE and SA turbulence models, refinement levels and stationary/rolling road configurations; however, Reynolds averaged Navier-Stokes simulations showed that the refinement levels used had a greater effect on aerodynamic characteristics for the WALE turbulence model compared to the SA. Differences of 50% were seen for the lift coefficient in FLUENT between turbulence models for the initial refinement, and as much as 100% difference for the higher refinement level.

For the specified refinement levels, consistency cannot be achieved between the CFD and turbulence models used. Using multiple CFD and turbulence models at low refinement levels could assist in allowing the designer to predict the aerodynamic performance, however, based on the solvers and turbulence models, the refinement used in this study showed varying effects on the change in drag and lift for rolling and stationary road simulations. The lift coefficient of the vehicle for the most part was seen to show a much greater change when compared to drag from the comparisons of solvers, turbulence models, refinement and the effect of rolling road. Determining the drag of a light vehicle can be easily achieved and verified using multiple solvers and methods, however, the lift coefficient and its validation require a greater understanding of the vehicle flow field as well as the solvers, turbulence models and refinement levels capable of correctly simulating the turbulent regions around a vehicle. It is possible the eddies formed around certain features could not be represented using a moderate refinement. A higher resolution showed better comparability; however, the time in which it takes to simulate at the higher resolution compromises the effectiveness of the lattice Boltzmann method solution, especially when wake refinement is a key aspect as it drastically increased the number of elements. Simulations involving the higher refinement criteria took as much as three times longer than a simulations with the same model at lower resolution with wake refinement and two times longer than a detailed simulation with wake refinement. XFLOW was found to take more than twice as long than a similar setup FLUENT simulation, this could however be due to the different method of discretisation between XFLOW and FLUENT as refining did not result in a uniform change of results between the software.

The work presented in this thesis will hope to aid the aerodynamic development of road vehicles along their design progression and enable designers and engineers to evaluate aerodynamic characteristics of many vehicle designs in order to achieve an aerodynamic and aesthetically pleasing vehicle.

Recommendations

The level of discretisation required for CFD simulations of this type is greatly governed by processing power, to properly conduct future simulations the refinement will have to be optimised for the available computing power with region-wise refinement in order to correctly and efficiently simulate flow characteristics around a road vehicle.

The ability to average data was limited due to large amount of hard disk space required and was not used in all simulations due to the number of simulations and space constraints. This feature allows the observation of the steady state which gives an averaged look at the airflow characteristics around the vehicle. Using this feature more often in future simulations will allow for greater overall understanding of the flow physics.

XFLOW also allows for dynamic body simulations which allows for dynamic suspension, allowing the vehicle body to move due to wind forces. With the unknown parameters of vehicle weight, centre of gravity and suspension characteristics it was difficult to reproduce an accurate simulation. Using this feature would be a key aspect in understanding the flow field around the dynamic vehicle for further aerodynamic optimisation.

Specific studies can be approached for all aspects of the vehicle's aerodynamic design, such as; the development of a highly adaptable vehicle geometry with modification optimisation and implementation of new aerodynamic appendages, a specific wheel arch study which relies heavily on rotating detailed wheels including a vehicle in cornering conditions and the development of a rolling road and rotating wheels system for a scale wind tunnel.

APPENDICES

Appendix A

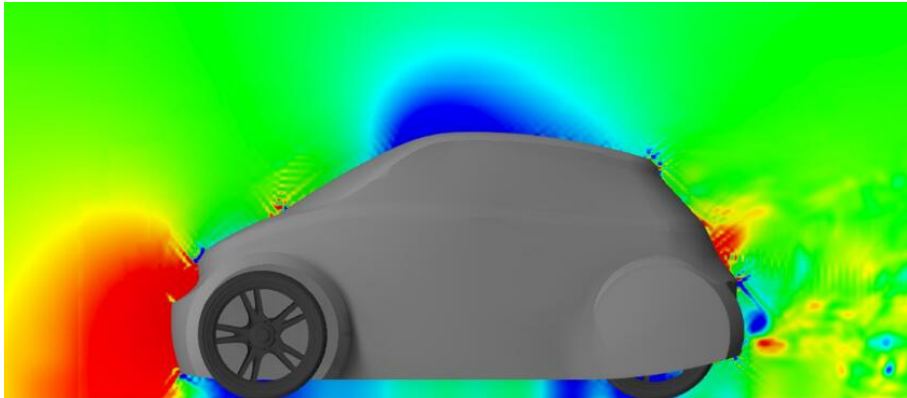


Figure A1: XY-plane pressure cut plot - concept 1

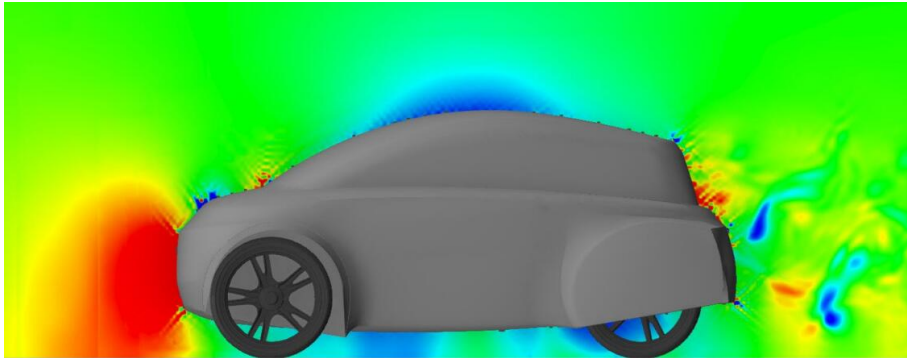


Figure A2: XY-plane pressure cut plot - concept 2

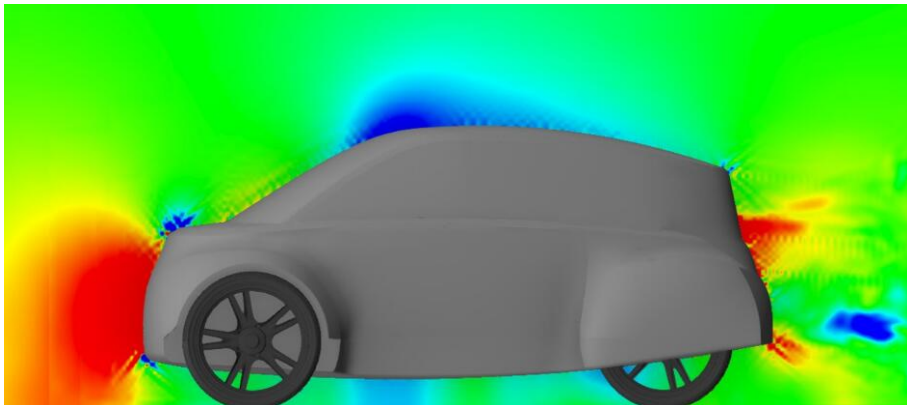


Figure A3: XY-plane pressure cut plot - concept 3

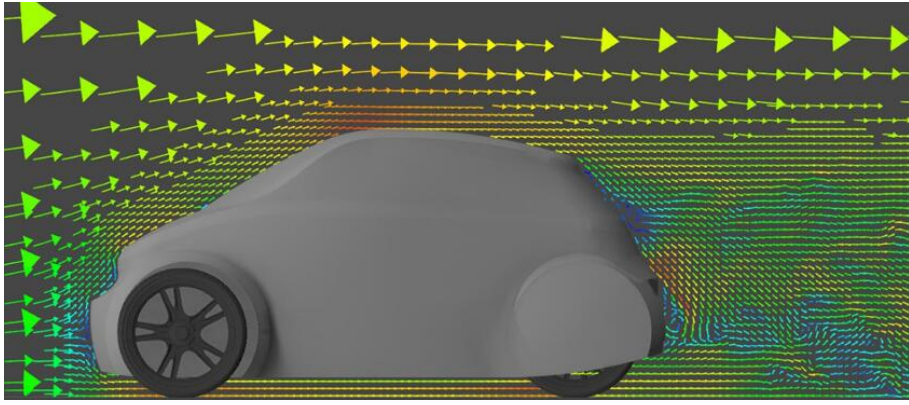


Figure A4: XY-plane velocity vectors cut plot - concept 1

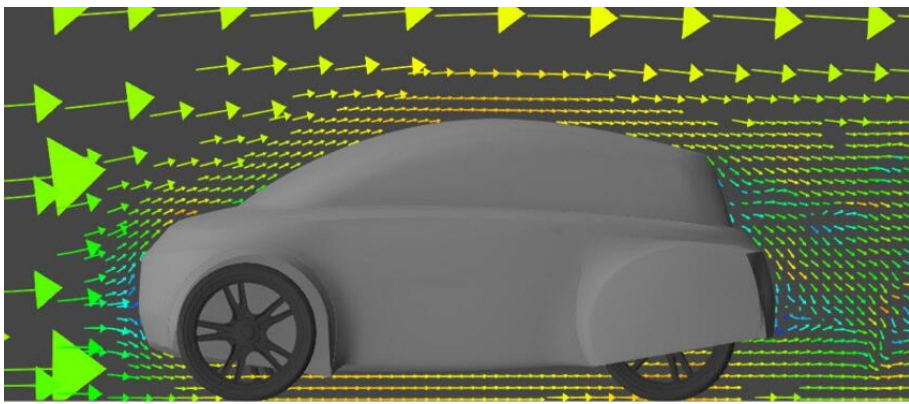


Figure A5: XY-plane velocity vectors cut plot - concept 2

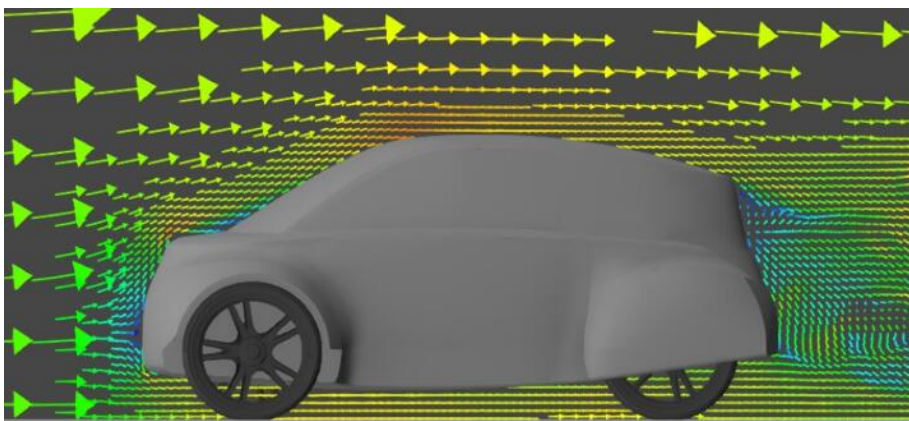


Figure A6: XY-plane velocity vectors cut plot - concept 3

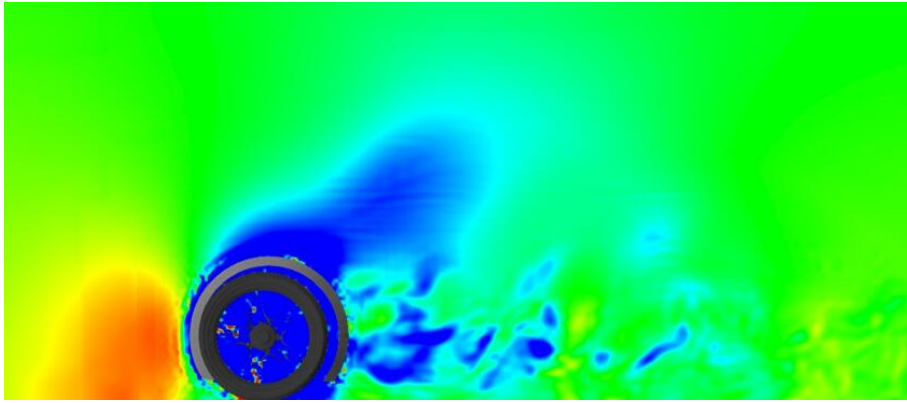


Figure A7: XY-plane pressure cut plot at wheels - concept 1

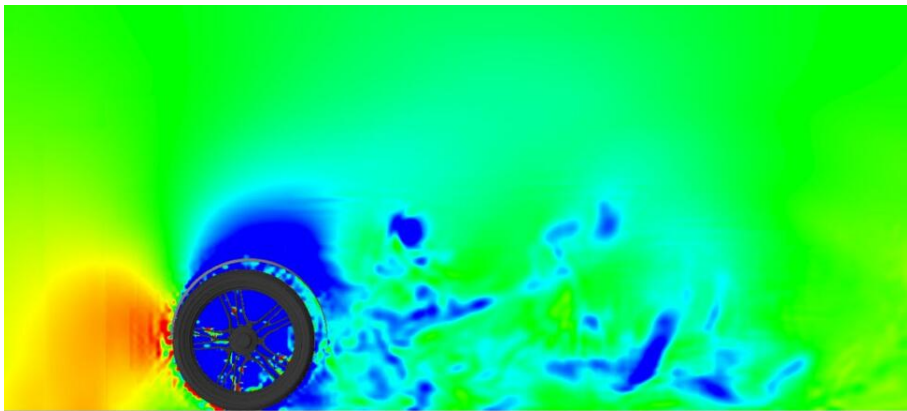


Figure A8: Centre cut XY-plane pressure cut plot at wheels - concept 2

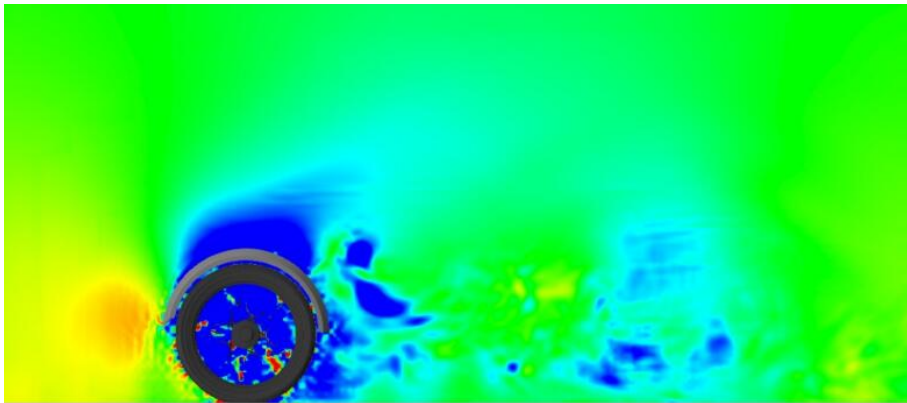


Figure A9: Centre cut XY-plane pressure cut plot at wheels - concept 3

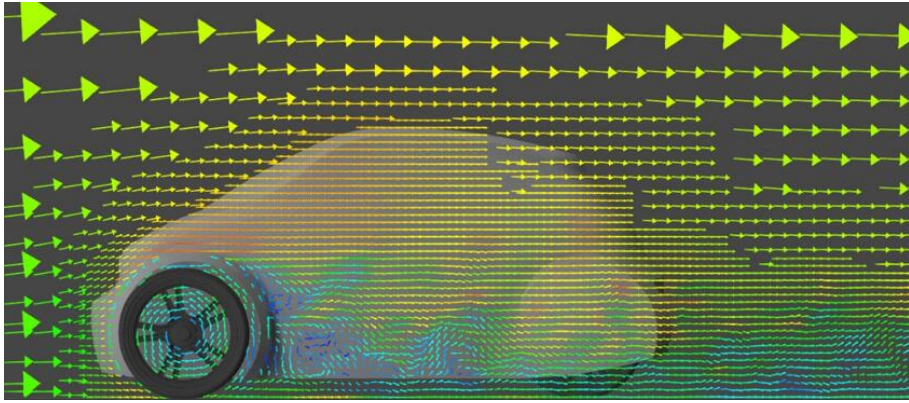


Figure A10: XY-plane velocity vectors cut plot at wheels - concept 1

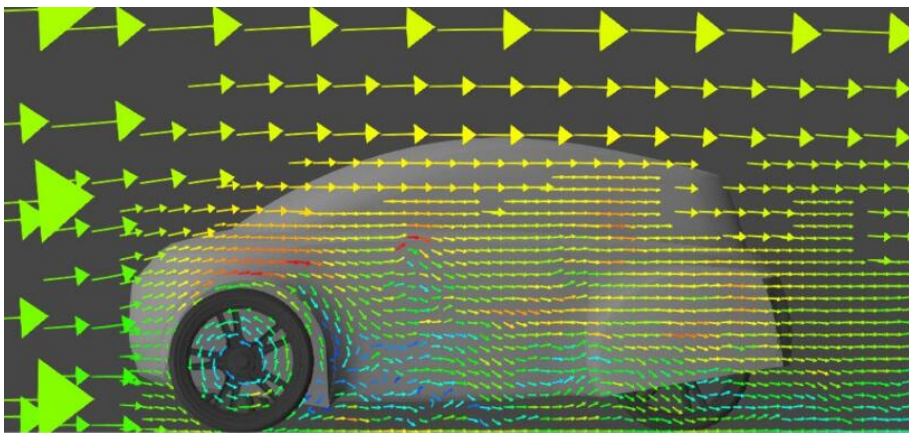


Figure A11: XY-plane velocity vectors cut plot at wheels - concept 2

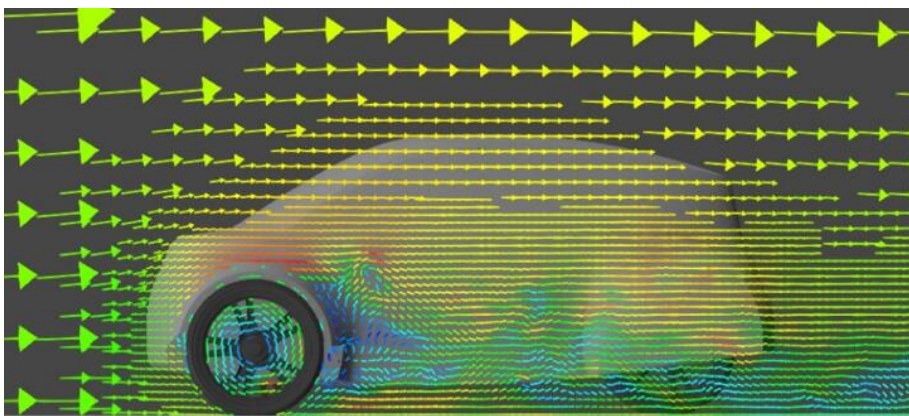


Figure A12: XY-plane velocity vectors cut plot at wheels - concept 3

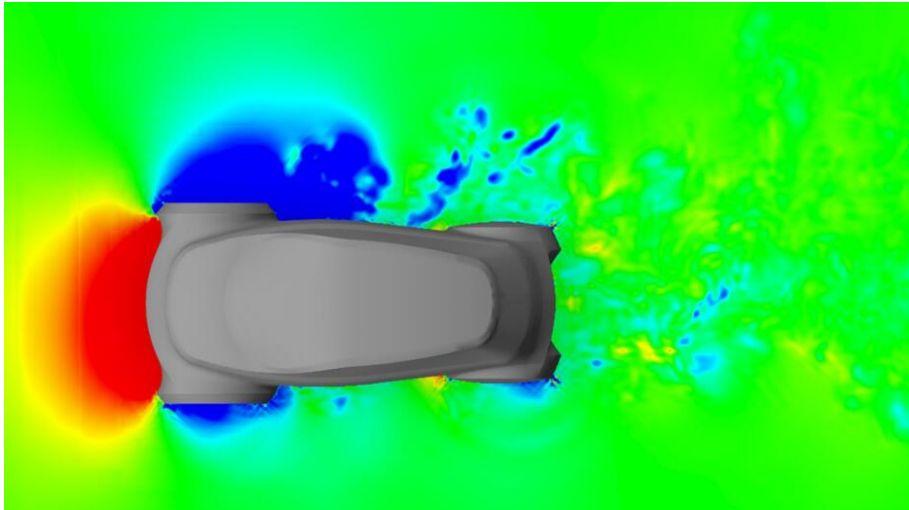


Figure A13: XZ-plane pressure cut plot - concept 1

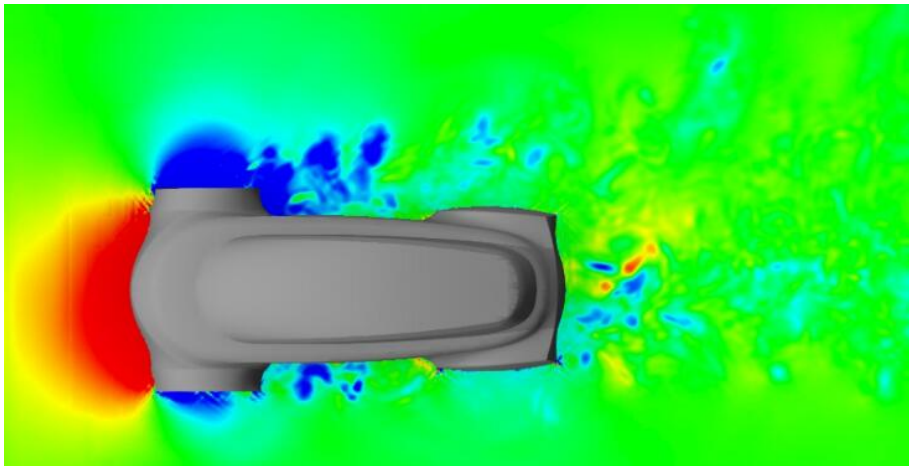


Figure A14: XZ-plane pressure cut plot - concept 2

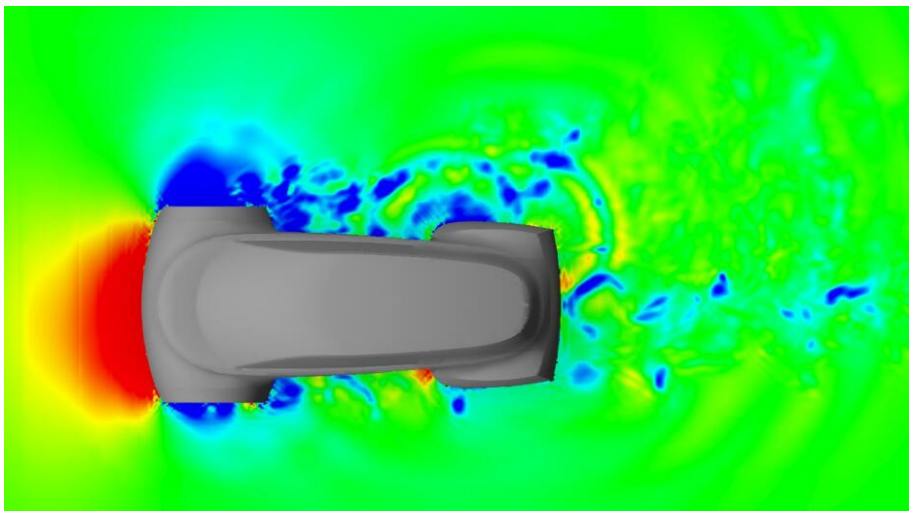


Figure A15: XZ-plane pressure cut plot - concept 3

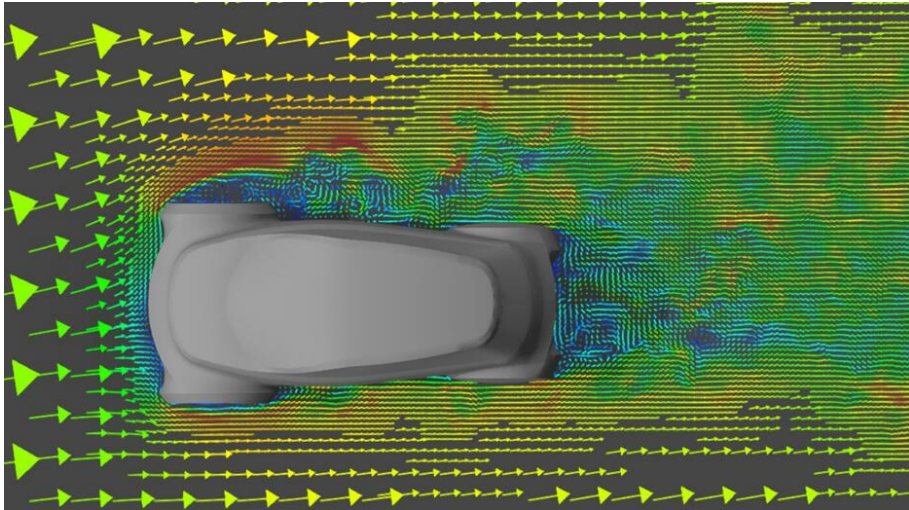


Figure A16: XZ-plane pressure cut plot - concept 1

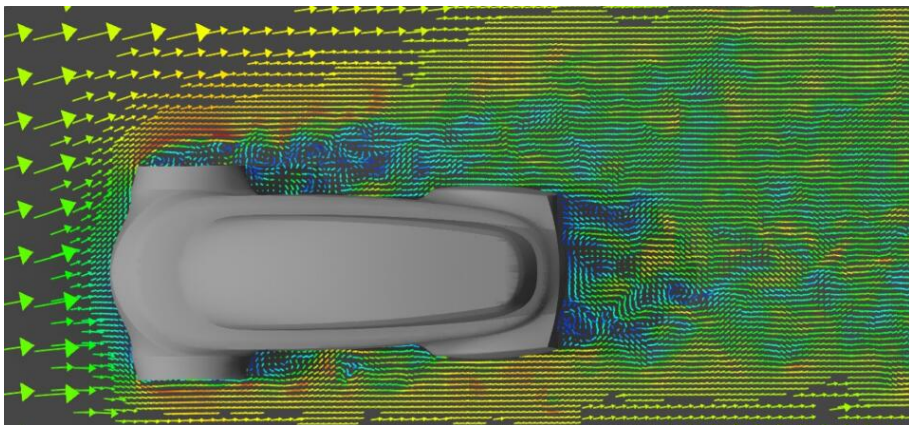


Figure A17: XZ-plane pressure cut plot - concept 2

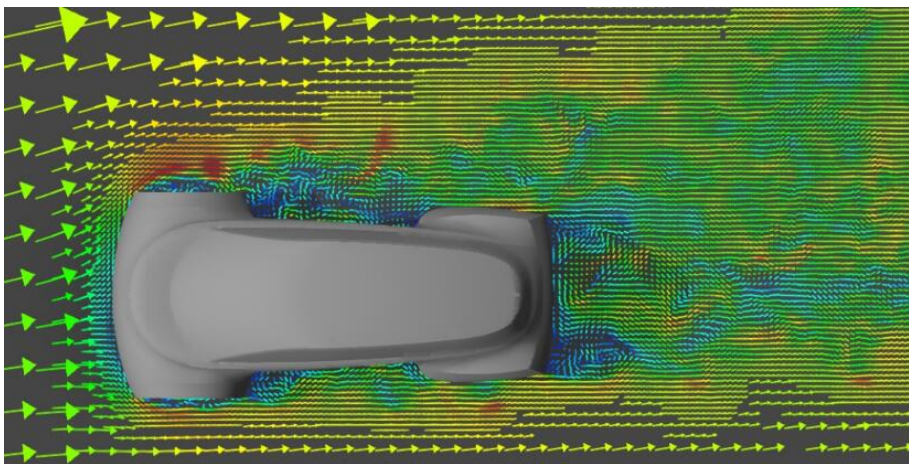


Figure A18: XZ-plane pressure cut plot - concept 3

Appendix B

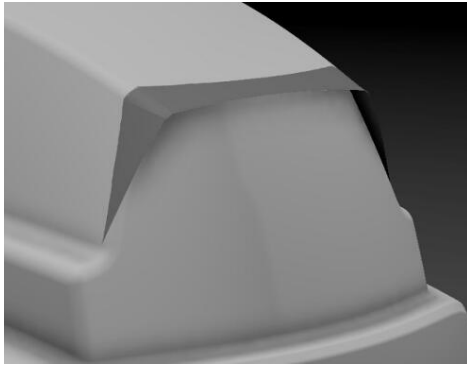


Figure B1: Spoiler 1

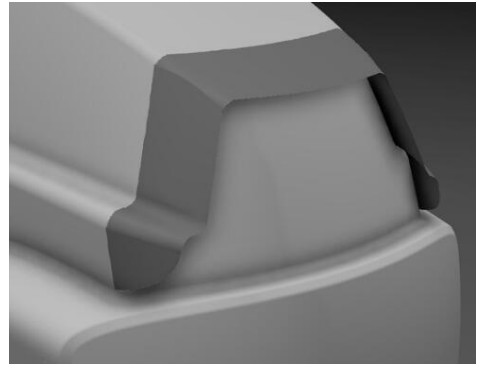


Figure B2: Spoiler 2

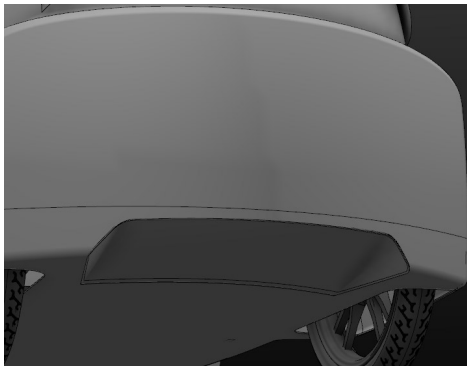


Figure B3: Diffuser 1

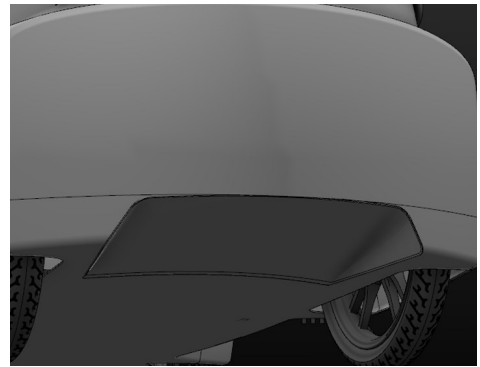


Figure B4: Diffuser 2



Figure B5: Front diffuser

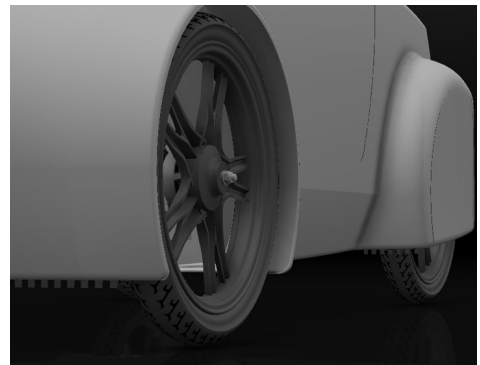


Figure B6: Wheel diffusers

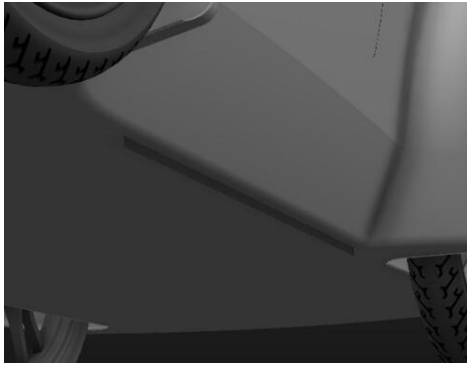


Figure B7: Side skirt

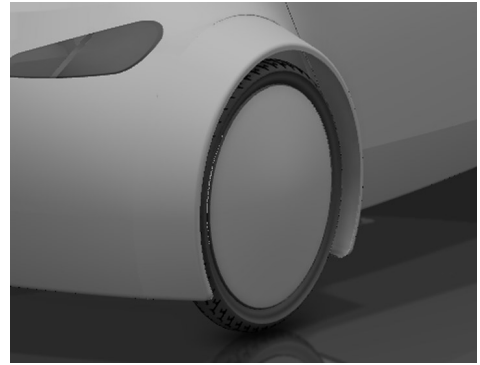


Figure B8: Wheel cover

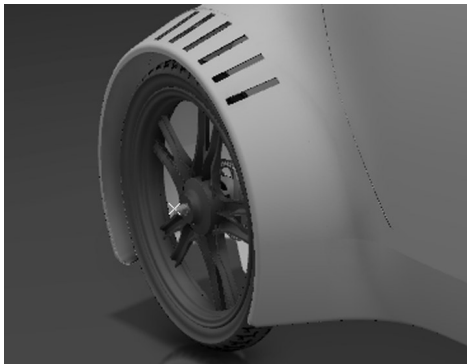


Figure B9: Wheel arch top vent

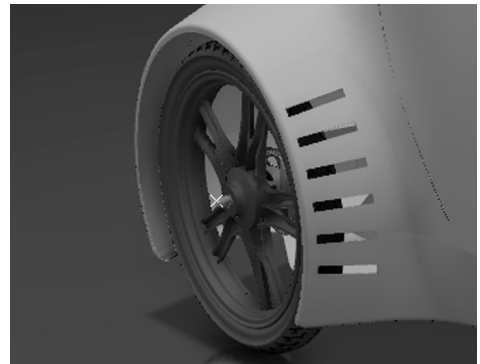


Figure B10: Wheel arch rear vent

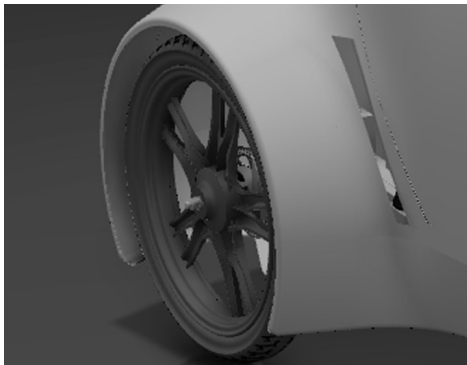


Figure B11: Wheel arch slot

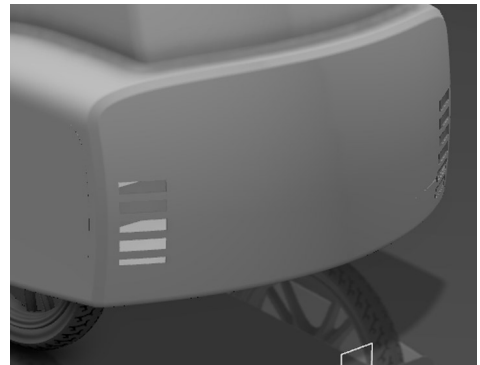


Figure B12: Rear vent

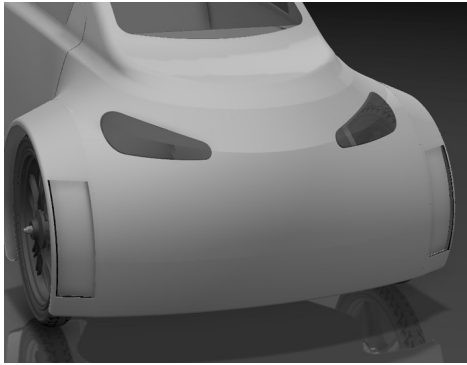


Figure B13: Front air guide 1

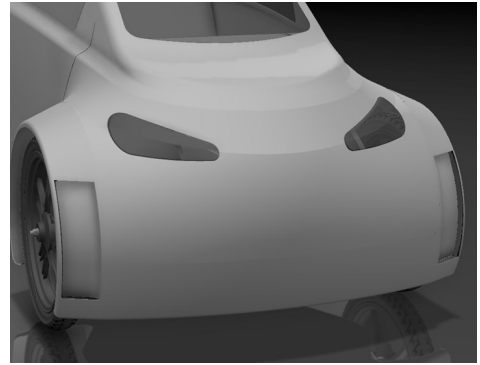


Figure B14: Front air guide 2

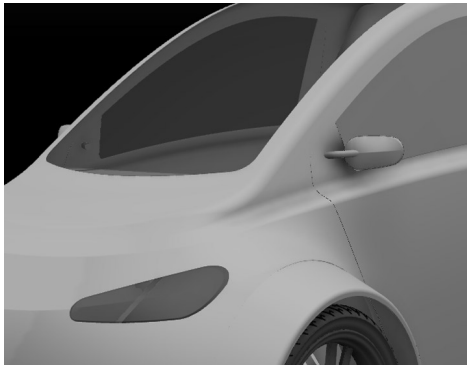


Figure B15: Side mirrors



Figure B16: Rear air guide

Bibliography

- SR Ahmed, G Ramm, and G Faltin. Some salient features of the time-averaged ground vehicle wake. Technical report, SAE Technical Paper, 1984.
- Steven R Allmaras and Forrester T Johnson. Modifications and clarifications for the implementation of the spalart-allmaras turbulence model. In *Seventh International Conference on Computational Fluid Dynamics (ICCFD7)*, pages 1–11, 2012.
- John David Anderson et al. *Computational fluid dynamics*, volume 206. Springer, 1995.
- Peter Aschwenden, Jürg Müller, Gian Claudio Travaglio, and Timo Schöning. The influence of motion aerodynamics on the simulation of vehicle dynamics. Technical report, SAE Technical Paper, 2008.
- Nasser Ashgriz and Javad Mostaghimi. An introduction to computational fluid dynamics. *Fluid flow handbook. McGraw-Hill Professional*, 2002.
- PW Bearman, D De Beer, E Hamidy, and JK Harvey. The effect of a moving floor on wind-tunnel simulation of road vehicles. Technical report, SAE Technical Paper, 1988.
- Yunus A Cengel and John M Cimbala. *Fluid Mechanics: Fundamentals and Applications 2nd Revised edition Edition*. McGraw-Hill Professional, 2009.
- Shiyi Chen and Gary D Doolen. Lattice boltzmann method for fluid flows. *Annual review of fluid mechanics*, 30(1):329–364, 1998.
- Antonello Cogotti. Ground effect simulation for full-scale cars in the pininfarina wind tunnel. Technical report, SAE Technical Paper, 1995.
- MN Dhaubhadel. Review: Cfd applications in the automotive industry. *Journal of fluids engineering*, 118(4):647–653, 1996.
- F. Ducros, F. Nicoud, and T. Poinsot. *Wall-Adapting Local Eddy-Viscosity models for simulations in complex geometries*. Avenue Gaspard Coriolis, 31057 Toulouse cedex, 1999.
- Bradley D Duncan, Satheesh Kandasamy, Khaled Sbeih, Todd H Lounsberry, and Mark E Gleason. Further cfd studies for detailed tires using aerodynamics simulation with rolling road conditions. Technical report, SAE Technical Paper, 2010.
- B Fago, H Lindner, and O Mahrenholtz. The effect of ground simulation on the flow around vehicles in wind tunnel testing. *Journal of Wind Engineering and Industrial Aerodynamics*, 38(1):47–57, 1991.
- Ehab Fares. Unsteady flow simulation of the ahmed reference body using a lattice boltzmann approach. *Computers & Fluids*, 35(8):940–950, 2006.
- Joel H Ferziger and Milovan Perić. *Computational methods for fluid dynamics*, volume 3. Springer Berlin, 2002.
- Ansys Fluent. 14.5, theory guide; ansys. *Inc., Canonsburg, PA*, 2012.

- Patrick Gilliéron and Francis Chometon. Modelling of stationary three-dimensional separated air flows around an ahmed reference model. In *ESAIM: Proceedings*, volume 7, pages 173–182. EDP Sciences, 1999.
- J Hardy, O De Pazzis, and Yves Pomeau. Molecular dynamics of a classical lattice gas: Transport properties and time correlation functions. *Physical review A*, 13(5):1949, 1976.
- Xiaoyi He and Li-Shi Luo. Lattice boltzmann model for the incompressible navier–stokes equation. *Journal of statistical Physics*, 88(3-4):927–944, 1997.
- Alexander Hennig, Nils Widdecke, Timo Kuthada, and Jochen Wiedemann. Numerical comparison of rolling road systems. Technical report, SAE Technical Paper, 2011.
- FJ Higuera and J Jimenez. Boltzmann approach to lattice gas simulations. *EPL (Europhysics Letters)*, 9(7):663, 1989.
- David M Holman, R Brionnaud, and Zaki Abiza. Solution to industry benchmark problems with the lattice-boltzmann code xflow. In *Proceeding in the European Congress on Computational Methods in Applied Sciences and Engineering (ECCOMAS)*, 2012a.
- David M Holman, Ruddy Brionnaud, Francisco Martinez, and Monica Mier-Torrecilla. Advanced aerodynamic analysis of the nasa high-lift trap wing with a moving flap configuration. In *2nd AIAA High Lift Prediction Workshop*, 2012b.
- RJA Howard and M Pourquie. Large eddy simulation of an ahmed reference model. *Journal of Turbulence*, 3(5), 2002.
- W Ho Hucho, LJ Janssen, and HJ Emmelmann. The optimization of body details-a method for reducing the areodynamic drag of road vehicles. Technical report, SAE Technical Paper, 1976.
- Wolf-Heinrich Hucho. *Aerodynamics of road vehicles*. Butterworth Publishers, Stoneham, MA, 1987.
- Angel Humnic and Anghel Chiru. On cfd investigations of vehicle aerodynamics with rotating wheels’ simulation. Technical report, SAE Technical Paper, 2006.
- Seung-On Kang, Sang-Ook Jun, Hoon-Il Park, Yo-Cheon Ku, Jung-Do Kee, Dong-Hee Hong, Kyu-Hong Kim, and Dong-Ho Lee. Influence of rotating wheel and moving ground condition to aerodynamic performance of 3-dimensional automobile configuration. *Transactions of the Korean Society of Automotive Engineers*, 18(5):100–107, 2010.
- Sinisa Krajnovic and Lars Davidson. Development of large-eddy simulation for vehicle aerodynamics. In *ASME 2002 International Mechanical Engineering Congress and Exposition*, pages 165–172. American Society of Mechanical Engineers, 2002.
- Siniša Krajnović and Lars Davidson. Influence of floor motions in wind tunnels on the aerodynamics of road vehicles. *Journal of wind engineering and industrial aerodynamics*, 93(9):677–696, 2005.
- Christoffer Landström, Lennart Löfdahl, and Tim Walker. Detailed flow studies in close proximity of rotating wheels on a passenger car. Technical report, SAE Technical Paper, 2009.
- Christoffer Landström, Tim Walker, and Lennart Löfdahl. Effects of ground simulation on the aerodynamic coefficients of a production car in yaw conditions. Technical report, SAE Technical Paper, 2010.
- Christoffer Landström, Tim Walker, Lasse Christoffersen, and Lennart Löfdahl. Influences of different front and rear wheel designs on aerodynamic drag of a sedan type passenger car. Technical report, SAE Technical Paper, 2011.
- Andrew A Lawson, Robert G Dominy, David B Sims-Williams, and Paul Mears. A comparison between on-road and wind tunnel surface pressure measurements on a mid-sized hatchback. Technical report, SAE Technical Paper, 2007.

- H Lienhart, C Stoots, and S Becker. Flow and turbulence structures in the wake of a simplified car model (ahmed modell). In *New Results in Numerical and Experimental Fluid Mechanics III*, pages 323–330. Springer, 2002.
- Todd H Lounsberry, Mark E Gleason, Satheesh Kandasamy, Khaled Sbeih, Richa Mann, and Bradley D Duncan. The effects of detailed tire geometry on automobile aerodynamics-a cfd correlation study in static conditions. Technical report, SAE Technical Paper, 2009.
- Jochen Mayer, Michael Schrefl, and Rainer Demuth. On various aspects of the unsteady aerodynamic effects on cars under crosswind conditions. Technical report, SAE Technical Paper, 2007.
- Wolfgang Mayer and Jochen Wiedemann. The influence of rotating wheels on total road load. Technical report, SAE Technical Paper, 2007.
- Guy R McNamara and Gianluigi Zanetti. Use of the boltzmann equation to simulate lattice-gas automata. *Physical Review Letters*, 61(20):2332, 1988.
- E. Olsen, E. Olson, and G. Jahansson. *Vehicle aerodynamics - force and moment measurements on scaled car models using stationary and moving-belt ground planes*. Academic OneFile, 2014.
- YH Qian, Dominique d’Humières, and Pierre Lallemand. Lattice bgk models for navier-stokes equation. *EPL (Europhysics Letters)*, 17(6):479, 1992.
- David Schroeck, Werner Krantz, Nils Widdecke, and Jochen Wiedemann. Unsteady aerodynamic properties of a vehicle model and their effect on driver and vehicle under side wind conditions. Technical report, SAE Technical Paper, 2011.
- Simone Sebben. Numerical flow simulations of a detailed car underbody. Technical report, SAE Technical Paper, 2001.
- Tsan-Hsing Shih, Louis A Povinelli, Nan-Suey Liu, Mark G Potapczuk, and JL Lumley. A generalized wall function. *National Aeronautics and Space Administration, Glenn Research Center*, 1999.
- Adrian F Skea, Peter Ronald Bullen, and Jun Qiao. Cfd simulations and experimental measurements of the flow over a rotating wheel in a wheel arch. Technical report, SAE Technical Paper, 2000.
- J Slater. Uncertainty and error in cfd applications. *NPARC Alliance CFD Verification and Validation Web Site*, 2008.
- RK Strachan, K Knowles, and NJ Lawson. The vortex structure behind an ahmed reference model in the presence of a moving ground plane. *Experiments in fluids*, 42(5):659–669, 2007.
- Sauro Succi. *The Lattice Boltzmann Equation*. Oxford university press, Oxford, 2001.
- M Takagi. Application of computers to automobile aerodynamics. *Journal of Wind Engineering and Industrial Aerodynamics*, 33(1):419–428, 1990.
- Alexander Wäschle. The influence of rotating wheels on vehicle aerodynamics-numerical and experimental investigations. Technical report, SAE Technical Paper, 2007.
- Jochen Wiedemann. The influence of ground simulation and wheel rotation on aerodynamic drag optimization-potential for reducing fuel consumption. Technical report, SAE Technical Paper, 1996.